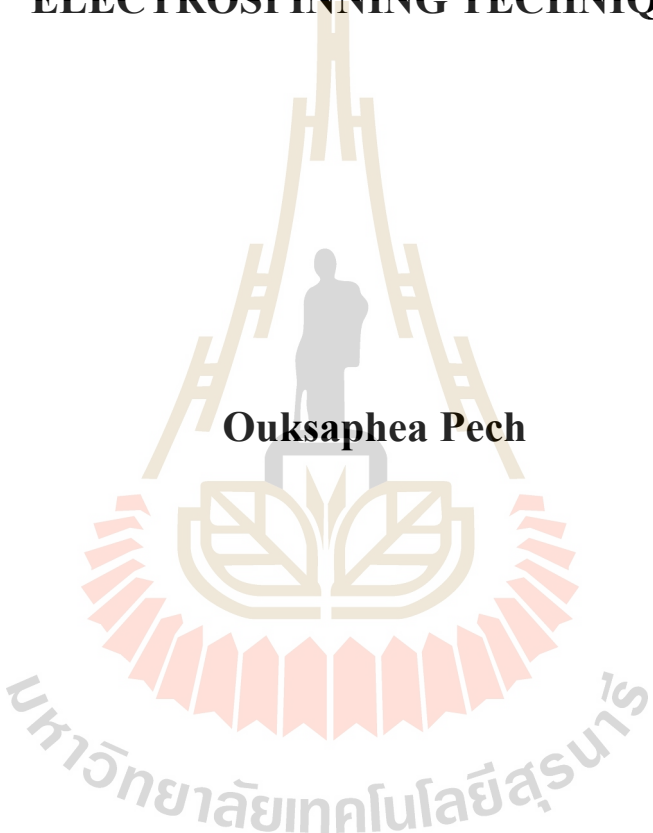


**PREPARATION, STRUCTURE, AND
ELECTROCHEMICAL PROPERTIES OF CARBON
NANOFIBERS FABRICATED BY CORE-SHELL
ELECTROSPINNING TECHNIQUE**

Ouksaphea Pech



**A Thesis Submitted in Partial Fulfillment of the Requirements for the
Degree of Doctor of Philosophy in Physics
Suranaree University of Technology
Academic Year 2018**

การเตรียม โครงสร้างและสมบัติทางไฟฟ้าเคมีของเส้นใยนาโนคาร์บอน
เตรียมด้วยเทคนิคอิเล็กโทรสปินนิงแบบแกนใน-เปลือกนอก



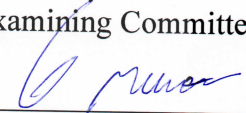
นายอุสเฟีย บ้าง

วิทยานิพนธ์นี้เป็นส่วนหนึ่งของการศึกษาตามหลักสูตรปริญญาวิทยาศาสตรดุษฎีบัณฑิต
สาขาวิชาฟิสิกส์
มหาวิทยาลัยเทคโนโลยีสุรนารี
ปีการศึกษา 2561

**PREPARATION, STRUCTURE, AND ELECTROCHEMICAL
PROPERTIES OF CARBON NANOFIBERS FABRICATED BY
CORE-SHELL ELECTROSPINNING TECHNIQUE**

Suranaree University of Technology has approved this thesis submitted in partial fulfillment of the requirements for the Degree of Doctor of Philosophy.

Thesis Examining Committee



(Asst. Prof. Dr. Worawat Meevasana)

Chairperson



(Prof. Dr. Santi Maensiri)

Member (Thesis Advisor)



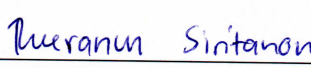
(Asst. Prof. Dr. Nonglak Meethong)

Member



(Assoc. Prof. Dr. Prayoon Songsiriritthigul)

Member



(Asst. Prof. Dr. Theeranun Siritanon)

Member



(Prof. Dr. Santi Maensiri)

Vice Rector for Academic Affairs
and Internationalization



(Asst. Prof. Dr. Worawat Meevasana)

Dean of Institute of Science

อุสเพีย บัจ : การเตรียม โครงสร้างและสมบัติทางไฟฟ้าเคมีของเส้นใยนาโนคาร์บอน
เตรียมด้วยเทคนิคอิเล็กโตรสปินนิงแบบแกนใน-เปลือกนอก (PREPARATION,
STRUCTURE, AND ELECTROCHEMICAL PROPERTIES OF CARBON
NANOFIBERS FABRICATED BY CORE-SHELL ELECTROSPINNING
TECHNIQUE) อาจารย์ที่ปรึกษา : ศาสตราจารย์ ดร.สันติ แม้นศิริ, 283 หน้า.

เส้นใยนาโนฐานคาร์บอน/แกนใน-เปลือกนอก/อิเล็กโตรสปินนิง/สมบัติทางไฟฟ้าเคมี/เส้นใยนาโน
คาร์บอนที่เชื่อมต่อกันต่าง ๆ/แมงกานีสออกไซด์/ตัวเก็บประจุไฟฟ้ายิ่งยวด

งานนี้ได้รายงานการเตรียมเส้นใยนาโนคาร์บอนต่าง ๆ เส้นใยนาโนคาร์บอนที่เชื่อมต่อกัน
ต่าง ๆ และเส้นใยนาโนคอมโพสิตคาร์บอนแมงกานีสออกไซด์ต่าง ๆ ซึ่งถูกประดิษฐ์ด้วยเทคนิค
อิเล็กโตรสปินนิงแบบเดิมและแบบแกนใน-เปลือกนอกตามลำดับด้วยการใช้ทั้งความร้อนและการ
กระตุ้นด้วยคาร์บอนไดออกไซด์ การเผาและกระบวนการกระตุ้นต่าง ๆ ของทุกตัวอย่างถูกทำที่
อุณหภูมิ 900 องศาเซลเซียสในก๊าซอาร์กอนและคาร์บอนไดออกไซด์ตามลำดับ สำหรับ IC-CNF
สัดส่วนโดยน้ำหนักของ PVP-PAN ถูกใช้เป็น PVP-PAN: 3-7 2-8 และ 1-9 ซึ่งถูกใช้เป็นสารละลาย
ตั้งต้นต่าง ๆ ของอิเล็กโตรสปินนิงพอลิเมอร์ผสมแบบหัวฉีดเดี่ยว นอกจากนี้ อิเล็กโตรสปินนิง
หัวฉีดแบบแกนใน-เปลือกนอกยังถูกใช้ในงานนี้ด้วย สำหรับเส้นใยแบบแกนใน-เปลือกนอกของ
เส้นใยนาโนแบบแกนใน-เปลือกนอกของคาร์บอนแมงกานีสออกไซด์คอมโพสิตต่าง ๆ สารละลาย
ของ PAN คือ สารละลายที่เป็นแกนใน ขณะที่ PAN ถูกผสมกับออกไซด์ของโลหะคือสารละลายที่
เป็นเปลือกนอก ด้วยการปรับเปลี่ยนสารละลายที่เป็นเปลือกนอกต่าง ๆ เราสามารถเตรียมได้
ตัวอย่างสามตัวอย่างที่แตกต่างกับไปตามสัดส่วนโดยน้ำหนักของแกนใน-เปลือกนอกเช่น 10-8 10-
9 และ 10-10 ในการวิเคราะห์ลักษณะต่าง ๆ ของวัสดุ กล้องจุลทรรศน์อิเล็กตรอนแบบส่องกราด
ชนิดฟิวอิมิชชัน (FE-SEM) ได้แสดงให้เห็นถึงลักษณะการเชื่อมต่อกันของเส้นใยกับเส้นใย อนุภาค
นาโนของแมงกานีสออกไซด์และลักษณะต่าง ๆ ของเส้นใย ลักษณะวิทยาของการเชื่อมต่อกัน
ของเส้นใยกับเส้นใยถูกพบในเส้นใยนาโนคาร์บอนแบบแกนใน-เปลือกนอกของ PVP-PAN/PAN-
PVP เท่านั้น ขณะที่ในการผสม PVP-PAN ไม่มี นอกจากนี้ ผลต่าง ๆ จาก FE-SEM นี้ ได้แสดงให้เห็น
ให้เห็นเส้นผ่านศูนย์กลางและขนาดอนุภาคต่าง ๆ ซึ่งถูกสอดคล้องกับพื้นที่จำเพาะจากเทคนิค การดูด
ซับ/คายก๊าซไนโตรเจน เส้นผ่านศูนย์กลางที่ใหญ่ที่สุดนี้ถูกพบใน CNF การผสมกันของ PVP และ
PAN ด้วยเทคนิคพอลิเมอร์ผสมหรืออิเล็กโตรสปินนิงแบบแกนใน-เปลือกนอกสามารถลดขนาดเส้น
ผ่านศูนย์กลางของเส้นใย โครงสร้างต่าง ๆ ของเส้นใยแบบแกนใน-เปลือกนอกของคาร์บอน

แมงกานีสออกไซด์คอมโพสิตได้แสดงให้เห็นในภาพตัดขวางของเส้นใยต่าง ๆ ซึ่งได้แสดงอนุภาคซึ่งอยู่ด้านนอกบนเส้นใยนาโนคาร์บอนต่าง ๆ differential scanning calorimetry (DSC) และ thermogravimetric analysis (TGA) ได้แสดงสมบัติต่าง ๆ เกี่ยวกับความร้อนของทุกตัวอย่าง เทคนิควิเคราะห์การเลี้ยวเบนของรังสีเอ็กซ์ (XRD) ได้แสดงคาร์บอนอสัณฐานเฟส โครงสร้างแกรไฟต์ และแมงกานีสออกไซด์ ขณะที่การวิเคราะห์รามานได้แสดงคุณภาพของคาร์บอนในตัวอย่างต่าง ๆ ประสิทธิภาพทางด้านไฟฟ้าเคมีถูกวัดในสารละลายโดยระบบสามขั้วในสารละลายโพแทสเซียมไฮดรอกไซด์ 6 โมลาร์ C/MnO_x ได้แสดงค่าการเก็บประจุจำเพาะที่มากที่สุดเท่ากับ 213.7 ฟารัดต่อกรัมที่ความหนาแน่นกระแส 0.5 แอมแปร์ต่อกรัม ด้วยความหนาแน่นพลังงาน 30 มิลลิวัตต์ชั่วโมงต่อกรัมที่ความหนาแน่นกำลัง 249 มิลลิวัตต์ต่อกรัม และมีความเสถียร 97 เปอร์เซ็นต์ หลังจาก 1000 รอบ จากผลต่าง ๆ ที่ขมวดเชื่อมโยงเหล่านี้จะเกิดจากผลร่วมกันของพฤติกรรมต่าง ๆ ของ EDLCs และซูโดคาปาซิทีฟของ CNF และ MnO_x เนื่องจากมีค่าความต้านทานในการถ่ายเทประจุที่ต่ำและมีพื้นที่ผิวที่สูง



สาขาวิชาฟิสิกส์
ปีการศึกษา 2561

ลายมือชื่อนักศึกษา Ouksaphea Pech
ลายมือชื่ออาจารย์ที่ปรึกษา Ob

OUKSAPHEA PECH : PREPARATION, STRUCTURE, AND
ELECTROCHEMICAL PROPERTIES OF CARBON NANOFIBERS
FABRICATED BY CORE-SHELL ELECTROSPINNING TECHNIQUE.
THESIS ADVISOR : PROF. SANTI MAENSIRI, D.Phil. 283 PP.

CARBON-BASED NANOFIBERS/CORE-SHELL
ELECTROSPINNING/ELECTROCHEMICAL PROPERTY/INTERCONNECTED
CARBON NANOFIBERS/MANGANESE OXIDE/SUPERCAPACITOR

This work reported the preparation of carbon nanofibers (CNFs), interconnected carbon nanofibers (ICNFs), and carbon-manganese oxide composite nanofibers (C/MnO_x) fabricated by a conventional and a core-shell electrospinning technique, respectively, with the combination of heat treatment and CO₂-activation process. The calcination and activation processes of all samples were performed at the temperature of 900°C in the argon and CO₂, respectively. For IC-CNF, the PVP-PAN weight ratios were varied as PVP-PAN: 3-7, 2-8, and 1-9 applied in the precursor solutions of the single-nozzle polymer-blend electrospinning. Moreover, the core-shell nozzle electrospinning was also used for this case. For carbon manganese oxide composite core-shell nanofibers, the PAN solution was a core solution, while the PAN mixed with metal oxide was a shell solution. By varying the shell solutions, we can get three different samples based on the weight ratios of core-shell, i.e. 10-8, 10-9, and 10-10. Concerning material characterizations, the field emission scanning electron microscopy (FE-SEM) revealed the fiber-fiber interconnection patterns, the manganese oxide nanoparticles, and other fiber morphologies. Moreover, the fiber-fiber interconnection

morphologies were observed in PVP-PAN/PAN-PVP core-shell based carbon nanofibers only, while the PVP-PAN blend did not. Furthermore, the FE-SEM results also exhibited the fiber diameters and particle sizes, which were consistent with the specific areas obtained from the N_2 -adsorption/desorption techniques. As a result, the biggest diameter was observed in CNF; and the mixture of PVP and PAN via polymer blend or core-shell electrospinning could reduce the sizes of fiber diameters. Besides, the structures of carbon-manganese oxide composite core-shell nanofibers were revealed by the cross-sectional images of the fibers, which displayed the particles staying outside on the carbon nanofibers. Furthermore, the differentiate-canning calorimetry (DSC) and the thermogravimetric analysis (TGA) displayed the thermal properties of all samples. In addition, X-ray diffraction techniques (XRD) presented the phases of amorphous carbon, graphite structure, and manganese oxides, while the Raman analysis determined the carbon qualities in the samples. Additionally, the electrochemical performances were measured by three-electrode system in 6 M KOH aqueous electrolyte. Thus, the C/MnO_x exhibited the greatest specific capacitance of 213.7 F g⁻¹ at the current density of 0.5 A g⁻¹ with the energy density of 30 W h kg⁻¹ at the power density of 249 W kg⁻¹ and the great cycling stability of 97% after 1000 cycles. These great results might be caused by the synergistic effect of EDLCs and pseudocapacitive behaviors of CNF and MnO_x because of the low charge transferred resistance and high surface area.

School of Physics

Academic Year 2018

Student's Signature Onksaphea Pech

Advisor's Signature 

ACKNOWLEDGEMENTS

This work would have not been accomplished without the helps from many people, to whom I would like to express my sincere thanks. To begin with, I would like to express my thanks to all members in AMP group; especially, I would like to express my acknowledgement to my advisor Prof. Dr. Santi Maensiri who supported me emotionally, mentally, and financially. Moreover, I would like to thank my thesis examination committee members, such as Asst. Prof. Dr. Worawat Meevasana, Asst. Prof. Dr. Theeranun Siritanon, Assoc. Prof. Dr. Prayoon Songsiririthigul, and Asst. Prof. Dr. Nonglak Meethong for their strong efforts and constructive comments on my thesis. Particularly, I also would like to thank Dr. Jessada Khajonrit for translating the abstract into Thai language.

In addition, I would like to express my sincerest appreciation to the staff of School of Physics, Institute of Science, and all relevant units of Suranaree University of Technology for all facilities. Besides, I am grateful to the SUT-PhD Scholarship for Asean Countries and the Nanotechnology Center (NANOTEC), National Science and Technology Development Agency (NSTDA), Ministry of Science and Technology, Thailand, through the Center of Excellence Network for the financial supports.

Finally, I also would like to thank my family for their loves and inspirations, which were the powerful forces to boost my mind until I am here today.

Ouksaphea Pech

CONTENTS

	Page
ABSTRACT IN THAI.....	I
ABSTRACT IN ENGLISH	III
ACKNOWLEDGEMENTS.....	V
CONTENTS.....	VI
LIST OF TABLES	X
LIST OF FIGURES	XI
LIST OF ABBREVIATIONS.....	XVI
CHAPTER	
I INTRODUCTION	1
1.1 Background and motivation	1
1.2 Objectives of the research	4
1.3 Limitation of the research	4
1.4 Location of research	5
1.5 Expected results.....	5
1.6 Outline of the thesis.....	5
II LITERATURE REVIEWS	7
2.1 Supercapacitors	7
2.1.1 Electrochemical double layer capacitors (EDLCs).....	7

CONTENTS (Continued)

	Page
2.1.2 Pseudocapacitors	9
2.2 Electrospinning technique	10
2.2.1 Electrospinning process	10
2.2.2 Application of electrospun materials	11
2.2.3 Side-by-side and multi-nozzle electrospinning.....	12
2.2.4 Core-shell electrospinning	13
2.2.5 Needleless electrospinning (NLE)	14
2.2.6 Polymers and solvent used in electrospinning	16
2.3 Carbon nanofibers (CNF).....	17
2.3.1 Why carbon nanofibers	17
2.3.2 The structure of CNF	17
2.3.3 The synthesis methods	19
2.3.4 Porous carbon nanofibers.....	19
2.3.5 Application of CNF.....	21
2.4 MnO _x	22
2.5 Carbon composite nanofibers.....	24
2.5.1 The structures of carbon composite nanofibers	24
2.5.2 The synthesis methods	25
2.5.3 Applications of CNF in supercapacitors	25

CONTENTS (Continued)

	Page
III EXPERIMENTAL PROCEDURE	30
3.1 Fabrication of CNF, P-CNF, IC-CNF, and C-MnO _x	31
3.1.1 The precursor preparation	31
3.1.2 Fabrications of the as spun nanofibers	33
3.1.3 Calcination of the as spun nanofibers	33
3.2 Material characterization	37
3.2.1 Thermogravimetric analysis (TGA)	37
3.2.2 Scanning electron microscopy (SEM).....	38
3.2.3 Transmission electron microscopy (TEM).....	40
3.2.4 X-ray diffraction (XRD).....	42
3.2.5 Gas adsorption/desorption techniques.....	45
3.2.6 Raman spectroscopy.....	49
3.3 Electrochemical measurements	51
3.3.1 Cyclic voltammetry (CV).....	52
3.3.2 Galvanostatic charge/discharge (GCD).....	56
3.3.3 Electrochemical impedance spectroscopy (EIS).....	57
IV RESULTS AND DISCUSSION	59
4.1 CNF and P-CNF	60
4.1.1 Structural and morphology characterization	60

CONTENTS (Continued)

	Page
4.1.2 Electrochemical properties of CNF and P-CNF.....	67
4.2 Interconnected carbon nanofibers (IC-CNF).....	74
4.2.1 Structural and morphology characterization	74
4.2.3 Electrochemical properties	86
4.3 Carbon-manganese oxide composite nanofibers (C-MnOx).....	94
4.3.1 Structural and morphology characterization	94
4.3.2 Electrochemical properties.....	106
V CONCLUSIONS AND SUGGESTIONS.....	115
5.1 The structure and morphology characterization.....	115
5.2 The electrochemical properties	117
5.3 Suggestions.....	119
REFERENCES	121
APPENDIX.....	151
CURRICULUM VITAE.....	154

LIST OF TABLES

Table	Page
2.1 The synthesis methods, testing condition and specific capacitances of carbon based composite nanofibers	26
3.1 List of materials used as starting materials for CNF, P-CNF, IC-CNF, and C/NO _x preparation, quoting their source and purity.....	32
4.1 The textural parameter CNFs and PCNFs obtained by BET, BJH, and MP methods	67
4.2 The textural parameter of CNFs and PCNFs obtained by BET, BJH, and MP methods	72
4.3 Average diameters of all nanofibers and textural parameters of the samples obtained by BET, BJH, and MP methods	84
4.4 The values of R _s and R _{ct} of C_3-7, C_2-8, C_1-9, CS-PVP, and CS-PAN	92
4.5 Average diameters of all nanofibers and particle size of MnO _x embedded in nanofibers	101
4.4 The values of charge transfer resistances, equivalent series resistances, and N values of the samples.....	113

LIST OF FIGURES

Figure	Page
1.1	Regone plot of various energy storage devices.....2
2.1	Scheme of (a) supercapacitor and (b) electric double layer of porous electrode which electric charges are accumulated at the surface of electrode9
2.2	The side-by-side electrospinning system13
2.3	The four-nozzle electrospinning system13
2.4	The core-shell electrospinning system14
2.5	The needleless electrospinning system15
2.6	Various structures of carbon nanofibers: (a) multi-walled CNFs, (b) graphene platelet, (c) graphene fishbone, (d) graphene ribbon and (e) stacked cut CNFs, and (f) amorphous CNF without graphene layers.....18
3.1	Procedure of preparation of all samples.....35
3.2	The homemade single/core-shell electrospinning machine35
3.3	The flowchart displaying the fabrication and characterization of all Samples36

LIST OF FIGURES (Continued)

Figure	Page
3.4	(a) Schematic representation of SEM of a sample and (b) the scattering of primary electron by the sample. High-energy backscattered electrons are generated in the membrane (BSEM) and the sample (BSEs). Low-energy secondary electrons are generated in membrane (SEM and SEBM) and sample (SES)39
3.5	Scanning electron microscope39
3.6	The schematic outline of TEM41
3.7	Transmission Electron Microscopes42
3.8	Bragg's law44
3.9	X-ray diffractometer45
3.10	The IUPAC classification of adsorption isotherms49
3.11	The photo of BET, BEL SORP MINI II JAPAN.....50
3.12	The photo of BRUKER RAM II VERTEX 7051
3.13	Experimental set up of electrochemical measurements, which consist of personal computer, potentiostat/galvanostat, and electrochemical cell.....52
3.14	The view of the Nova-1.11 software analyzing CV curve.....52
3.15	Cyclic voltammogram of three different electrochemical capacitors: ideal, resistive, faradaic capacitors53
4.1	TGA (a) and DSC (b) of as-spun-PAN nanofibers61

LIST OF FIGURES (Continued)

Figure	Page
4.2	The XRD pattern of CNF with the standard62
4.3	The SEM images of CNF (a), (b), and (c), and P-CNF (d), (e), and (f) at different magnifications64
4.4	(a) N ₂ adsorption and desorption isotherm of the samples. (b) Micropore distributions of the samples and (insert) mesopore and macropore distribution of the samples.....66
4.5	CV curves of both samples at scan rate (a) 500 mV s ⁻¹ and (b) 2 mV s ⁻¹ ; the plot of specific capacitance as a function of scan rates (c) and current densities (d).....69
4.6	The GDC curves of both samples at the current density of 0.5 A g ⁻¹ and (b) 10 A g ⁻¹ ; (c) Ragone plots of both samples, and (d) capacity retention71
4.7	The Nyquist impedance plots at a frequency range of 0.1 Hz-100 kHz in 6 M KOH electrolyte solution of CNF and P-CNF electrodes73
4.8	The TGA (a) and DSC (b) curves of PAN ₃₋₇ , PAN ₂₋₈ , PAN ₁₋₉ , CS-PVP, and CS-PAN nanofibers76
4.9	The XRD patterns of C ₃₋₇ , C ₂₋₈ , C ₁₋₉ , CS-PVP, and CS-PAN and the references patterns.....78
4.10	The Raman spectra of C ₃₋₇ , C ₂₋₈ , C ₁₋₉ , CS-PVP, and CS-PAN and the references patterns.....80

LIST OF FIGURES (Continued)

Figure	Page
4.11 The SEM images of (a) CNF, (b) C_3-7, (c) C_2-8, (d) C_1-9, CS-PVP, and (e) CS-PAN.....	82
4.12 (a) N ₂ adsorption and desorption isotherm; (b) micropore distributions and (insert) mesopore and macropore distribution of C_1-9, CS-PVP, and CS-PAN.....	85
4.13 The CV curves at the scan rate of (a) 500 mV/s and (b) scan rate 5 mV/s; the plots of specific capacitances vs (c) scan rate and (d) current density of C_3-7, C_2-8, C_1-9, CS-PVP, and CS-PAN.....	88
4.14 The discharge curves at the current density of (a) 10 A g ⁻¹ and (b) 0.5 A g ⁻¹ ; the Ragone plots (c) and (d) capacity retentions of C_3-7, C_2-8, C_1-9, CS-PVP, and CS-PAN.....	90
4.15 The Nyquist plot (a) and (b) enlargement of Nyquist plot of C_3-7, C_2-8, C_1-9, CS-PVP, and CS-PAN.....	93
4.16 The DSC (a) and TGA (b) of PAN-MnO ₁₀₋₈ , PAN-MnO ₁₀₋₉ , and PAN-MnO ₁₀₋₁₀	95
4.17 The XRD spectra of C-Mn ₁₀₋₈ , C-Mn ₁₀₋₉ , and C-Mn ₁₀₋₁₀	97
4.18 Raman spectra of C-Mn ₁₀₋₈ , C-Mn ₁₀₋₉ , and C-Mn ₁₀₋₁₀	99
4.19 The FE-SEM of (a) C-Mn ₁₀₋₈ , (b) C-Mn ₁₀₋₉ , and (c) C-Mn ₁₀₋₁₀ at the magnification of 5 kX and (d) C-Mn ₁₀₋₈ , (e) C-Mn ₁₀₋₉ , and C-Mn ₁₀₋₁₀ at the magnification of 50 kX.....	102

LIST OF FIGURES (Continued)

Figure	Page	
4.20	The FE-SEM images of cross-sectional fibers of (a) and (c) C-Mn ₁₀₋₈ , (b) the enlargement of C-Mn ₁₀₋₈ , (d) C-Mn ₁₀₋₉ , (e) C-Mn ₁₀₋₁₀ , and (f) the enlargement of C-Mn ₁₀₋₁₀	103
4.21	The isotherm curve (a), MP plot (b), and BJH (inset (b)) of C-Mn ₁₀₋₈	105
4.22	The CV curves at the scan rate of (a) 5 mV s ⁻¹ and (b) 500 mV s ⁻¹ ; (c) the plots of specific capacitances versus scan rate, and the Regone plots of the samples	109
4.23	The CD curves at the current density of (a) 10 A g ⁻¹ and (b) 0.5 A g ⁻¹ ; (c) the Regone plots and (d) capacity retention.....	111
4.24	The Nyquist plot (a) and enlargement of Nyquist plot (b) of all samples	114

LIST OF ABBREVIATIONS

BET	=	Brunauer-Emmett-Teller
BJH	=	Barrett-Joyner-Halenda
CV	=	Cyclic voltammetry
DSC	=	Differentiate-scanning Calorimetry
EDLCs	=	Electric double-layer capacitors
EIS	=	Electrochemical impedance spectroscopy
GCD	=	Galvanostatic charge/discharge
NMP	=	N-Methyl-2-pyrrolidone
PAN	=	Polyacrylonitrile
PVDF	=	Polyvinylidene fluoride
PVP	=	Polyvinylpyrrolidone
SEM	=	Scanning electron microscopy
TEM	=	Transmission electron microscopy
TGA	=	Thermal gravimetric analyzer
XANE	=	X-ray absorption near edge structure
XAS	=	X-ray absorption spectroscopy
XRD	=	X-ray diffraction

CHAPTER I

INTRODUCTION

1.1 Background and motivation

Recently, energy shortage is the hot topic to be considered due to the decreasing natural resources, rapidly increasing demands, and environmental issues. Renewable energy has become a preferable candidate to deal with this problem. However, renewable energies, such as solar power (López-Lapeña and Pallas-Areny, 2018) and wind power (Willis *et al.*, 2018) depend very much on natural conditions. For example, the sunlight can be obtained only at a daytime, and the wind occurs unstably. Therefore, high efficient and reliable energy storage devices are the hearts of the renewable energy application (Aneke and Wang, 2016). To date, energy storage devices including batteries (Blecua *et al.*, 2017), fuel cells (Abdelkareem *et al.*, 2019), capacitors, and supercapacitors (Agyemang *et al.*, 2018) have been interested and developed. Among them, supercapacitors have been chosen as one of the promising energy storage devices used in the renewable energy technology because of their high power densities, long cycle lives, fast charging/discharging rates, and high stabilities in operation (Akinwolemiwa *et al.*, 2017). Beside this, supercapacitors can also be used in the other applications like hybrid vehicles and portable electronic devices. Base on their energy storage mechanisms, there are two types of supercapacitor: (a) the electrical double layer capacitors (EDLCs), which store energy by pure electrostatic attraction between by reversible faradaic reaction including surface adsorption/desorption process

between electrodes and electrolytes (T.-L. Chen and Elabd, 2017). More literature reviews about supercapacitors were summarized in chapter II. Generally, carbon materials with high surface areas are used as electrodes of EDLCs, which provide fast charging/discharging process resulting in high power density and excellent cycling stability. There are various patterns of carbonaceous materials, such as graphene, activated carbon, carbon aerogels, template derived carbons, carbon nanotubes, and carbon nanofibers (Zhai *et al.*, 2011). Electrospun carbon nanofibers (CNF) have been fabricated by electrospinning followed by carbonization and activation process, and they have been considered as electrode material because of certain features including nanoscale size, freestanding nature, easily added reinforcement, and simplified process. Moreover, CNF can provide a faster ion response because of the reduced ion transport paths compared with carbon particles; and it does not need any binder which can block the pores and increase the electrode resistance (Inagaki *et al.*, 2012).

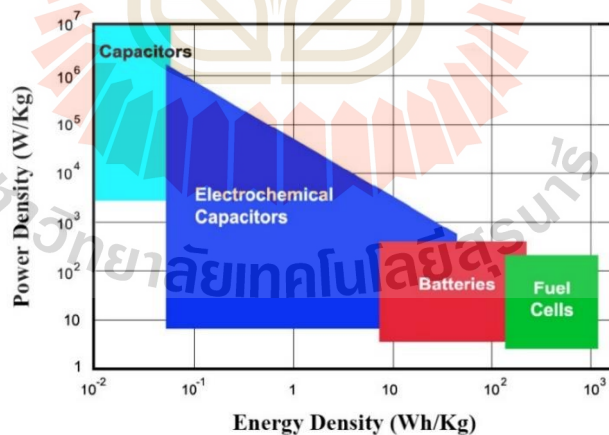


Figure 1.1 Ragone plot of various energy storage devices [Adapted from (Goodenough *et al.*, 2007)].

To improve the specific capacitance of EDLCs, surface area and conductivity are important factors. Moreover, the specific capacitance of supercapacitor can be enhanced by summing up the EDLCs and pseudo capacitors to get both benefits (T.-L.

Chen and Elabd, 2017). Some transition metal oxides have been reported to be used to embed in carbon nanofibers, such as nickel oxide, cobalt oxide, vanadium oxide, titanium oxide, copper oxide, ferrite oxide, ruthenium oxide (C. Yuan *et al.*, 2014). Among these, ruthenium oxide has a high specific capacitance; however, the cost is still expensive that is why the cheaper manganese oxide becomes an interesting materials for energy storage devices (Barai *et al.*, 2017). The more details about CNF and manganese oxide will be found in chapter II (Literature review).

In this study, carbon nanofibers (CNF), porous carbon nanofibers (P-CNF), interconnected carbon nanofibers (IC-CNF), and carbon/carbon-manganese oxide composite nanofibers (C/MnO_x) were fabricated by a single-nozzle and core-shell-nozzle electrospinning technique followed by carbonization and CO₂-activation process. The precursor solutions for CNF, P-CNF, IC-CNF, and C/MnO_x were prepared by using polyacrylonitrile (PAN), PAN and paraffin oil, PAN and polyvinylpyrrolidone (PVP), and PAN and manganese nitrate dissolving in N, N-dimethylformamide (DMF), respectively. The more details of solution preparations and sample fabrications will be found in chapter III (Research Methodology). The prepared nanofibers were characterized by various techniques including, X-ray diffraction (XRD), scanning electron microscopy (SEM), field emission scanning electron microscopy (FE-SEM), transmission electron microscopy (TEM), and gas absorption technique (Lin *et al.*, 2018). Moreover, the electrochemical properties of the samples were also studied.

1.2 Objectives of research

The general objective of this PhD thesis is to contribute the collective knowledge in the preparation, characterization, and electrochemical properties of CNF, PCNF, IC-CNF, and CNF/MnO_x. In overall, the major scientific and technical objectives of the thesis involve:

- 1.2.1 To synthesize CNF, PCNF, IC-CNF, and CNF/MnO_x by single nozzle and core-shell nozzle electrospinning followed by heat treatment method.
- 1.2.2 To study the effects of the polymeric concentrations on the structures and morphologies of the nanofibers.
- 1.2.3 To study the electrochemical properties of the nanofibers for energy storage application.

1.3 Limitations of the research

- 1.3.1 This study focuses on the fabrications of carbon-based nanofibers including porous and interconnected carbon nanofibers and CNF reinforced with MnO_x nanoparticle.
- 1.3.2 The samples were calcined at 900 °C for 2h in inert gas atmosphere and directly activated by CO₂ for 20 min.
- 1.3.3 The morphologies, structures, and electrochemical properties of all samples are compared with those of the pure CNF.
- 1.3.4 Investigation of the electrochemical properties of the fabricated electrodes was studied by cyclic voltammetry (CV), galvanostatic

charge/discharge (GCD) and electrochemical impedance spectroscopy (EIS).

1.4 Locations of research

- 1.4.1 Advanced Materials Physics Laboratory (AMP), School of Physics, Institute of Science, Suranaree University of Technology (SUT), Nakhon Ratchasima, 30000 Thailand.
- 1.4.2 The Center for Scientific and Technological Equipment (SUT), Suranaree University of Technology (SUT), Nakhon Ratchasima, 30000 Thailand.

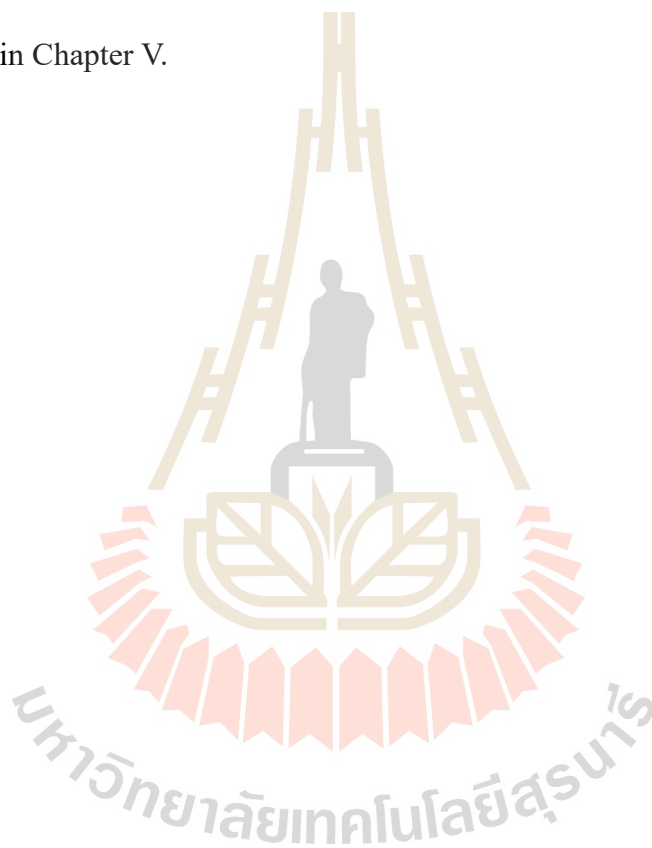
1.5 Expected results

- 1.5.1 Skill and expertise for synthesis, fabrication and characterization techniques for CNF, PCNF, IC-CNF, and CNF/MnO_x with the improved properties for electrode material of supercapacitors.
- 1.5.2 Understanding of the electrochemical properties of the CNF, PCNF, IC-CNF, and CNF/MnO_x
- 1.5.3 International publications (ISI).

1.6 Outline of the thesis

This thesis is divided into five chapters. The first chapter provides the introduction of the thesis. In the next chapter (chapter II), a brief review of information concerning with background of CNF, manganese oxides, electrospinning/core-shell electrospinning technique, the theory approach concerning with electrochemical

properties are also detailed in this chapter. Chapter III presents chemical and experimental method of the CNF, PCNF, IC-CNF, and CNF/MnO_x. Moreover, this chapter also presents the fabrication techniques. Furthermore, the informations of all measurements techniques used in this research are also summarized in this chapter. Then, the results obtained in this research and discussions of the results are given in Chapter IV. Finally, conclusions and suggestions are described, and the future works are proposed in Chapter V.



CHAPTER II

LITERATURE REVIEWS

2.1 Supercapacitors

Supercapacitors, also known as electrochemical capacitors or ultracapacitors, are energy storage devices which have high power density, long cycle life, fast charging/discharging rate, and long term operation stability (Y. Huang, F. Cui, *et al.*, 2018). There are many applications for supercapacitors including portable electronic devices, hybrid vehicles, and power backup systems (Sun *et al.*, 2017). Supercapacitor comprises of a negative electrode (negatrode), aqueous/non-aqueous electrolyte, separator and a positive electrode (positrode) (Akinwolemiwa *et al.*, 2017). Based on the energy storage mechanism, supercapacitors can be classified into two types: the electrochemical double-layer capacitors (EDLCs) and pseudocapactors (Y. Huang, Y. Zhao *et al.*, 2018).

2.1.1 Electrochemical double layer capacitors (EDLCs)

The formation of electrochemical double layer capacitor (EDLCs) consists of two-identical electrodes immersed in an aqueous or an organic electrolyte and separated by the separator. The electrochemical capacitors have a very similar structure as an electrochemical cell but there is no electron transfer across the interface. The energy storage mechanism of EDLDs is based on the reversible electrostatic accumulation of ions on the surface of electrode and electrolyte (Sarwar *et al.*, 2016). Figure 2.1(a) shows a typical double-layer capacitor. Due to Coulomb's force positive charges

accumulated on the positive electrode attract an equal number of negative charges around the electrode in the electrolyte side. Another double-layer is formed at the negative electrode-electrolyte interface to insure the electric neutrality of the system by the charges accumulated at electrode and positive charges in the electrolyte near the interface. Therefore, two electric double-layers are formed in a complete electrochemical double-layer capacitor, one at the negative electrode-electrolyte interface and another at the positive electrode-electrolyte interface (Jeong and Kim, 2018). Generally, EDLCs are known as symmetric supercapacitors, which their electrodes are carbon material. High-surface-area carbons, such as activated carbons are qualified as electrode materials for EDLCs (Lee *et al.*, 2016). It is noticed that the useful surface areas are where the electrolyte ions can access only which can form electrode electrolyte double-layers [see Figure 2.1(b)]. Therefore, the pore sizes of electrode materials must be optimized to fit the sizes of the electrolyte ions. However, if the porosity of electrode material is too high, the electric conductivity electrode will be low and it will decrease the power density of the supercapacitor (Dupont and Donne, 2016). The capacitance, the energy, and the maximum instantaneous power are calculated by the following equations, respectively.

$$C = \frac{\epsilon_r \epsilon_0 A}{d} \quad (1)$$

$$E = \frac{1}{2} CV^2 \quad (2)$$

$$P_{\max} = \frac{V^2}{4R} \quad (3)$$

where ϵ_0 is the dielectric constant of the vacuum, ϵ_r is the dielectric constant of the electrolyte, A is the accessible surface area, d is the separation between charge, C is the capacitance, V is the cell voltage, R is the internal resistance (González *et al.*, 2016).

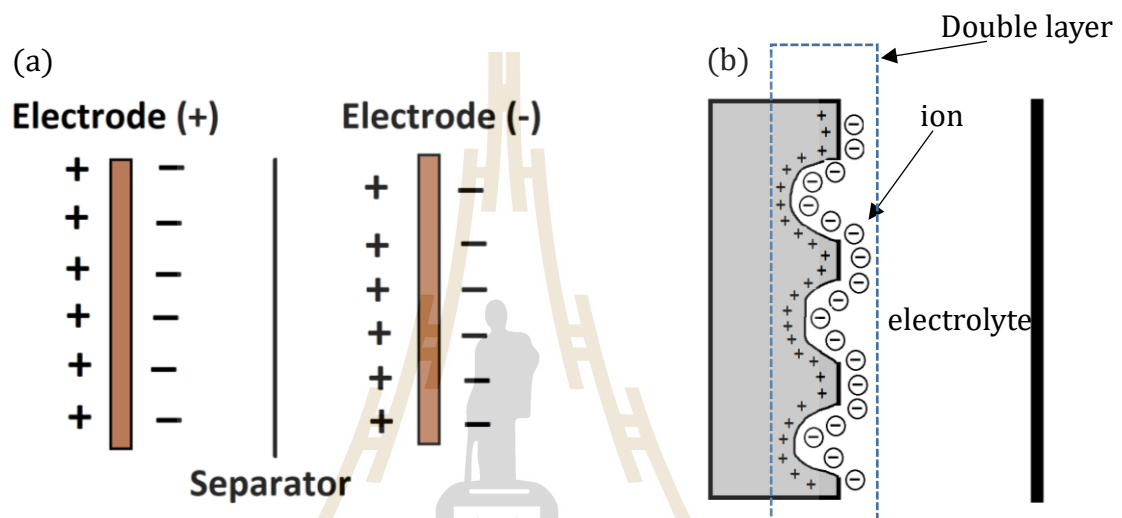


Figure 2.1 Scheme of (a) supercapacitor and (b) electric double layer of porous electrode, which electric charges are accumulated at the surface of electrode.

2.1.2 Pseudocapacitors

The same as EDLCs, a pseudocapacitor also consists of two identical electrodes immersed in an aqueous or an organic electrolyte and separated by the separator. However, the charge storage of pseudocapacitors is different from EDLCs. Pseudocapacitors store energy by a faradaic charge transfer in the electrode layer, which occurs through electrochemical reduction-oxidation (redox) reaction (Xiao *et al.*, 2017). The active materials for pseudocapacitors are metal oxide/hydroxide and conductive polymer. Since the faradic electrochemical processes occur both on the

surface and in the bulk near the surface, pseudocapacitors usually exhibit larger specific capacitance than EDLCs. The behavior of this redox reaction is similar to the electrochemical reactions in the rechargeable batteries. The redox reaction in an electrode layer must be electrochemically reversible or semi-reversible to ensure efficient charge and discharge (Dupont and Donne, 2016). The electrodes of pseudocapacitors are usually composed of a reversible electrochemical active material and electrochemically inert material like carbon material. In electrochemically reversibility, the electroreduction and electrooxidation of a pseudomaterial's oxidation states can occur at almost the same potentials. However, most of redox reactions are not totally reversible because of their limited reaction kinetics, particularly if the reactions are driven at high rates. The redox reactions must occur within the stability region of the electrolyte in order for a pseudocapacitive material to be used for storage (Miller, 2017).

2.2 Electrospinning techniques

2.2.1 Electrospinning process

In electrospinning process, the solution of polymer or melt is stretched to form fine fibers with thinner diameter (from nanometer to micrometer) and larger surface area than the fibers obtained from conventional spinning process by using electrostatic force (Alazab *et al.*, 2017). Similar to electrostatic precipitators and pesticide sprayers, DC high voltage in the range of several kVs is used to produce strong mutual electric repulsive force overcome weaker force of surface tension in the charged polymer liquid (You *et al.*, 2017). There are two types of electrospinning setups, i.e. vertical and horizontal. Recently sophisticated systems have been developed to operate in room

temperature and ambient condition. The three main components of electrospinning system comprise a spinneret, a high-voltage power supply, and a grounded collector (Soares *et al.*, 2018). Some parameters, which affect the quality of productive nanofibers, include processing parameter, such as applied voltage, feed rate/flow rate, types of collector, tip to collector distance and ambient parameters like humidity, temperature etc. (Gee *et al.*, 2018). In general, there are two types of electrospinning including melt electrospinning (Abdal-hay *et al.*, 2018) and solution electrospinning (Alazab *et al.*, 2017). Normally, melt electrospinning has rarely been used since it cannot provide nanoscale fibers, which are needed in the applications, and it requires advanced equipment, high viscosity, and high heating temperature (H. Xu *et al.*, 2018). On the other hand, the solution electrospinning is more preferable even there are some disadvantages including the toxicity of the solution to the environment. The solution electrospinning technique could be developed by adding the photopolymerization in the spinning process (X. Zhu *et al.*, 2018).

2.2.2 Applications of electrospun materials

There are many literatures reported the applications of electrospun materials. First, they can be applied in the medical applications, such as drug delivery and regenerative medicine (S. Chen *et al.*, 2018), tissue engineering (Alharbi *et al.*, 2018), and bone tissue engineering (G. Cheng *et al.*, 2018). Second, they have been used in the environmental applications including the oil-water separation (Bae *et al.*, 2018), water filtering (J. Huang *et al.*, 2018), photocatalytic water purification (J. Huang *et al.*, 2018), membranes (K. Zhang *et al.*, 2018), and air filtering (Z. Cheng *et al.*, 2018). Third, they are utilized in Biopolymer and food productions like the productions of food proteins and polysaccharides (Mendes *et al.*, 2017) and food hydrocolloids (C.

Zhang *et al.*, 2018). Next, they are found in the sensor applications, including gasochromic hydrogen detection (Tavakoli Foroushani *et al.*, 2018), electromagnetic wave absorption (Wei *et al.*, 2018), formaldehyde sensor (X. Gao *et al.*, 2018), humidity sensor (T. Yuan *et al.*, 2018). Finally, they can be applied in the energy storage applications, such as electrode materials for supercapacitors (W.-M. Chang *et al.*, 2018), materials for lithium-ion battery (Q. Chen *et al.*, 2015), dye-sensitized solar cells (X. Zhang *et al.*, 2018), materials for advanced lithium-sulfur batteries (Lu Li *et al.*, 2018), sodium-ion batteries (Q. Zhu *et al.*, 2017).

2.2.3 Side-by-side and multi-nozzle electrospinning

To spin two or more solutions at the same time, side-by-side and multi-nozzle electrospinning have been developed. Niu (Niu, 2012) used side-by-side electrospinning system to spin the two different polymer solutions, i.e. PVP solution and PAN solution. The schematic diagram of side-by-side electrospinning was illustrated in figure 2.2. Simprachim (Sinprachim *et al.*, 2016) used four-nozzle electrospinning system to spin PAN solution and PAN-metal-nitrate solutions. The fiber-mat product could be obtained much greater than the single-nozzle electrospinning system at the same time. The schematic diagram of four-nozzle electrospinning system was displayed in Figure 2.3.

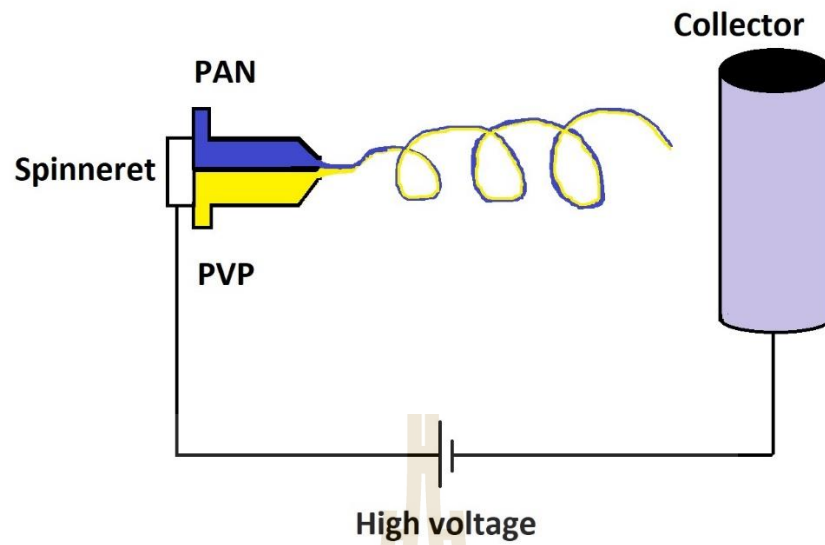


Figure 2.2 The side-by-side electrospinning system.

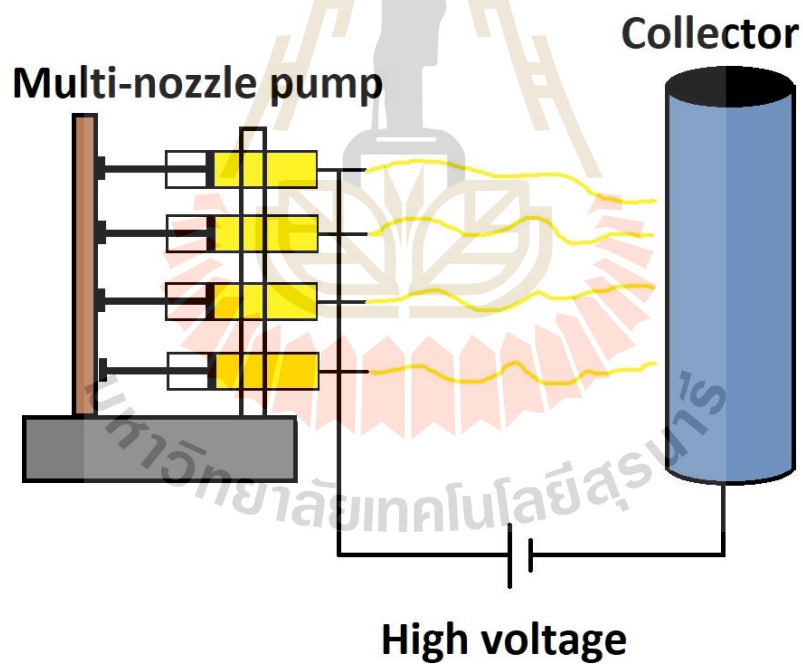


Figure 2.3 The four-nozzle electrospinning system.

2.2.4 Core-shell electrospinning

Figure 2.4 illustrates a basic setup for core-shell electrospinning, which includes two syringes and coaxial spinneret. Similar to conventional electrospinning, under high voltage the electrospinning liquid is drawn out from spinneret and form a ‘compound

Taylor cone' with a core-shell structure (Gadkari, 2014). The core-shell structure in fibers will be built and kept through spinning and collected on the rotating 'collector'. In those processes, core-shell Taylor cone formation will decide the core-shell nanofibers forming (Huang *et al.*, 2013). In order to get a nice 'compound Taylor cone' with core-shell structure, one has to make an utmost control and balance inject speed of inner and outer fluid, which keep the 'compound Taylor cone' in dynamic stabilization (Babapoor *et al.*, 2017). A too high or too low flow rate of the inner fluid is unfavorable. An appropriate injecting speed and rate of inner-outer fluid should be considered and investigated carefully to have good core-shell structure fibers (Yu *et al.*, 2014).

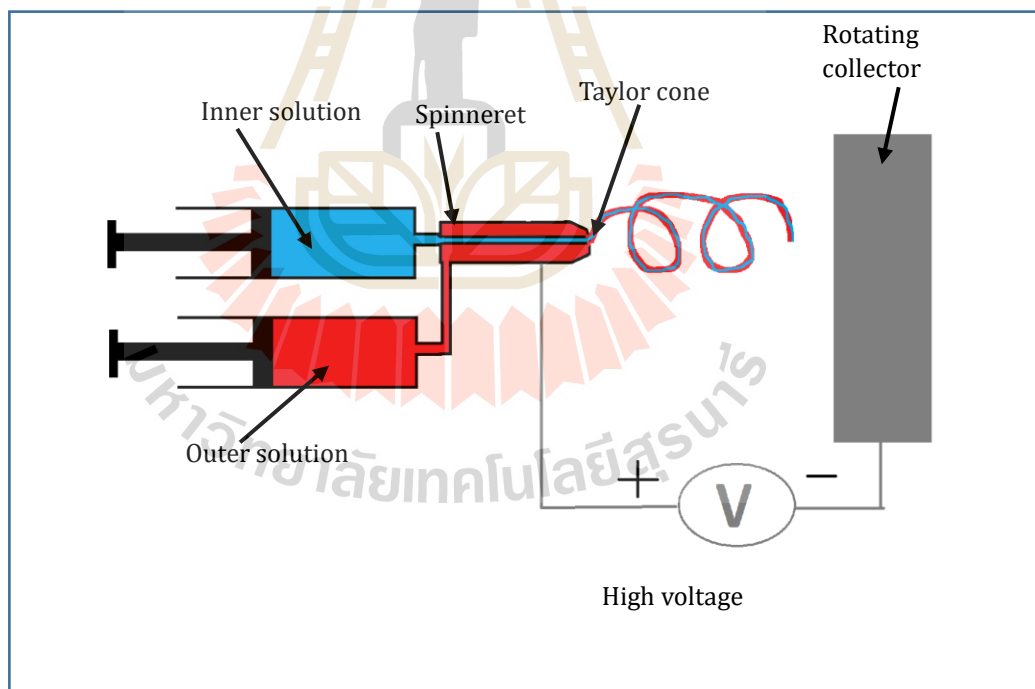


Figure 2.4 The core-shell electrospinning system.

2.2.5 Needleless electrospinning (NLE)

Similar to conventional, side-by-side, the multi-nozzle, and core-shell electrospinning, the electrospinning solution is drawn out from spinneret under high

voltage by the repulsive force of electric charge on the surface of the solution and form a ‘compound Taylor cone’. On the other hand, the spinning parameter are quite different from the conventional one. For instance, the distance between the Taylor cone and collector is very short about 140 mm; the speed of rotating bath is very low about 10 rpm; and voltage is extremely high in the range of 70-75 kV.

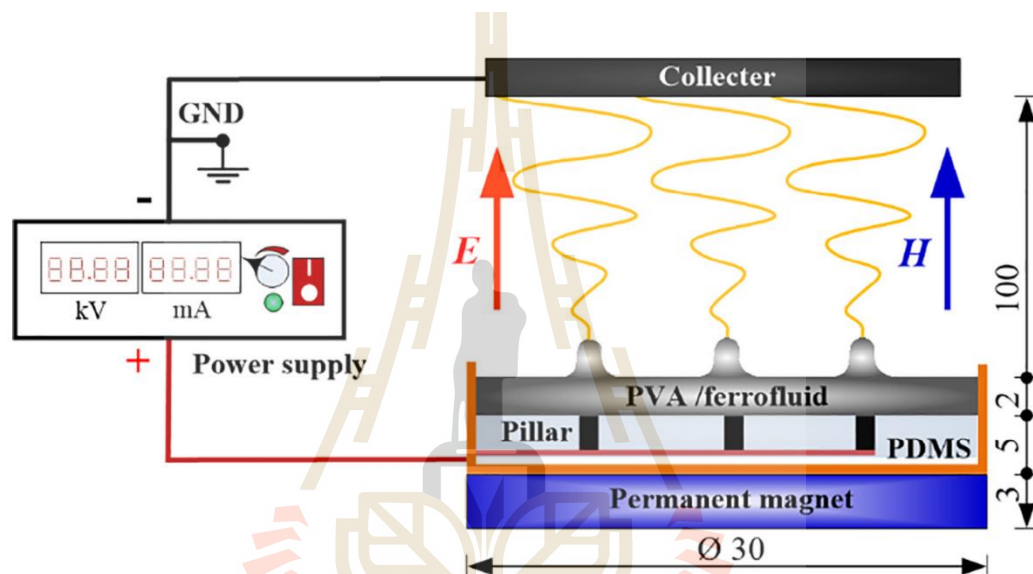


Figure 2.5 Needleless electrospinning system (adapted from (Hongjian Wang *et al.*, 2018)).

Nanofibers obtained from this technique meet the requirement of many application (Streckova *et al.*, 2018). In NLE, a very high voltage about 28 kV is needed to form a Taylor cone and produce the continuously-spinning fiber jet (Hongjian Wang *et al.*, 2018). The schematic representation of NLE was presented in Figure 2.5.

2.2.6 Polymers and solvents used in electrospinning

There are many kinds of polymers having been used in electrospinning. Some polymers are water-soluble including polyvinylpyrrolidone (PVP) (Castkova *et al.*, 2017), polyacrylic acid (PAA), polyvinyl alcohol (PVA) (Bose and Sanyal, 2018), poly(vinyl acetate) (PVAc), polyethylene oxide (PEO) (Dobrovolskaya *et al.*, 2018). On the other hand, some polymers are not-water-soluble like polyacrylonitrile (PAN) (Z.-X. Huang *et al.*, 2018), polyimide (PI) (Lasprilla-Botero *et al.*, 2018), polyamide 66 (PA66) (Z. Cheng *et al.*, 2018), poly(vinylidene fluoride) (PVDF)(Amini *et al.*, 2018), polymethacrylate (PMMA) (J. Bai *et al.*, 2018), polyvinylchloride (PVC), polylactic acid (PLA) (Coimbra *et al.*, 2019), polyurethanes (PU), polybenzimidazol (PBI), polycarbonate (PC), polyethylene-co-vinyl acetate (PEVA), polyaniline (PANI), polyethylene dioxythiophene (PEDOT) (Zarrin *et al.*, 2018), polyvinylcarbazole, polyethylene terephthalate (PET), polycrylic acid-polypyrene methanol (PAA-PM), polyvinylchloride (PVC), cellulose acetate (CA) (Bae *et al.*, 2018), polyacrylamide, (PAAm), collagen (Le Corre-Bordes *et al.*, 2018), polycaprolactone (PCL) (Morikawa, 2018), poly(2-hydroxyethyl methacrylate (HEMA), poly(ethylene-co-vinyl alcohol), polyethylene terephthalate (PET), and polyethylene naphthalate (PEN). The solvents used to solube these polymers include dimethyl formamide (DMF) (W.-M. Chang *et al.*, 2018), formic acid, dimethyl acetamide, chloroform, tetrahydrofuran, methylene chloride, acetic acid (Kwak *et al.*, 2017), dichlormethane, acetone (Kang and Kang, 2018), ethanol (Isik *et al.*, 2018), methanol (Someswararao *et al.*, 2018), isopropyl alcohol, camphor sulfonic acid, hexafluoro-2-propanol (Fang *et al.*, 2018).

2.3 Carbon nanofibers

2.3.1 Why carbon nanofibers?

Carbon materials are very attractive candidates for energy storage devices; especially supercapacitors due to their certain factors. They include different allotropes, various dimensionality (from 0 to 3D), existence in different forms (powders, fibers, foams, etc.), good conductivity (Jiandong Liu 2018), high surface area (Y. Bai *et al.*, 2018), low cost (Alvi and Akhtar, 2016), environmentally friendly (Alvi and Akhtar, 2016), operation in wide range of temperature (Chesnokov *et al.*, 2016), and abundant element (J. Cai *et al.*, 2016). Carbon nanofibers fabricated by combination of electrospinning technique and carbonization process have been considered as a promising candidate for energy storage application due to the nanoscale tubular morphology, which can offer a unique combination of low electrical resistivity and high porosity (Agyemang *et al.*, 2018). The specific surface area of carbon nanofibers can be improved by activation process which can be classified into chemical activation (Bao *et al.*, 2018) and physical activation (Liu *et al.*, 2013). Moreover, it is easy to put enforcements. For example, metal oxide can be imbedded into carbon nanofibers by just adding the metal source into the solution before doing electrospinning. This is a simple and low-cost technique, which can control pore structure, degree of graphitization, electrical conductivity and metallic species loading of carbon nanofibers (Alegre *et al.*, 2018).

2.3.2 The structure of CNFs

Carbon nanofibers (CNFs) are one-dimensional (1D) nanostructured carbon materials with nanometer-size diameters. For example, continuous carbon nanofibers assembled as a non-woven web of interchanged fibers are fabricated via electrospinning

and subsequent thermal treatment. The carbon nanofibers (CNFs) are distinguished from conventional carbon fibers (CFs) by smaller-size diameters. The CF diameters are in order of several micrometers while CNFs have diameters of 50-300 nm. The unique properties include huge surface area, good electrical conductivity, and high chemical stability in different solution at wide temperature range (LichaoFeng *et al.*, 2014). There are many types of structure of carbon nanofibers including graphite, fullerene, and amorphous carbon. The degree of graphitization affects strongly the electrochemical properties of carbon nanofibers. The high temperature is used in carbonization process to obtain the graphitization structure by the rearranging of carbon atoms (B. Zhang *et al.*, 2016). The various types of nanostructure of carbon nanofibers are displayed in figure 2.6.

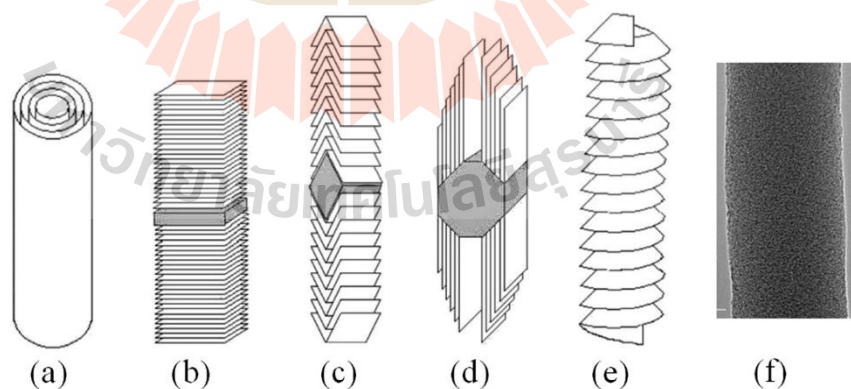


Figure 2.6 Various structures of carbon nanofibers: (a) multi-walled CNFs, (b) graphene platelet, (c) graphene fishbone, (d) graphene ribbon and (e) stacked cut CNFs, and (f) amorphous CNF without graphene layers (B. Zhang *et al.*, 2016).

2.3.3 The synthesis methods

Various methods have been employed to synthesize CNFs including traditional vapor growth method or plasma enhanced chemical vapor depositing method (J.-Y. Choi *et al.*, 2018) and the combination of electrospinning of polymer and carbonization method (Dincer *et al.*, 2018). Among these methods, the combination of electrospinning for forming fiber mat and the carbonization process for converting material to become CNF under an inert gas atmosphere is the most preferable method because of uncomplicated process and low cost. In electrospinning method, the polymer solution was stretched as continuous fibers by applied electric field. As a result, a mat or web of fibers is collected for further heat treatment to obtain carbon nanofibers mat or web. Moreover, the web or mat structure of fibers is a good form for electrode materials of energy storage devices due to the easy transport of electric charge and accessibility of electrolyte ions (W.-M. Chang *et al.*, 2018). There are several materials used for commercial carbon nanofibers, such as polymers (PAN, PVA), rayon, and pitch and so on. Among these, Polyacrylonitrile (PAN) has been widely used because of its high carbon yield and thermal stability. By using PAN via electrospinning method and carbonization at certain condition, some factors can be controlled like pore structure, degree of graphitization, electrical conductivity (Arbab *et al.*, 2017).

2.3.4 Porous carbon nanofibers

In the electrochemical applications, the electrical conductivity and the surface area have been set as the first priority. Thus, CNF fabricated by electrospinning and carbonization process meet the requirement due to their large surface area and high electrical conductivity (Busacca *et al.*, 2017). Moreover, the specific area of CNF can be improved by activation including Physical (Che Othman *et al.*, 2017) and Chemical

activation (Byamba-Ochir *et al.*, 2016) to produce more mesopores and micropores, which are useful for increasing specific capacitance (Byamba-Ochir *et al.*, 2016). There are many literatures published about how to make porous carbon nanofibers. For example, An (An *et al.*, 2016) fabricated mesoporous carbon nanofibers by using electrospinning and H₂-activation with the specific area of 467.6 m² g⁻¹. Besides, Bai (Bai *et al.*, 2014) fabricated the porous carbon nanofibers by electrospinning followed by steam activation and treatment in HNO₃/H₂SO₄ mixture with the specific surface area of 583 m² g⁻¹. Next, Deng (Deng *et al.*, 2017) prepared the honeycomb like hierarchical porous carbon nanofiber by electro-blown spinning technique. Another example, Dong (Y. Dong *et al.*, 2015) fabricated mesoporous graphitic carbon nanofibers by electrospinning and templated method with high specific area of 870 m² g⁻¹. Then, Fan (Fan *et al.*, 2016) prepared nitrogen-enriched meso-macroporous carbon fibers network by electrospinning followed by pyrolysis and SiO₂ removal processes. More example, Zuniga (Zuniga *et al.*, 2016) prepare multichannel hollow structure of TiO₂/carbon composite nanofibers by forcespinning followed by carbonization process with the specific surface area of 123.31 m² g⁻¹. In addition, Zhang (Zhang *et al.*, 2017) prepared nitrogen-doped biomass-derived carbon nanofibers/graphene aerogel via hydrothermal self-assembly method and followed by freeze-drying and carbonization. Also, Zhang (Lijun Zhang *et al.*, 2016) fabricated three-dimensional nitrogen and boron co-doped porous carbon nanofibers by a combination of electrospinning and carbonization process. Moreover, Zhang (Lijuan Zhang *et al.*, 2016) prepared hierarchical porous carbon nanofibers by electrospinning followed by carbonization process with the specific area of 679 m² g⁻¹. Besides, Zeng (Zeng *et al.*, 2015) prepared free-standing mesoporous electrospinning carbon nanofibers web without activation by

a combination of electrospinning and carbonization process with specific area of $535 \text{ m}^2 \text{ g}^{-1}$. Furthermore, Yoo (Yoo *et al.*, 2017) synthesized porous carbon nanofibers with bamboo-like carbon nanofibers branches by one-step carbonization process. Next, Yao (Yuechao Yao *et al.*, 2017) fabricated nitrogen-enriched hierarchically porous carbon nanofibers network by electrospinning followed by heat and acid treatment with specific area of $559 \text{ m}^2 \text{ g}^{-1}$. In addition, Yang (K. S. Yang *et al.*, 2015) prepared RuO₂-containing activated carbon nanofibers with hollow cores by one –step electrospinning followed by thermal treatment. Lastly, Xu (J. Xu *et al.*, 2018) prepared NiS anchored carbon nanofibers by electrospinning combined with calcination and in situ sulfurization with the specific area of $376 \text{ m}^2 \text{ g}^{-1}$.

2.3.5 Application of CNF

Due to their unique properties, carbon nanofibers can be good candidates in many applications. Some applications include heat treatment material, catalyst (Al-Enizi *et al.*, 2018; Chung *et al.*, 2018), composite reinforcement and supporting materials for metal nanoparticles (Bajaj *et al.*, 2018), membrane-based separation (Y. Bai *et al.*, 2018), and sensors including biosensors (Alim *et al.*, 2018) and screen-printed electrochemical sensor (Yao Yao *et al.*, 2019). Moreover, they are also used as electrode materials for energy storage devices. For example, the energy storage devices include Li-ion batteries (Jiandong Liu 2018), Li-S battery (Cao *et al.*, 2018), sodium-ion batteries (G. Chen *et al.*, 2018), sodium-selenium batteries (Hui Wang *et al.*, 2019), sodium-sulfur batteries (Xia *et al.*, 2018), flexible lithium ion batteries (F. Zhao *et al.*, 2017), lead acid batteries (Blecua *et al.*, 2017), vanadium flow batteries (Xu *et al.*, 2017), fuel cells (Abdelkareem *et al.*, 2019), Zn-air cells (J. E. Park *et al.*, 2018), Li-air battery (Song and Shin, 2014), dye-sanitized solar cells (Ling Li *et al.*, 2018),

supercapacitors (Agyemang *et al.*, 2018), symmetric supercapacitors (N. Cai *et al.*, 2018), asymmetric supercapacitors (Budhiraju *et al.*, 2017), flexible supercapacitors (Y. Li *et al.*, 2018), and all-solid-state flexible supercapacitors (Tian *et al.*, 2017). In this section, the review concentrates mainly on the literature of CNFs used as the electrode material for electrochemical capacitor or supercapacitor.

2.4 MnO_x

Manganese oxides have been considered as promise materials for energy storage devices to replace the high capacitive RuO₂ because of their inexpensive cost, environmental safety, and high specific capacitance (Ahuja *et al.*, 2018). MnO_x has characteristic of pseudocapacitive materials, which stores energy by reversibly redox reaction including exchanging electric charge with electrolyte and changing the oxidation states (Barai *et al.*, 2017). The crystallinity of MnO_x affects very much on the surface area and the conductivity, i.e. the more crystallinity, the higher conductivity, but the lower surface area. The preparation conditions affect the morphology, composition and structure to form different types of MnO₂ including α -MnO₂ (Sankar *et al.*, 2018), β -MnO_x (R.-B. Li *et al.*, 2018), γ -MnO_x (Ranganatha and Munichandraiah, 2018), λ -MnO₂ (Tang *et al.*, 2018), and δ -MnO₂ (Q. Gao *et al.*, 2018). Moreover, the preparation conditions also cause the different morphologies including nanoparticles (Aswathy *et al.*, 2018), nanospheres (Chai *et al.*, 2018), nanoneedles (Davoglio *et al.*, 2018) nanowires (Byles *et al.*, 2018), nanosheets (Amir *et al.*, 2018), nanorods (Ahn *et al.*, 2018), nanoribbon (Ahuja *et al.*, 2018) etc. Various techniques have been used to synthesize manganese oxides including hydrothermal, sol-gel, reduction reaction, co-precipitation, and cathodic and anodic deposition (Y.

Chen *et al.*, 2013). There are many literatures reported the manganese oxides with the applications in energy storage devices. Bai (X. Bai *et al.*, 2018) synthesized hierarchical multidimensional MnO₂ by hydrothermal method with the specific capacitance of 311.52 F g⁻¹ at the current density of 0.3 A g⁻¹ in 1 M Na₂SO₄. Aswathy (Aswathy *et al.*, 2018) prepared Mn₃O₄ nanoparticles on the surface of activated graphited paper by template-free hydrothermal method with the specific capacitance of 471 F g⁻¹ at the current density of 1 mA cm⁻² in 1 M Na₂SO₄. Bi (Bi *et al.*, 2018) fabricated NiO/MnO₂ composite by one-pot microwave method with the specific capacitance of 102.78 mA h g⁻¹ at the current density of 1 A g⁻¹ in 6 M KOH. Chai (Chai *et al.*, 2018) synthesized the hollow δ-MnO₂ by in situ redox etching reaction using MoS₂ nanospheres as a template with the specific capacitance of 394 F g⁻¹ at the current density of 1 A g⁻¹ in 1 M Na₂SO₄. Cheng (Y. Cheng *et al.*, 2018) synthesized Mn₃O₄ by mediation of fatty acids with the specific capacitance of 304 F g⁻¹ at the scan rate of 10 mVs⁻¹ in 1 M Na₂SO₄. Chi (Chi *et al.*, 2018) prepared manganese oxide/graphene hydrogel composite by electrodepositing with the specific capacitance of 352.9 F g⁻¹ at the current density of 1 A g⁻¹ in 1 M Na₂SO₄. Davoglio (Davoglio *et al.*, 2018) fabricated α-MnO₂ nanoneedles by microwave-assisted method with the specific capacitance of 289 F g⁻¹ at the current density of 0.5 A g⁻¹ in 1 M Na₂SO₄. Ensafi (Ensafi *et al.*, 2018) prepared graphene/polyaniline-benzimidazole/graphene/MnO₂ quaternary composite by polymerization and hydrothermal method with the specific capacitance of 675 F g⁻¹ at the current density of 50 A g⁻¹ in 0.5 M H₂SO₄. Gao (Q. Gao *et al.*, 2018) synthesized Fe doped δ-MnO₂ nanoneedles by hydrothermal method with the specific capacitance of 627.3 F g⁻¹ at the current density of 1 A g⁻¹ in 3 M KOH. Ghasemi (Ghasemi *et al.*, 2018) synthesized MnO₂/RGO nanohybrid sonochemical method and

electrostatic co-precipitation procedure with the specific capacitance of 375 F g^{-1} at the current density of 1 A g^{-1} in $0.5 \text{ M Na}_2\text{SO}_4$. Raj (Gnana Sundara Raj *et al.*, 2018) prepared Mn_2SnO_4 by simple one-pot sonochemical method with the specific capacitance of 144 F g^{-1} at the current density of 3 mA cm^{-1} in $1 \text{ M Na}_2\text{SO}_4$. Jia (Jia *et al.*, 2018) fabricated porous carbon/ MnO_2 nanowires by hydrothermal method with the specific capacitance of 338 F g^{-1} at the current density of 1 A g^{-1} in $1 \text{ M Na}_2\text{SO}_4$. Kadam (Kadam *et al.*, 2018) synthesized flower like Mn-Co mixed metal oxide by electrodeposition method with the specific capacitance of 679 F g^{-1} at the scan rate 5 mV s^{-1} in 1 M NaOH . Al-Hemaid (Kogularasu *et al.*, 2018) prepared MnFe_2O_4 nano-agglomerates by template-synthesis approach with the specific capacitance of 1283 F g^{-1} at the scan rate of 5 mV s^{-1} in 1 M KOH . Lei (Lei *et al.*, 2018) fabricated Mn-doped nitrogen-containing carbon by leather processing with the specific capacitance of 272.62 F g^{-1} at the current density of 1 A g^{-1} in 1 M KOH . Li (R.-B. Li *et al.*, 2018) synthesized hierarchical mesoporous beta-manganese dioxide nanoflower by self-assembly method with the specific capacitance of 500 F g^{-1} at the current density of 1 A g^{-1} in $0.5 \text{ M Na}_2\text{SO}_4$.

2.5 Carbon composite nanofibers

2.5.1 Structure of carbon composite nanofibers

Carbon composite nanofibers (CCNF) is carbon nanofibers containing different phase fillers. The structure of CCNF is decided by the shape of CNF matrix. The diameter of the composite nanofibers is about hundreds of nanometer and their lengths can reach several micrometers (L. Chen *et al.*, 2018).

2.5.2 The synthesis methods

As reported earlier that the objective of carbon composite nanofibers is to improve its properties and favored over the cheaper price. To date, the synthesis methods of CCNF have been the subject of intense investigation, especially for an application of electrode material for energy storage devices. It is well known that, the materials for electrochemical capacitor electrode are divided into three main types: carbon based (CNT, CNF, Graphene, etc.), transition metal oxide/hydroxide (RuO₂, MnO₂, Ni(OH)₂, etc.) and conducting polymers (polyaniline (PANI), polypyrrole (PPy), etc. (Budhiraju *et al.*, 2017). The composite of these materials with CNF have been intensively investigated. The general preparation approaches of CNF matrix are chemical vapor deposition growth and electrospinning as described in section 2.6.2. Various methods for preparing the metal oxide/hydroxide nanoparticles, which acted as the composite materials are similar in section 2.4. The performance of composite fibers is strongly governed by dispersion of nanoparticles in the CNF matrix. Thus, the dispersion is a key role in the synthesis of CCNF. It was found that CNF with large surface area can act as a support for dispersion of metal oxide/hydroxide nanoparticles, and thus improving the conductivity of electrode material. Moreover, surface treatment is a method to help the dispersion of metal oxide/hydroxide in CNF matrix (Sinprachim *et al.*, 2016).

2.5.3 Applications of carbon composite nanofibers in supercapacitors

Generally, carbon-based composite material are able to be used in various fields of applications as reported in section 2.3.5. Based on their advantages including different allotropes, various dimensionality, different forms, good conductivity, high surface area, low cost, environmental safety, operation in wide range of temperature,

abundant element, CNF still have low energy density. Therefore, CNF have been used as the based materials to composite with the pseudocapacitive materials, such as metal oxides/hydroxides and conducting polymers in order to obtain the maximum potentials. The synthesis methods, testing condition and specific capacitances of carbon-based composite nanofibers in the applications of supercapacitors were summarized in Table 2.1.

Table 2.1 The synthesis methods, testing condition and specific capacitances of carbon-based composite nanofibers. (Continued)

Materials	Synthesis method	Testing conditions	Specific capacitance	Reference
CNF-CNT-PANI	Electrospinning and carbonization	1 A g ⁻¹ , 1 M H ₂ SO ₄ , (0-1.0 V)	1119 F g ⁻¹	(Agyemang <i>et al.</i> , 2018)
CNF	Electrospinning and carbonization	1 mV s ⁻¹ , 3M LiOH, (-1 – 0 V)	277 F g ⁻¹	(Bhoyate <i>et al.</i> , 2018)
NiMoO ₄ /Hollow CNF	electrospinning	1 A g ⁻¹ , 6 M KOH (0 – 0.5 V)	1438 F g ⁻¹	(Budhiraju <i>et al.</i> , 2017)
Inter-bonded CNF	Pyrolysis technique	1 A g ⁻¹ , 6 M KOH, (-0.9 – 0.1 V)	241 F g ⁻¹	(J. Cai <i>et al.</i> , 2016)
RGO-AgNP/N-CNF	Modified Hummers, Electrospinning and carbonization	0.5 A g ⁻¹	188 F g ⁻¹	(N. Cai <i>et al.</i> , 2018)

Table 2.1 The synthesis methods, testing condition and specific capacitances of carbon-based composite nanofibers. (Continued)

Materials	Synthesis method	Testing conditions	Specific capacitance	Reference
PANI-CNT- CNF	Plasmas modification, electrospinning and carbonization	1 A g ⁻¹ , (0 – 1 V) and 1 M H ₂ SO ₄ ,	304 F g ⁻¹	(W.-M. Chang <i>et al.</i> , 2016)
Ultrathin CNF	Centrifuged electrospinning and carbonization	1 A g ⁻¹ , 1 M H ₂ SO ₄ , (-1 – 1 V)	243 F g ⁻¹	(W.-M. Chang <i>et al.</i> , 2018)
GO-CNF	UV-induced photo polymerization, electrospinning and thermal treatment	1 A g ⁻¹ , 6 M KOH, (0 – 1 V)	140.1 F g ⁻¹	(Chee <i>et al.</i> , 2017)
CNF-PPy- rGO	Electrospinning, carbonization, electrochemical deposition	2 mV s ⁻¹ , 3 M KCL, (-0.2 – 0.8 V)	336.2 F g ⁻¹	(L. Chen <i>et al.</i> , 2018)
Cross-liked CNF	Electrospinning, carbonization,	1 A g ⁻¹ , 6 M KOH, (-0.8 – 0 V)	222.9 F g ⁻¹	(Jianping Ding <i>et al.</i> , 2018)

Table 2.1 The synthesis methods, testing condition and specific capacitances of carbon-based composite nanofibers. (Continued)

Materials	Synthesis method	Testing conditions	Specific capacitance	Reference
CNF/G	Electrospinning, spraying, heat treatment	1 A g ⁻¹ , 6 M KOH, (-0.9 – 0.1 V)	180 F g ⁻¹	(Q. Dong <i>et al.</i> , 2013)
mesoporous CNF		0.7 A g ⁻¹ , (0.1 – 0.8 V)	303 F g ⁻¹	(Y. Dong <i>et al.</i> , 2015)
CNF/CuFe ₂ O ₄	Electrospinning and carbonization	10 mV s ⁻¹ , 1 M KOH, (0 – 0.35 V)	191 F g ⁻¹	(Nilmoung <i>et al.</i> , 2016)
AgO _x -MnO _x /CNF	Electrospinning and carbonization	0.5 A g ⁻¹ , 6 M KOH, (-1 – 0 V)	204 F g ⁻¹	(Sinprachim <i>et al.</i> , 2016)
Porous CNF	Electrospinning and corrosion	1 A g ⁻¹ , 1 mol L ⁻¹ H ₂ SO ₄ , (0 – 1 V)	272 F g ⁻¹	(Y. Li <i>et al.</i> , 2018)
H-CeO ₂ @GC	hydrothermal	1 A g ⁻¹ , 6 M KOH (0 – 0.55 V)	501 F g ⁻¹	(W. Wu <i>et al.</i> , 2019)

Table 2.1 The synthesis methods, testing condition and specific capacitances of carbon-based composite nanofibers. (Continued)

Materials	Synthesis method	Testing conditions	Specific capacitance	Reference
Carbon membrane	Liquid-liquid phase separation and solvent evaporation	0.5 A g ⁻¹ , 6 mol L ⁻¹ KOH, (-1 – 0 V)	247 F g ⁻¹	(Y. Wu <i>et al.</i> , 2019)
Inner PCNF	Electrospinning, oxidative polymerization	1 A g ⁻¹ , 6 M KOH, (-1 – 0 V)	328 F g ⁻¹	(Xie <i>et al.</i> , 2017)
OMCN@NiCo ₂ O ₂	Assembly, solvothermal	1 A g ⁻¹ , 6 M KOH, (0 – 0.6 V)	1631 F g ⁻¹	(Y. Yang <i>et al.</i> , 2019)

CHAPTER III

EXPERIMENTAL PROCEDURE

Chapter III describes the experimental method of the research, which can be generally categorized into the following three main sections:

- (1) Sample preparation techniques: synthesis of CNF, P-CNF, IC-CNF, and C/MnO_x by a single-nozzle and core-shell-nozzle electrospinning technique followed by carbonization and CO₂-activation process.
- (2) Material characterizations: X-ray diffraction (XRD), scanning electron microscopy (SEM), field emission scanning electron microscopy (FE-SEM), transmission electron microscopy (TEM), Raman, and gas absorption technique.
- (3) Electrochemical measurements: Cyclic voltammetry (CV), Galvanostatic charge-discharge (GCD) and electrochemical impedance spectroscopy (EIS).

This chapter will give a brief introduction of these techniques, facilities, and the background theories.

3.1 Fabrication of CNF, P-CNF, IC-CNF, and C-MnO_x

3.1.1 The precursor preparation

In this study, polyacrylonitrile (PAN), polyvinylpyrrolidone (PVP), N, N-dimethylformamide (DMF), paraffin oil, and manganese nitrate [Mn(NO₃)₂] were used as the starting materials. PAN was the main material to form carbon, PVP was the agent to form fiber-fiber interconnection, paraffin oil was the agent to produce porosity in the fiber, and manganese nitrate was the main source for manganese oxide nanoparticles.

For CNF, the precursor solution was prepared by dissolving PAN with the weight percentage of 10 wt% in DMF. For P-CNF, the precursor solution, which has been used as the shell solution, was prepared by dissolving PAN with the weight percentage of 8 wt% in DMF and paraffin oil was used as the core solution.

For IC-CNF, two different methods were used including core-shell and blend-solution electrospinning. For core-shell electrospinning, PAN or PVP was dissolved in DMF with the weight percentage of 10 wt% of PAN or PVP compared with DMF. For PAN/PVP blend electrospinning, the solutions were prepared by dissolving 10 wt% of both PAN and PVP in DMF in different mass ratios. Three different precursors could be obtained by the mass ratios of PVP and PAN were 1:9, 2:8, and 3:7.

For C/MnO_x, the PAN and PAN mixed with metal source were dissolved in DMF separately by 20 wt% of metal source was compared to PAN content and the total content (metal and PAN) was 10 wt% compare to DMF. The PAN solution was used as a core solution while the PAN mixed with metal source was used as a shell solution to ensure that the particles could stay on the outmost surface maximally. The weight percentage of the metal-PAN shell solution was varied in three conditions including 10

wt%, 9 wt%, and 8 wt% while the weight percentage of PAN-core solution was maintained constantly of 10 wt%. After being strongly stirred at room temperature for 2h, the solutions were followed by ultrasonication for 1h at room temperature and subsequently continued stirring until the solutions became homogeneous, which were ready for doing electrospinning process. The materials used in this research are shown in Table 3.1.

Table 3.1 List of materials used as starting materials for CNF, P-CNF, IC-CNF, and C/MnO_x preparation, quoting their source and purity.

Materials	Sources	Purity/MW
Polyacrylonitrile	Sigma-Aldrich	150, 000
polyvinylpyrrolidone	Sigma-Aldrich	1,300,000
N, N-dimethylformamide	SIAL	99.8%
Paraffin oil	Sigma-Aldrich	99.9%
Manganese (II) nitrate	PRS Panreac	251.01

3.1.2 Fabrication of the as-spun nanofibers

The homogeneous precursor solutions were loaded into the 10-ml-plastic syringes and inserted into the homemade electrospinning/core-shell electrospinning system (see Figure 3.2). Therefore, we obtained different as-spun mats, which were

PAN, PAN-paraffin oil, PVP-PAN_1-9, PVP-PAN_2-8, PVP-PAN_3-7, core-shell PVP-PAN, core-shell PAN-PVP, PAN-PAN_Mn(NO₃)₂_10-10, PAN-PAN_Mn(NO₃)₂_10-9, and PAN-PAN_Mn(NO₃)₂_10-8. The feeding rate of the pump was in the range of 0.5-0.6 ml h⁻¹, and the applied voltage was set between 5 and 7 kV. The distance between the spinnerets and the rotating drum collector was 10 cm. The as-spun nanofibers were collected from the grounded collector and kept in an incubator at 60°C for overnight before doing further calcinations.

3.1.3 Calcination of the electrospun nanofibers

Three main steps were applied in the calcination process including stabilization, carbonization, and activation (Nilmoung *et al.*, 2016). The as-spun samples were stabilized in the temperature of 230°C by the furnace (MTI GSL-1100X, USA) for 2h under the air atmosphere to form infusible ladder polymer, which preventing the fibers from melting at the carbonization process (Y. Choi *et al.*, 2014). Then, the argon (400 ml min⁻¹) was used instead of air in the tube and the temperature was increased up to 900°C with the heating rate 5°C min⁻¹ and hold for 2h. The inner gas (argon in this case) was used to guarantee that there was no oxygen molecule, which could burn the fiber at high temperature. Finally, the activation process by the flow of CO₂ was performed directly at the last 20 min of the last step and the furnace tube was cooled down naturally with argon atmosphere. The CO₂-activation could increase the surface area of the sample by more pores were created by the interaction between CO₂ and carbon surface (Y.-C. Chang *et al.*, 2017). The calcined samples were obtained as paper sheets and divided into three groups. The first group consisted of activated carbon nanofibers derived from pure PAN, porous activated carbon nanofibers derived from PAN-paraffin oil. The second group consisted of activated carbon nanofibers derived from PVP-PAN

blend with different ratio, i.e. PVP-PAN_1-9, PVP-PAN_2-8, and PVP-PAN_3-7. The second group also consisted of activated carbon nanofibers derived from core-shell PVP-PAN, which PVP solution was used as a core and PAN solution was used as a shell solution, core-shell PAN-PVP, which PAN solution was used as a core and PVP was used as a shell solution. The last group consisted of three samples. The first sample is activated carbon/manganese oxide composite nanofibers derived from PAN/PAN-Mn(NO₃)₂_10-10, which 10 wt% of PAN was used as a core solution and 10 wt% of PAN-Mn(NO₃)₂ was used as a shell solution. The second sample was activated carbon/manganese oxide composite nanofibers derived from PAN/PAN-Mn(NO₃)₂_10-9, which 10 wt% of PAN was used as a core solution and 9 wt% of PAN-Mn(NO₃)₂ was used as a shell solution. The last sample was activated carbon/manganese oxide composite nanofibers derived from PAN/PAN-Mn(NO₃)₂_10-8, which 10 wt% of PAN was used as a core solution and 8 wt% of PAN-Mn(NO₃)₂ was used as a shell solution. All samples were renamed as CNF, P-CNF, C_1-9, C_2-8, C_3-7, CS-PVP, CS-PAN, C-Mn_10-10, C-Mn_10-9, C-Mn_1-8, respectively, which were ready for doing characterizations. Figure 3.1 displayed the whole procedure of fabrication of all samples including solution preparation, electrospinning, calcination and activation. The flowchart diagram showing the overview of the experimental procedure performed in this work was illustrated in Figure 3.3.

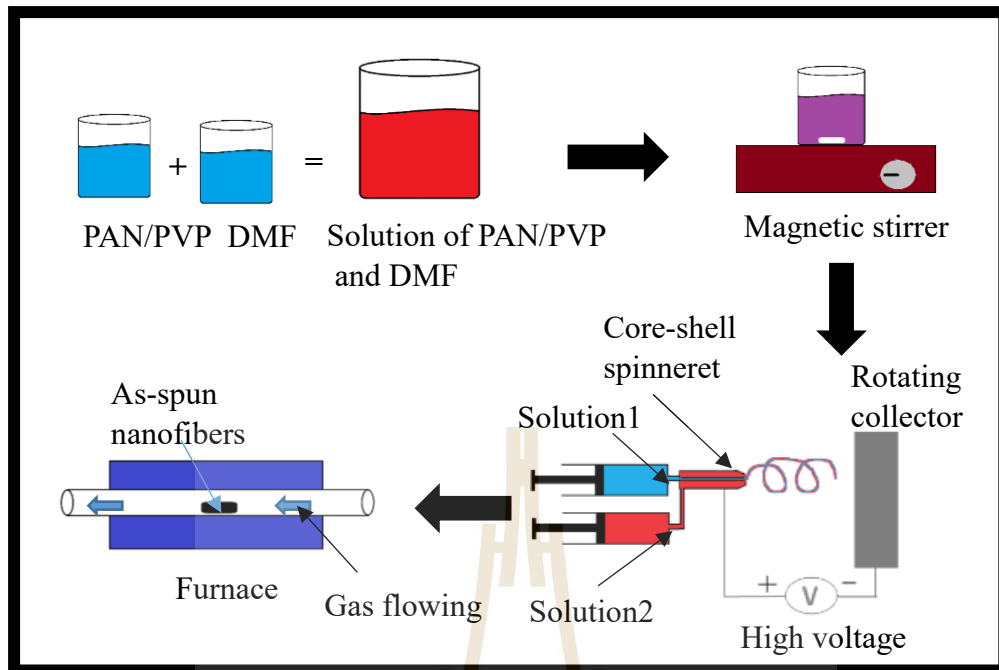


Figure 3.1 Procedure of preparation of all samples.



Figure 3.2 The homemade single/core-shell electrospinning machine.

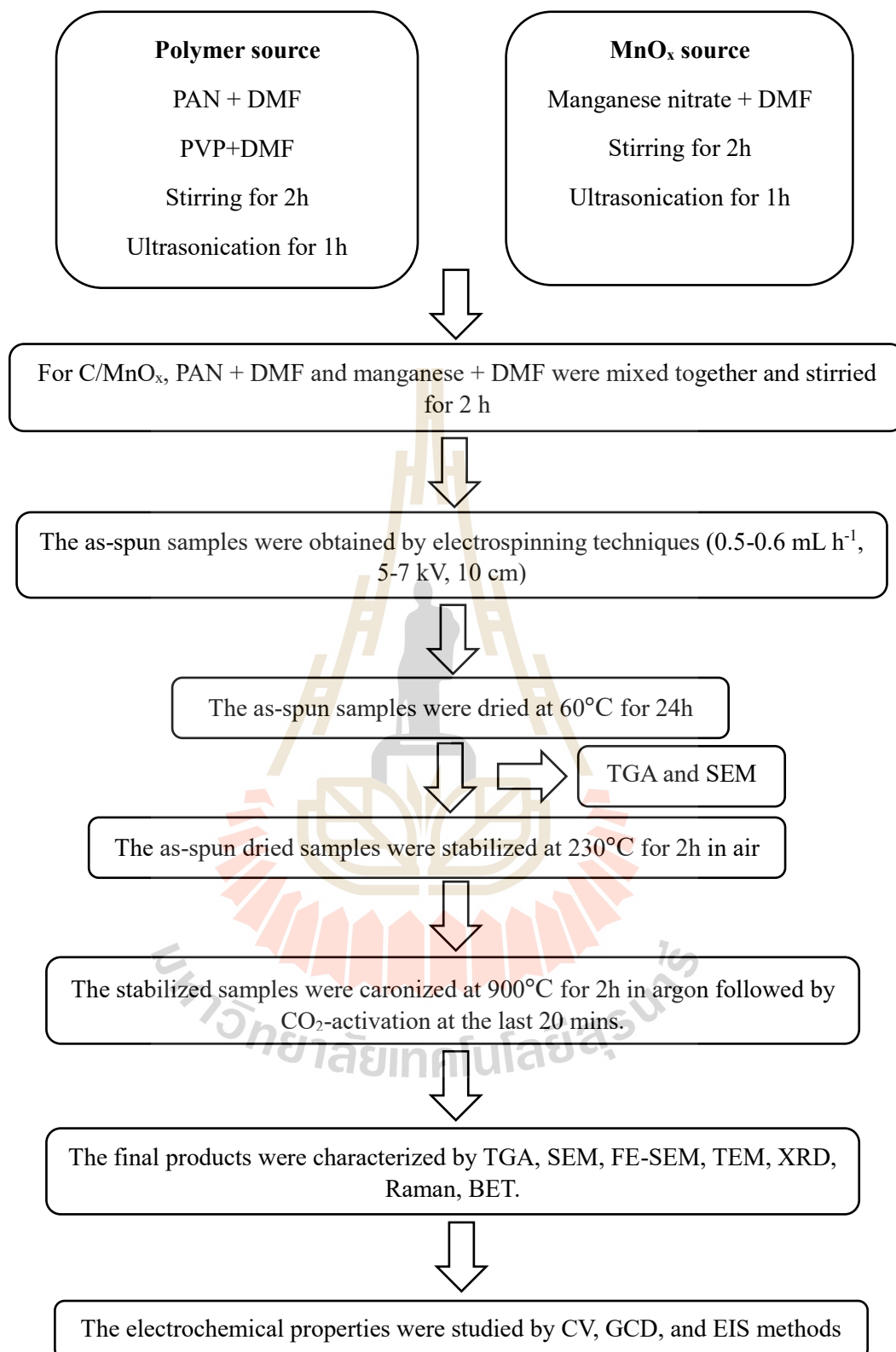


Figure 3.3 The flowchart displaying the fabrication and characterization of all samples.

3.2 Material characterization

In this research, the phase composition and microstructure of all samples were characterized by XRD, SEM and TEM techniques. The quality of carbon material was studied by Raman technique. The surface area and pore size distribution of the nanoparticles was investigated by Gas absorption techniques. The electrochemical properties were studied on a potentiostat galvanostat (PGSTAT302N) via CV, GCD and EIS techniques. The several characterization techniques were used and brief concepts were given as follows:

3.2.1 Thermogravimetric analyzer (TGA)

Thermogravimetric analyzer (TGA) is a powerful technique used to study the decomposition temperatures and the thermal stability of materials by measuring the weight loss while the temperature increases (Al Garawi *et al.*, 2017). The measurement usually takes place in the inert gas atmosphere, such as nitrogen or argon to prevent the sample from the oxidation. Generally, DTA or DSC (Differential Thermal Analysis or Differential Scanning Calorimetry) are performed simultaneously with TGA (Korhammer *et al.*, 2018). There are some factors influenced the result of the experiment like time step, nucleation rate, sample mass, water vapor pressure, and heating rate (Lan *et al.*, 2018).

In this study, the weight loss versus the temperature of PAN and PAN composite were measured by TGA techniques. Moreover, this technique also provides the temperatures for doing stabilization and carbonization. The experiment was carried out in nitrogen atmosphere from room temperature up to 1000°C with the mass of each sample about 3 mg and heating rate of 10°C/min using TGA-DSC (METTLER TOLEDO STARe).

3.2.2 Scanning electron microscopy (SEM)

Scanning electron microscopy (SEM) is the powerful technique used to observe the morphologies of the samples by using the electron beams with the applications in Biology and Materials Science (Hayakawa and Matsuoka, 2016). The signals obtained from the secondary electrons, backscattered electrons, and characteristic X-ray generate the images of the sample, where they meet the primary electron beams. Normally, the secondary electrons are the major signals to create the images of the sample. The samples used in the study have to be a conductive materials, otherwise a gold-coating process is performed on the sample before the experiment to improve the conductivity of the samples (Liv *et al.*, 2014). There are of many kinds of SEM, which their specialties focus on different manners. They include Environmental SEM, High-Resolution SEM, Hellion Ion Microscopy (HIM), and Cryo-SEM. In the environmental SEM (also known as Low-vacuum SEM), the microscope column and the sample chamber should stay under a low vacuum to prevent scattering between the electron beams and gas molecules. Usually in SEM, the minimal area of the electron beams can determine the resolution of the image. However, this area is getting bigger by the interaction volume resulting from the electron beam scattering. Therefore, to improve the resolution, Hellion ion is used to replace electron, which the ion emission created by selecting only one ion for imaging among the three. The gas field ionization source contain an ultra-high brightness, so a very small beam is needed to determined aperture and it can go deeper into the specimen (de Souza and Attias, 2018). Figure 3.4 illustrates the schematic representation of SEM of a sample and the scattering of primary electron by the sample. In this work, the scanning electron microscopy (FE-SEM INCAx-act 51-ADD0088, SUT) was used (see Figure 3.5).

3.2.3 Transmission electron microscopy (TEM)

Transmission electron microscopy (TEM) is a powerful tool used to study the morphologies and defect characterization in the sample. Similar to process of the slide projector, electron beam to go through the slide and some electrons can pass through and inject on the screen to produce the image. In TEM technique, electron beam is produced and focused on a very thin sample and go through it. The detector catch the passed-through electron beam and generate the image (Callahan *et al.*, 2018). There are several ways to obtain the images using a fluorescent screen, photographic film, or CCD camera. Since the electron have to go through the sample, the sample preparation is the key step in this technique. The diffraction contrast technique can also be performed in TEM to study the crystal defects including dislocation lines (Hasanzadeh *et al.*, 2018). Normally the sample-for-TEM preparation is prepared by dispersing the sample in ethanol. The solution is dropped on a copper grid and dried for several hours before doing characterization.

Generally, the main components of TEM are electron beam source, lenses, sample holder, and electron detector. Bases on the sample characteristic, different types of TEM have been designed for specific purpose. Some samples require high energy to obtain high resolution image, however, other samples cannot work with the high energy which could destroy the sample. So the special TEM, which operate at the low energy have been developed (Geelen *et al.*, 2015). Figure 3.6 shows the schematic outline of TEM.

In this work, all prepared samples were measured with the energy of 200 keV by using FEI-TEM- TECNAI G220, SUT, as displayed in Figure 3.7. The Bright field

TEM images, high-resolution (HRTEM) TEM images and corresponding selected areas of electron diffraction (SAED) patterns of the samples were also recorded in this work.

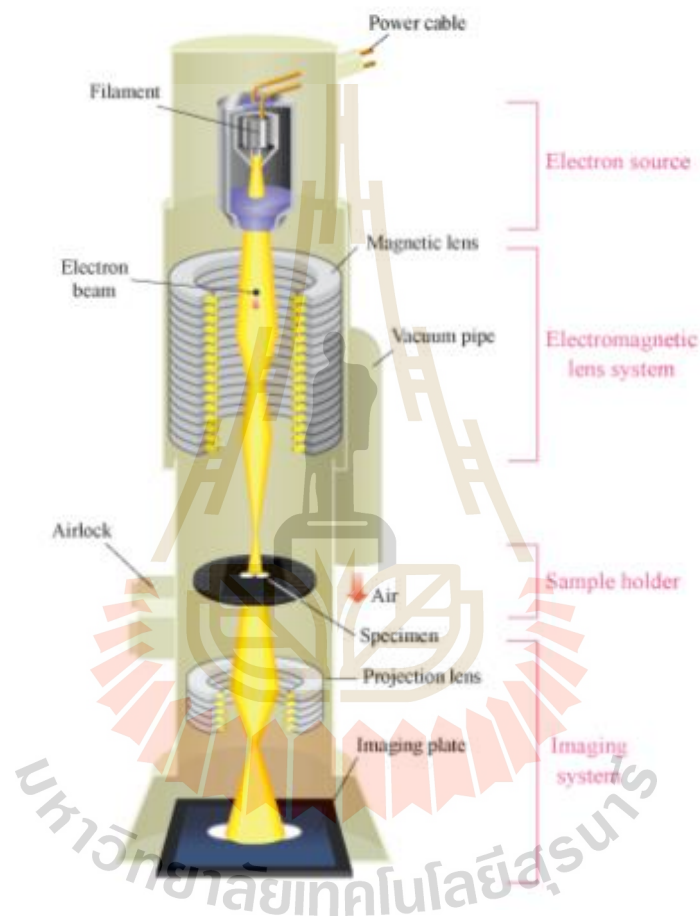


Figure 3.6 The schematic outline of TEM (adapted from Atomic World (http://www.hkphy.org/atomic_world/tem/tem02_e.html)).



Figure 3.7 Transmission Electron Microscopes (FEI TEM- TECNAI G220, SUT).

3.2.4 X-ray diffraction (XRD)

X-ray diffraction (XRD) is a powerful technique used to determine the crystalline materials, to define the structures and orientations of single crystals or grains, to determine the average spacing between layers or rows of atom, and to confirm the sample purity and texture. Basically, the XRD components comprise of X-ray source, sample holder, and signal detector. The X-ray arm and the detector arm can rotate around the sample to shine and detect X-ray from different angle for obtaining the spectrum of angles, intensity, and peak width, which are the main data to analyze

the sample. The phases of the unknown compound in the sample are determined by comparing the spectra obtained from the experiment and the reference data (Dejoie *et al.*, 2018). For more details, the structures getting from the data of experiment are predicted by four steps: (i) preconditioning including background subtraction and optimization of profile parameters, (ii) generation of trial structures (iii) simulation of the XRD pattern for a given trial structure, and (iv) fitting the experiment structure with the simulation structure (Gao *et al.*, 2017). The X-ray principle is summarized as following. The X-ray beam incident on a crystalline solid will be diffracted by the crystallographic planes as illustrated in Figure 3.7. The constructive and destructive interferences occur if a phase difference is $n\lambda$ (in phase) and $n\lambda/2$ (out of phase). Two in-phase incident waves, beam 1 and beam 2, are deflected by two crystal planes (A and B). The deflected waves will not be in phase except when the following relationship (Bragg equation) is satisfied.

$$2d\sin\theta = n\lambda \quad (3.1)$$

Where d is the spacing between the parallel crystal planes, θ is the angle of incident beam, λ is the wavelength of the incident X-ray beam and n is an integer. In order to keep these beams in phase, their path difference ($SQ + QT = 2d \sin \theta$) has to equal one or multiple X-ray wavelengths ($n\lambda$). The diffractometer records changes of diffraction intensity with 2θ . A number of intensity peaks located at different 2θ provide a 'fingerprint' for a crystalline solid. Identification of crystalline substance and crystalline phases in a specimen is achieved by comparing the specimen diffraction spectrum with spectra of known crystalline substances.

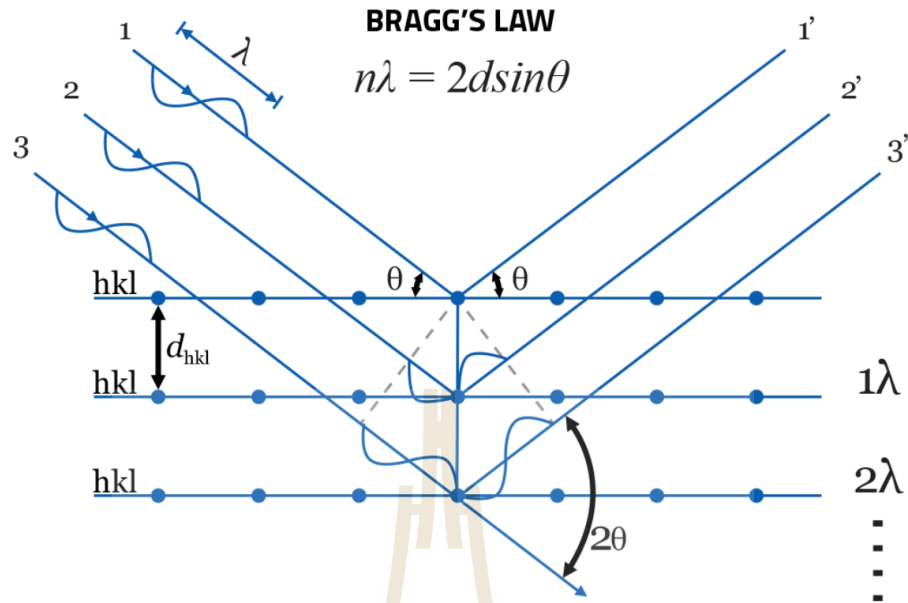


Figure 3.8 Bragg's law (adapted from VEQTER (<http://www.veqter.co.uk/residual-stress-measurement/x-ray-diffraction>)).

In this study, the phases and structure analysis of the samples were determined by X-ray diffraction (XRD; D2 Advance Bruker) with Cu K_{α} at $\lambda = 0.15406$ nm as shown in Figure 3.8. The XRD pattern were recorded in the 2θ of 15° - 80° with the time step of 0.5 and the step size of 0.02. The crystalline phase identification was carried out by comparison with the Joint Committee on Powder Diffraction Standards (JCPDS) diffraction files. The crystallite size of the nanocrystalline samples was measured from the line broadening analysis of the diffraction peak by using the Debye-Scherer equation:

$$D = \frac{k\lambda}{\beta \cos\theta} \quad (3.2)$$

where D is the crystallite size (nm), k is the spherical shape factor (0.9), λ is the X-ray wavelength, θ is the diffraction angle, and β is the full width at half maximum (FWHM) intensity.



Figure 3.9 X-ray diffractometer (XRD; Bruker D2, Germany, SUT).

3.2.5 Gas adsorption techniques

The gas adsorption technique is a powerful tool to measure the specific surface area and the pore characteristics of the samples by measuring the amount of N_2 , which was adsorbed by the samples with the respect to the relative pressure. The measurement is performed at the very low temperature in nitrogen liquid at 77K. Normally, the sample was degassed at certain temperature to remove the moisture on the sample before doing measurement (Lapham and Lapham, 2017). The adsorption/desorption isotherm is obtained by measuring the pressure and applying the gas law. The

adsorption/desorption isotherm provides information about the pore characteristic of the sample including the surface area, pore volume, and pore size.

The adsorption/desorption isotherm can have different shape depending on the adsorbent, adsorbate and the adsorbent adsorbate interaction. According to the International Union of Pure and Applied Chemistry (IUPAC) classification, the adsorption/desorption isotherm is divided into six types.

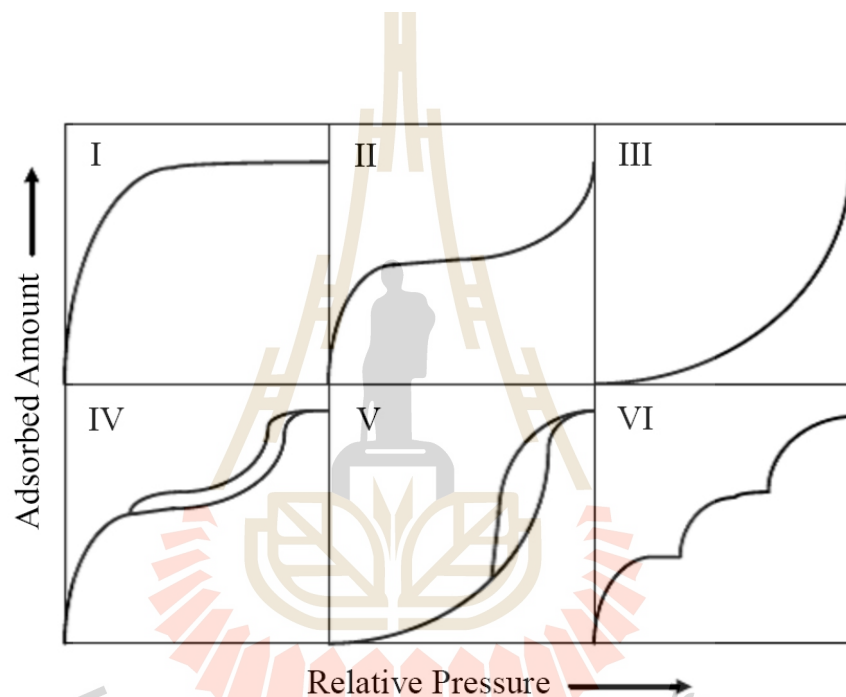


Figure 3.10 The IUPAC classification of adsorption isotherms (Sangwichien, 2002).

There are three types of pore based on the size including micropores (pore size < 2 nm), mesopores (pore size between 2 to 50 nm), and macropores (pore size > 50 nm). As presented in figure 3.9, type I represents the typical isotherm of micro-porous adsorbent. Type II and III represent the adsorption isotherm on macroporous and non-porous adsorbents. Type IV and V represent the mesoporous adsorbents. Type VI occurs for some materials with relatively strong forces, usually when the temperature

is near the melting point for the adsorbed gas (P. B. Balbuena, and Gubbins, K. E. , 1993; Sangwichien, 2002).

The Brunauer Emmett Teller (BET) technique is used mainly to observe the specific surface area of materials by analyzing the absorption isotherm of nitrogen gas compared to a reference cell (Brunauer *et al.*, 1938). For BET method, the phenomenon of adsorption can be expressed with the following equation.

$$\frac{1}{W\left[\left(\frac{P_0}{P}\right)-1\right]} = \frac{1}{W_m C} + \frac{C-1}{W_m C} \left(\frac{P}{P_0}\right) \quad (3.5)$$

where W is the total volume of adsorbed gas. W_m is the volume of adsorbed gas in a unimolecular layer covering the surface. P_A is saturation pressure. P is pressure. C is dimensionless constant that approximately equal

$$C = \exp(E_1 - E_L) / RT \quad (3.6)$$

Here E_1 is the heat of adsorption of the gas on the surface for first monolayer and E_L is the heat of liquefaction of the gas. By decreasing in relative pressure, desorption nitrogen was observed. The specific surface area can be calculated by

$$a_{BET} = \frac{W_m \sigma N_A}{m V_0} \quad (3.7)$$

where W_m arises from the slop and the intercept of plot between the relative pressure and $1/W[(P/P_0) - 1]$, σ is the area of the surface occupied by individual gas molecules, N_A is the Avogadro number, m is the sample mass and V_0 is the molar volume of gas (Pajarre and Koukkari, 2018).

The Barrett-Joyner-Halenda (BJH) method is a procedure for calculating pore size distributions, especially for mesopore and smaller macropore, from experimental isotherms using the Kelvin model of pore filling (Barrett *et al.*, 1951). For the adsorption/desorption isotherm depending on the shape of mesopore, the Kelvin equation represents the relationship between mesopore size and critical condensation pressure. The Kelvin equation is used to calculate pore size distribution from desorption isotherm (K. Liu *et al.*, 2018). Core radius (r) can be calculated by the Kelvin equation as follows:

$$\ln \frac{P}{P_0} = - \frac{2\gamma V_L}{RT r} \quad (3.8)$$

where γ is surface tension, V_L is molar volume of liquid adsorptive, R is gas constant and T is absolute temperature. If γ and V_L of nitrogen at liquid nitrogen temperature (77 K) are applied, the following equation can be obtained.

$$r = 0.953 / \ln (P_0 / P) \quad (3.9)$$

In this work, the specific surface area (S_p) and porosity of the nanoparticles were measured by using the N_2 adsorption technique. By using computer interfaced BELSORP-mini-II instruments as revealed in Figure 3.10, all samples were thoroughly degassed at 150°C for 6 h. The specific surface area was calculated by using the BET method. The pore size distributions were obtained from the analysis of the adsorption branch of the isotherm by the BJH method.



Figure 3.11 The photo of BET, BEL SORP MINI II JAPAN.

3.2.6 Raman spectroscopy

Raman spectroscopy is a powerful technique used to characterize the structural fingerprints of carbeneous materials based on the inelastic scattering of monochromatic light from a laser beam (Bokobza *et al.*, 2014). It is the nondestructive technique the samples can be reused by other experiments. By measuring the shift of frequency of the laser comparing to the original frequency, which is reemitted after absorbing, we can plot the spectrum providing the information about the materials. Every band in the Raman spectrum corresponds to a specific vibrational frequency of a bond within the

molecule. For example, for carboneous materials, the Raman shifts occur at two different wavelength bands namely the graphitic Band (G band) occurring at ~ 1600 cm^{-1} and the disordered band (D band) occurring at ~ 1350 cm^{-1} (Brolly *et al.*, 2016).

In this work the Raman spectrum were recorded at the room temperature by BRUKER RAM II VERTEX 70, $\lambda=532$ nm. The sprectra were obtained over the range of $500\text{-}3500$ cm^{-1} .



Figure 3.12 The photo of BRUKER RAM II VERTEX 70.

3.3 Electrochemical measurements

The three-electrode configuration in aqueous electrolyte was used to study the electrochemical behaviors of the prepared electrodes by using an autolab potentiostat galvanostat (PGSTAT 302N) as shown in Figure 3.10. Three popular techniques for measuring electrochemical properties of the samples are cyclic voltammetry (CV), electrochemical impedance spectroscopy (EIS), and galvanostatic charge/discharge (GCD) techniques. Figure 3.10 gives a schematic view of a cell connected to an electrochemical workstation. The three-electrode system consists of the active materials, a platinum wire (Pt) and silver/silver chloride (Ag/AgCl) electrodes used as working, counter, and reference electrodes, respectively. Basically, the current flows through the CE and the WE, and the voltage is measured (or controlled) between RE and WE (Pongprayoon *et al.*, 2017).

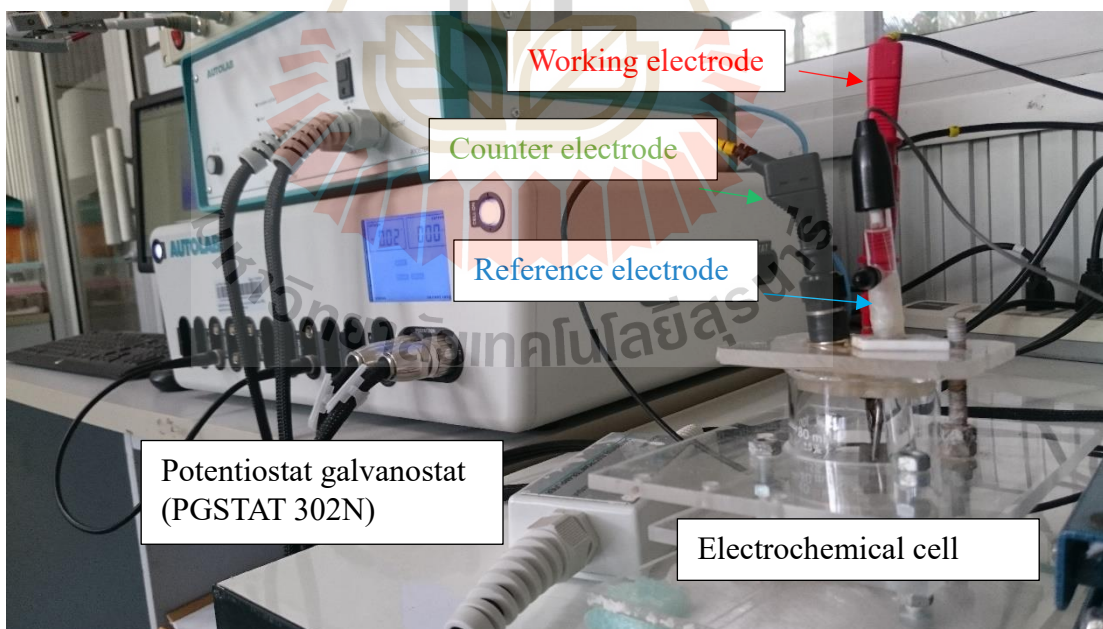


Figure 3.13 Experimental set up of electrochemical measurements, which consist of personal computer, potentiostat/galvanostat, and electrochemical cell.

Nova 1.11 was used to control all instrument and analyze the data obtained from the experiment. Figure 3.13 illustrates the view of the Nava software (version 1.11).

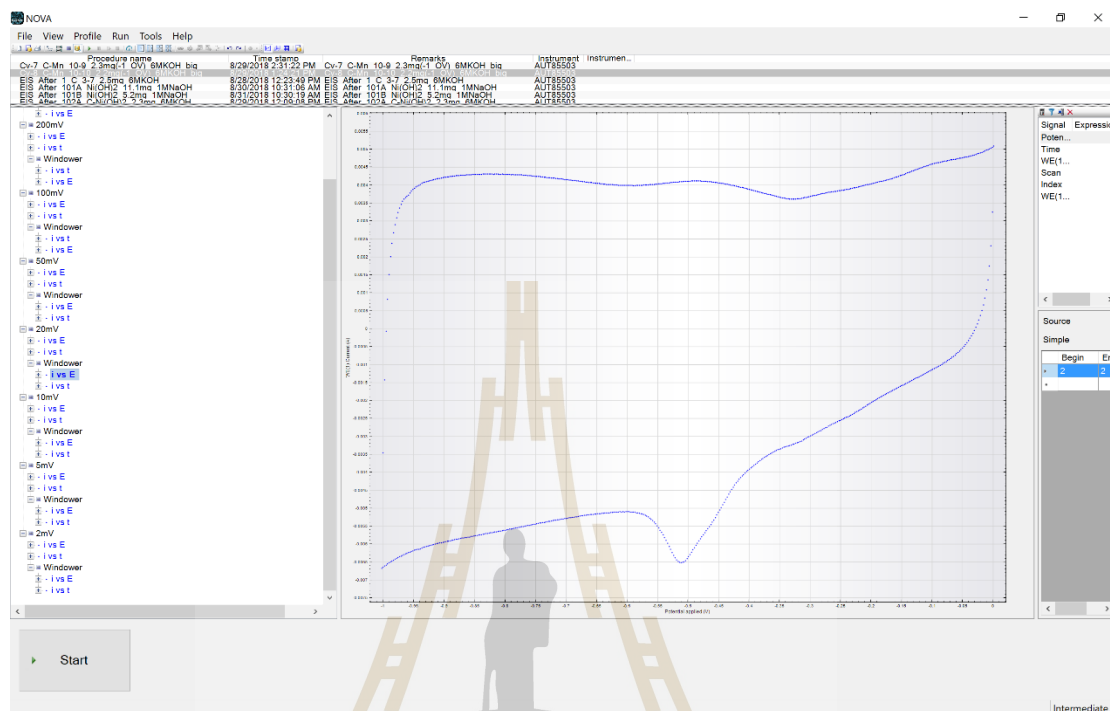


Figure 3.14 The view of the Nova-1.11 software analyzing CV curve.

3.3.1 Cyclic voltammetry

Cyclic voltammetry (CV) is one of electrochemical techniques used to reveal the electrochemical characteristic of the materials by measuring the current, which responds to the various potentials. This technique can provide detailed information on the specific capacitance, potential window, and redox reactions (R.-X. He and Zha, 2017). The plot of the current crossing through the working electrode and counter electrode yields a CV curve as shown in Figure 3.14, which presents three different types of CV curves including ideal capacitor, resistive capacitor, and pseudo capacitor. The CV curve of ideal capacitor has the form of rectangular, which implies that the capacitance would keep constant at various scan rate, while the resistive capacitor has

a form of parallelogram, and the pseudo capacitor has redox peaks which caused by the faradaic reaction of pseudo materials. Multi-peaks will be found in case the sample contains many oxidation states or the sample is the composition of many pseudo materials.

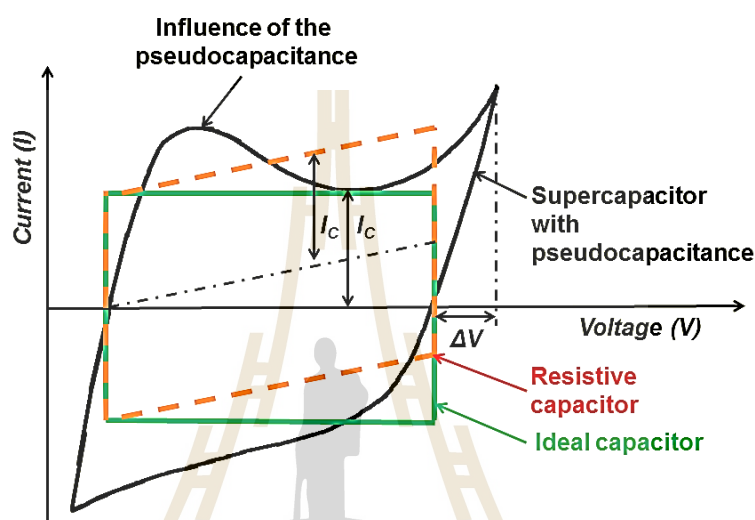


Figure 3.15 Cyclic voltammogram of three different electrochemical capacitors: ideal, resistive, faradaic capacitors (Adapted from <https://en.wikipedia.org/wiki/Pseudocapacitance>).

Reversibility is the important parameter in all electrochemical systems. Cyclic voltammetry can also provide an indication of the degree of reversibility of an electrochemical reaction. By looking at the voltammograms, we can see whether the reaction is reversible or not. There are three types of the electron transfer process including reversible, irreversible and quasi-reversible. In a reversible system, the electrode process is defined as electrochemically reversible when the rate of the electron transfer is higher than the rate of the mass transport. The electron transfers with rapidly rate in both forward and reverse scan. The current ratio between the reverse

peaks (cathodic peaks, $I_{p,c}$) and the forward peaks (anodic peaks, $I_{p,a}$) is constant and equal to 1.0 and proportional to the concentrations of the active species. The peak current (i_p) at room temperature is given by the Randles-Sevcik equation (Brownson and Banks, 2014; Nithya *et al.*, 2013):

$$i_p^{\text{rev}} = 2.687 \times 10^{-5} n^{3/2} ACD^{1/2} v^{1/2} \quad (3.9)$$

where n , A , C , D and v are the number of electron transferred/molecule, the electrode surface area (cm^2), the concentration (mol/cm^3), the diffusion coefficient (cm^2/s), and the potential scan rate (V/s), respectively. The anodic ($E_{p,a}$) and cathodic peak potentials ($E_{p,c}$) are independent of the scan rate. The separation between the potentials of the forward and reverse peaks (called peak-to-peak separation), ΔE_p , at room temperature, at all scan rates is equal to

$$\Delta E = E_{p,a} - E_{p,c} = \frac{0.059}{n} \text{V} \quad (3.10)$$

In an irreversible process, the electron transfer is lower than that of the mass transport and the rate electron transfer in the reverse scan is very slow. The peak current and the peak potential, respectively are given by

$$i_p^{\text{irrev}} = 0.4958 nFACD^{1/2} \left(\frac{\alpha n_a F}{RT} \right)^{1/2} v^{1/2} \quad (3.11)$$

$$E_p = E^0 - \frac{RT}{\alpha n_a F} \left[0.78 - \ln \frac{K^0}{D^{1/2}} + \ln \left(\frac{\alpha n_a F v}{RT} \right)^{1/2} \right] \quad (3.12)$$

where α and n_a are the transfer coefficient and the number of electrons involved in the charge transfer step, respectively, F is faradays constant (96,500 C/mol), α is transfer coefficient, R is gas constant (8.3145 J/mol K) and T is temperature (K). In irreversible process, the cathodic and anodic peak potentials are dependent of the scan rate. A quasi-reversible process is common that in electron transfer processes one observes that at low scan rates the process behaves reversibly, whereas at high scan rates the process behaves irreversibly (such behavior is more easily seen for processes that are not complicated by coupled reactions). Processes occurring in the transition zone between reversible and irreversible behavior are called quasi-reversible. A quasi-reversible process occurs when the rate of the electron transfer is of the same order of magnitude as the mass transport. The voltammograms of a quasi-reversible system exhibit a larger separation in peak potentials compared to a reversible system (Randviir, 2018).

In cyclic voltammetry, the specific area of the electrode is proportional to the enclosed area of the CV curve and it can be calculated by the following equation (Budhiraju *et al.*, 2017):

$$C_{CV} = \frac{1}{vm\Delta V} \int IdV \quad (3.13)$$

where I is the response current (A), v is the potential scan rate ($mV s^{-1}$), m is the mass of the electroactive materials in the electrodes (g), and ΔV is the potential window (V).

In this work, the cyclic voltammetry measurement was performed at a potential window in the range of -1 V to 0 V and different scan rates of 2, 5, 10, 20, 50, 100, 200, and 500 mV s⁻¹ were applied in 6 M KOH at room temperature.

3.3.2 Galvanostatic charge/discharge

The charging–discharging (GCD) technique is used to determine the kinetics and mechanism of electrode reactions by measuring the discharge time at the certain current density. Generally, this technique is also one of the most reliable approaches to determine specific capacitance, energy density, power density, and cycle life of a supercapacitor. The process of GCD measurements is based on the measuring the charge/discharge time at a certain current density, which this charge/discharge time can provide the data to calculate specific capacitance and other properties.

In this work, the GCD curves at different current densities of 0.5, 1, 2, 5, and 10 A g⁻¹ were tested to investigate the capacitance performances of the electrodes. The specific capacitance C_{CD} , energy density (E), and the power density (P) can be calculated by the following equation (W. Wu *et al.*, 2019):

$$C_{CD} = \frac{I \cdot \Delta t}{m \Delta V} \quad (3.15)$$

$$E = \frac{C_{CD} \cdot \Delta V^2}{2 \times 3.6} \quad (3.16)$$

$$P = \frac{E \times 3600}{\Delta t} \quad (3.17)$$

where I is the current (A), Δt is the discharge time (s), m is the active mass (g), ΔV is the potential window, and C_{CD} is the specific capacitance from charge/discharge

technique ($F \text{ g}^{-1}$), E is the energy density (Wh. kg^{-1}), and P is the power density (W kg^{-1})

3.3.3 Electrochemical impedance spectroscopy (EIS)

Electrochemical impedance spectroscopy (EIS) is a powerful technique used to characterize the properties of electrode-electrolyte interfaces related to metal corrosion and electrodeposition for energy storage devices which EIS can provide the specific capacitance and equivalent resistance (Cougnon *et al.*, 2015). In the operation, the small-amplitude of sinusoidal potential is applied to the cell electrode to measure the response current to get the impedance of the system. The apply-sinusoidal potential and the responding current ($\Delta I(\omega)$) are given as (Z. Zhao *et al.*, 2017):

$$\Delta I(\omega) = \Delta I e^{j(\omega t + \phi)} \quad (3.18)$$

where I is the current amplitude. $\omega = 2\pi f$ is the angular frequency, and Φ is phase shift between current response and the potential. The electrochemical impedance $Z(\omega)$ is defined as

$$Z(\omega) = \frac{\Delta V}{\Delta I} = |Z(\omega)|e^{-j\phi} = Z' + jZ'' \quad (3.19)$$

where Z' and Z'' are the real part and the imaginary part of the impedance, respectively defined as

$$Z'^2 + Z''^2 = |Z(\omega)|^2 \quad (3.20)$$

The impedance responses recorded by the EIS instrument are normally shown as Nyquist plots that illustrate the relationship between imaginary part impedance ($-Z''$) and real part impedance (Z') based on the equivalent circuit having the components of equivalent series resistance (R_s), charge-transfer resistance (R_{ct}), constant phase element (CPE) and Warburg impedance (W). The intercept in the Z' axis at a high frequency refers to R_s which stands for Ohmic resistance of the electrolyte, internal resistance of the electrode material and contact resistance at the electrode/current collector interface. The semicircle diameter at high frequency region corresponds to charge transfer resistance (R_{ct}) in which caused by faradic reaction. The slope of the linear curve at low frequency is called the Warburg resistance (W) and was used to describe the frequency dependent of ion diffusion into the bulk of the electrode surface (Budhiraju *et al.*, 2017). For none-ideal cell or cell with lack of surface homogeneity, the constant phase element (CPE or Q) is used. The parameter 'n' obtained from CPE is used to observed the quality of the electrode material ($n=1, 0$ and $0.5 < n < 1$) indicates the ideal capacitors, the insulators, and the moderate capacitor behavior, respectively. To observe these parameters, analysis of EIS data can used by modeling or fitting of impedance spectra with an equivalent circuit (EC). Depending on the shape of the EIS spectrum, the EC model is usually composed of resistors (R), conductors (L), and capacitors (C) connected in series or in parallel. After an EC is designed, it can be used to fit the EIS spectra with a software program (Yadav *et al.*, 2016). In this work, the EIS measurement was collected with a frequency range of 0.1 HZ to 100 kHz.

CHAPTER IV

RESULTS AND DISCUSSION

Chapter IV exhibits the experimental results and their discussions, which could be classified into three sections related to the types of the samples including (i) carbon nanofibers (CNF) and porous carbon nanofibers (P-CNF), (ii) interconnected carbon nanofibers (IC-CNF), and (iii) carbon/manganese oxide core-shell composite nanofibers (C/MnO_x). For each group of study, the crystal structures and phase compositions of the synthesized nanoparticles could be determined by using X-ray diffraction (XRD) results. The morphologies of the nanoparticles were investigated by scanning electron microscope (SEM) and transmission electron microscope (TEM). The qualities of carbon materials were characterized by Raman technique. The specific surface area and pore distribution were evaluated by Brunauer–Emmett–Teller (BET) method and Barrett-Joyner-Halenda (BJH) method, respectively. The electrochemical behaviors of different electrode materials were studied by cyclic voltammetry (CV), galvanostatic charge–discharge, and electrochemical impedance spectroscopy (EIS) method, respectively.

4.1 CNF and P-CNF

4.1.1 Structure and morphology characterization

4.1.1.1 Thermogravimetric analysis (TGA) of PAN nanofibers

The DSC of the as-spun-PAN nanofibers was obtained under a nitrogen atmosphere with the flowing rate of 100 ml min^{-1} . The temperature ranged from 25°C to 1200°C with the heating rate of $10^\circ\text{C min}^{-1}$. As displayed in Figure 4.1(b), the curve appeared with its main exothermic peak at $\sim 280^\circ\text{C}$. This suggests the decomposition temperature of the sample (Delgado-Mellado *et al.*, 2018). Figure 4.1(a) illustrated the weight loss of the as-spun-PAN sample studied by using TGA. The weight loss of the as-spun sample started above 280°C and maximized at $\sim 500^\circ\text{C}$ and continued till $\sim 1120^\circ\text{C}$ where the weight loss at this temperature is $\sim 98\%$. The degradation occurred in three steps. First, the tiny weight loss below 100°C concerned the removal of humidity and solvent. Second, the weight loss at mild temperature $\sim 200\text{--}300^\circ\text{C}$ can be explained as the infusible ladder polymer forming before calcination. The main weight loss occurs at 300°C till 460°C and continue till 1120°C . This indicates the pyrolysis of polymer structure of the fibers which is consistent with the DSC results (Hsieh *et al.*, 2018).

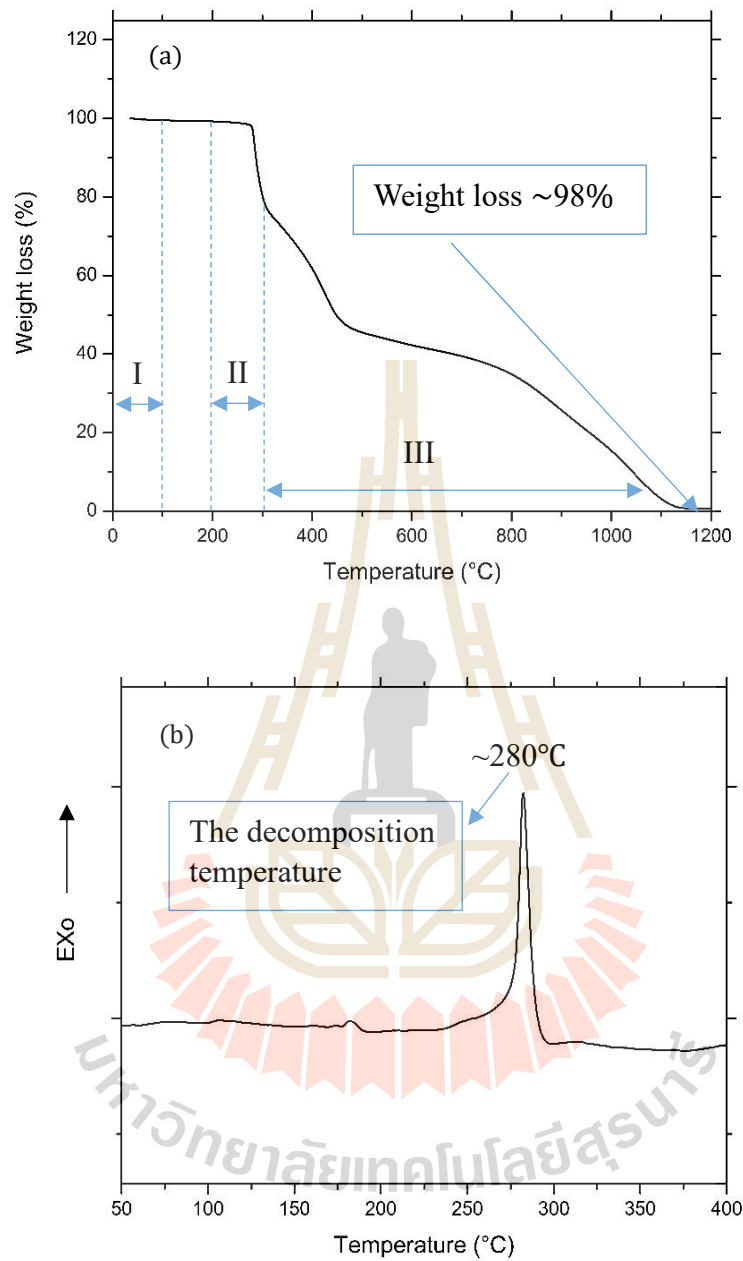


Figure 4.1 TGA (a) and DSC (b) of as-spun-PAN nanofibers.

4.1.1.2 X-ray diffraction (XRD) analysis of CNF

The XRD spectrum of the CNF as presented in Figure 4.2 was measured with Cu K α wavelength of 1.54 Å between 2θ from 10° to 80°, with step time 0.2 and step size 0.02. The broad-peak pattern shows the characteristic of amorphous carbon in the sample (Jingjing Ding *et al.*, 2018). Besides, the diffraction peaks at around $2\theta = 26^\circ$, 42° , and 44° indicate the formation of graphite structure, which can be indexed to (002), (100) and (101) planes and the value of d-spacing parameters of 3.4, 2.1, and 2.0 Å, respectively (JCPDS card no. 12-0212) (S. Yang *et al.*, 2012). No other characteristic peaks were detected.

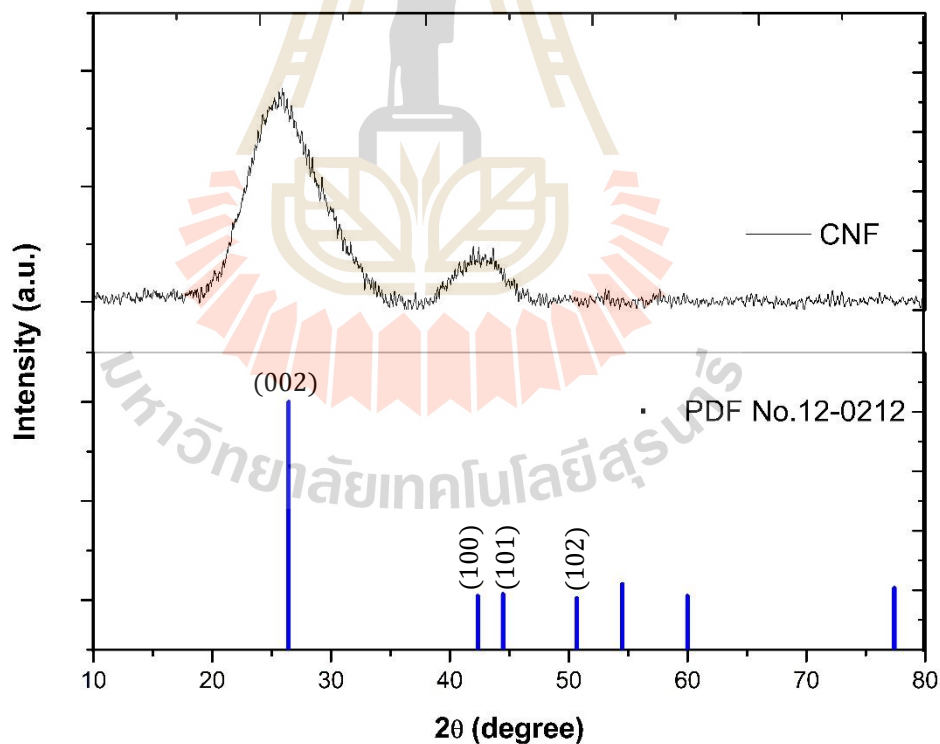


Figure 4.2 The XRD pattern of CNF with the standard.

4.1.1.3 SEM analysis of CNF and P-CNF

The morphologies of the samples were revealed by the high magnification SEM images. Figure 3 revealed the SEM images of electrospun carbon nanofibers (a-c) and electrospun porous carbon nanofibers (d-f). In general, all samples displayed a few rough surfaces of long-uniform and randomly-arranged nanofibers. For CNF, the average diameter of 400 ± 26 nm were measured, which most of the fiber diameters were in the ranges between 350-450 nm as exposed by the histogram plot (subset Figure 4.3(a)). On the other hand, the P-CNF has a smaller average diameter of 146 ± 23 nm, which most of the fiber diameters were in the ranges between 100-200 nm as presented by the histogram plot (subset Figure 4.3(d)). The macropores were observed in P-CNF with the average size of 46 ± 10 nm as exposed in Figure 4.3(e), which most of the pores were in the ranges between 40-60 nm as revealed by the histogram plot (subset Figure 4.3(e)). A lot of micropores were noticed as a major pores in PCNFs and their properties will be determined by the gas adsorption/desorption technique. Moreover, a lot of macropores were also observed in the P-CNF where these types of pore can increase specific capacitance of the material because of the enhancement of surface area which is utilized as the active sites for electrolyte ions (M. Chen *et al.*, 2017). These porous structure of the samples might be caused by two main reasons: (i) the pores may be created by the melting of the paraffin oil at the high temperature during the carbonization process, and (ii) the reaction of CO_2 on the surface of carbon nanofibers during the activation process (Y. Liu *et al.*, 2018).

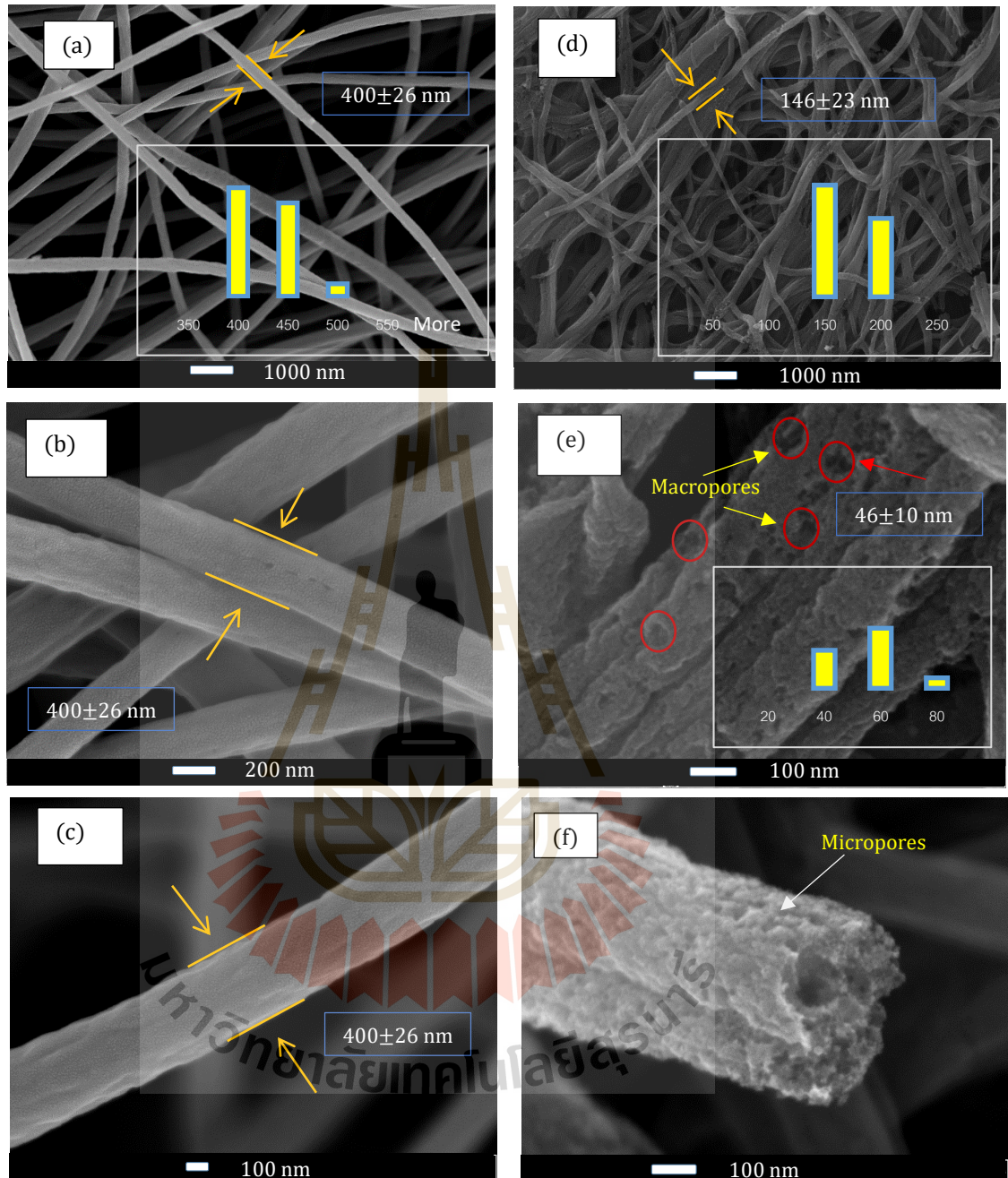


Figure 4.3 The SEM images of CNF (a), (b), and (c), and P-CNF (d), (e), and (f) at different magnifications.

4.1.1.4 Gas adsorption analysis

The specific surface areas and pore characters of all samples were determined by measuring N₂ adsorption/desorption. As presented in Figure 4.4(a), the isotherm curve of CNFs had a character of type III isotherm, which was nonporous type and it had weak interaction between the sample surface and the adsorbate. However, the isotherm curve of P-CNF had a character of combining of type I and type IV isotherm, which were micropore and mesopore respectively. In type I and type IV, the interaction between the sample surfaces and the adsorbates were relatively strong (P. B. Balbuena and Gubbins, 1993). Figure 4.4(b) exhibited the pore-size distributions of the samples determined by using both BJH and MP methods. CNFs had mean pore diameter of 14 nm, which was the diameter of mesopore while PCNFs had mean pore diameter of 1.8 nm, which was the diameter of micropore. Between the two samples, P-CNF had much higher specific surface area of 677m² g⁻¹. Unfortunately, the value of specific areas getting from BET technique for this materials, which have micropores (pore size less than 2 nm) and small mesopore had errors. This was because the measured isotherm was a weighted average over the adsorption because of the effects of pore size, pore shape, active adsorption sites, and blocked and networked pores (P. B. Balbuena, and Gubbins, K. E. , 1993; Mahle, 2002). Other parameters were listed in Table 4.1.

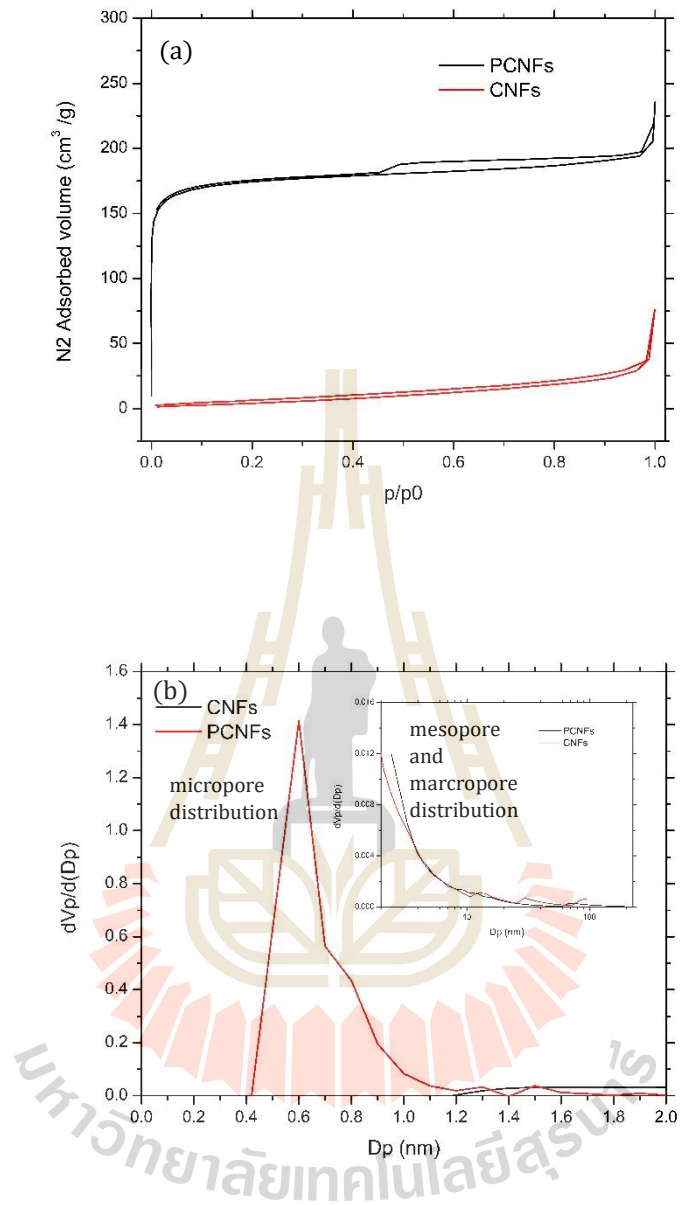


Figure 4.4 (a) N_2 adsorption and desorption isotherm of the samples. (b) Micropore distributions of the samples and (insert) mesopore and marcropore distribution of the samples.

Table 4.1 The textural parameter CNFs and PCNFs obtained by BET, BJH, and MP methods.

Sample	S_{BET} [m^2g^{-1}]	D_{m} [nm]	V_{tot} [cm^3g^{-1}]	V_{mi} [cm^3g^{-1}]	V_{me} [cm^3g^{-1}]
CNFs	20	14.03	0.07	0.01	0.08
PCNFs	677	1.86	0.31	0.29	0.01

4.1.2 Electrochemical properties of CNF and P-CNF

The electrochemical properties of CNF and P-CNF were studied by the cyclic voltammetry (CV), galvanostatic charge/discharge (GCD), and electrochemical impedance spectroscopy (EIS). The experiments were conducted in the three-electrode configuration system in 6 M KOH aqueous electrolyte. The working electrodes were prepared by sandwiching the samples between the nickel foams and pressing at very low pressure for 1 min, subsequently, they were soaked in the electrolyte overnight before doing measurements. In CV measurement, the potential windows were chosen from -1 to 0 V and the scan rate in the range of 2, 5, 10, 20, 50, 100, 200, 500 mV s^{-1} . The CD testing was measured with the same voltage window as CV measurement at the current densities in the range of 0.5, 1, 2, 5, and 10 A g^{-1} . The impedance behavior of electrode was tested in a frequency range between 0.1 and 10^5 Hz.

4.1.2.1 Cyclic voltammetry (CV) measurement

The capacitive behaviors of the electrodes were determined by plotting the CV curve at 500 mV s^{-1} and 2 mV s^{-1} . As displayed in Figure 4.5(a), at high scan rate the curves of both CNF and P-CNF behaved nearly as a rectangular curve of an ideal capacitor without any redox peaks, which indicated that the double layer capacitive

processes mainly stored the charges of the electrode. Moreover, the CV curve of Ni foam was also plotted to make a comparison. As a result, the loop of Ni foam CV curve is too small comparing with the loops of the CV curves of samples. Figure 4.5(b) indicated the CV curves of the samples, which also behaved nearly as a rectangular curve. It was noteworthy that the samples started to display resistive behaviors at the operating potential -0.1 V, which was the cathodic current from the decomposition of the aqueous electrolyte (L. Chen *et al.*, 2013). These phenomena indicated over potential region that implied the limitation of CNF. However, in both cases, the loops of CV curves of CNFs seem bigger than the loops of CV curves of P-CNF. This implied that the specific capacitance of CNFs was greater than the specific capacitance of PCNFs. Figure 4.5(c) presented the plot of specific capacitances of the samples versus scan rates. For CNF, as the scan rates increased, the specific capacitance also increased with the scan rates from 2 to 20 mV s^{-1} . Then, the specific capacitance reached a maximum value between 20 and 50 mV s^{-1} , and the decrease of specific capacitances were found above 100 mV s^{-1} indicating the diffusion of electrolyte ions was limited because of the time constraint and only the outer surface provided charge accumulation (S.-J. Park *et al.*, 2012; Pech *et al.*, 2010). Moreover, this limitation was possibly proposed as the double layer growth and blocked the ions before they accessed the full region in the micropore. However, for P-CNF, as the scan rate increased, the specific capacitance always decreased.

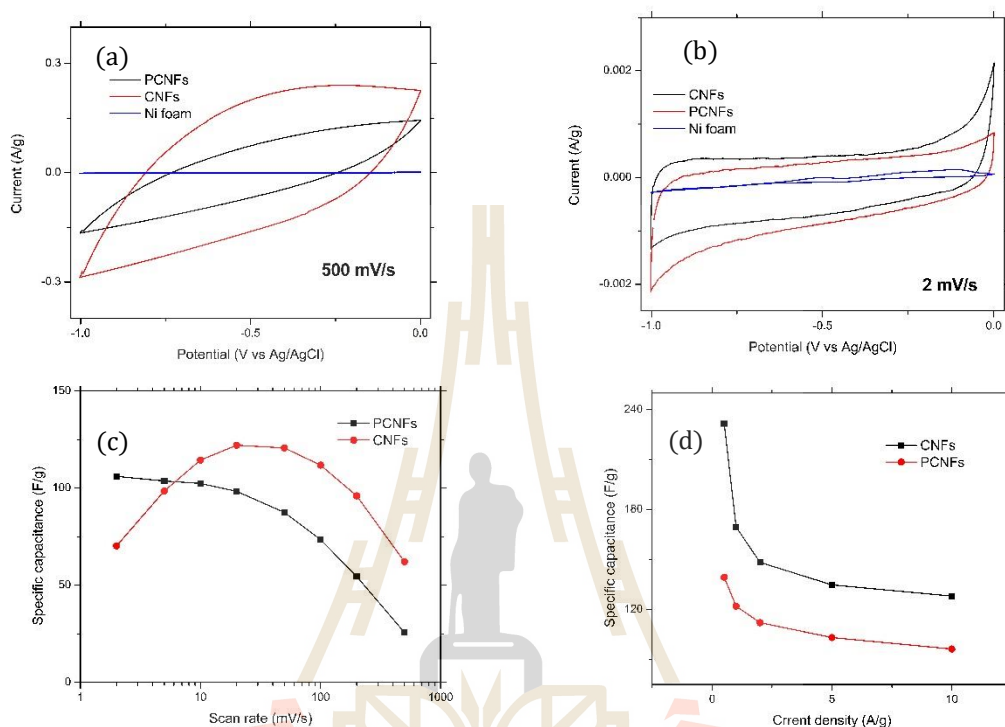
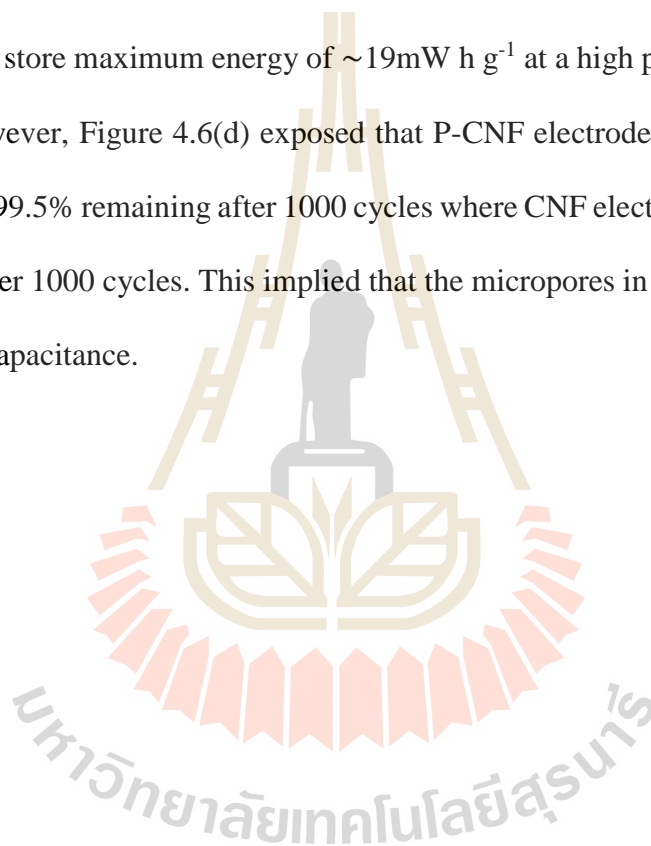


Figure 4.5 The CV curves of both samples at scan rate (a) 500 mV s^{-1} and (b) 2 mV s^{-1} ; the plot of specific capacitance as a function of scan rates (c) and current densities (d).

4.1.2.2 Galvanostatic charge/discharge (GCD) measurement

The linear voltage-time profile of GCD measurement of both samples at the current density of 10 A g^{-1} and 0.5 A g^{-1} were presented by Figure 4.6(a) and (b), respectively. Between these two samples, CNF electrode displayed the longest duration of ions charging/discharging at each current density. Figure 4.5(d) displayed that the

specific capacitances of all samples decreased with an increase of current density. In that, the specific capacitances of CNF were greater than the specific capacitances of P-CNF with all current densities. A comparison of power and energy density of all electrode is represented by the well-known Ragone plot as displayed in Figure 4.6(c). The CNF electrode can store maximum energy of $\sim 32 \text{ mW h g}^{-1}$ at a high power density of $\sim 249 \text{ mW g}^{-1}$, which demonstrates faster charging/discharging where P-CNF electrode can store maximum energy of $\sim 19 \text{ mW h g}^{-1}$ at a high power density of $\sim 247 \text{ mW g}^{-1}$. However, Figure 4.6(d) exposed that P-CNF electrode had a greater cycling stability of $\sim 99.5\%$ remaining after 1000 cycles where CNF electrode has only $\sim 95.9\%$ remaining after 1000 cycles. This implied that the micropores in the fibers could affect the specific capacitance.



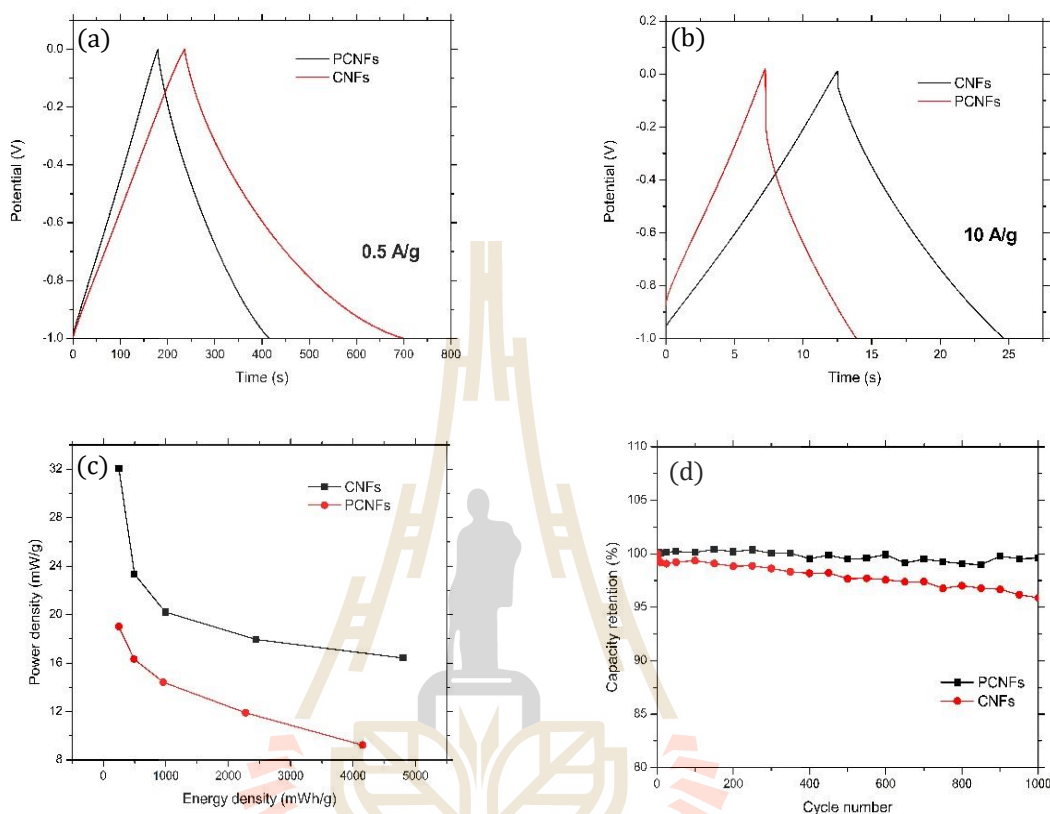


Figure 4.6 The GDC curves of both samples at the current density of 0.5 A g⁻¹ and (b) 10 A g⁻¹; (c) Ragone plots of both samples, and (d) capacity retention.

4.1.2.3 Electrochemical impedance spectroscopy (EIS) measurement

EIS experiment was performed in the frequency range of 0.1 Hz to 100 kHz at amplitude of 0.1 V to understand more about electrochemical performance of all samples. EIS data are generally presented as a Nyquist plot, which is a plot of imaginary part ($-Z''$) versus the real part (Z'). As revealed in Figure 4.6(a), there were three regions

to be considered in Nyquist plot including high frequency region, mid-frequency region, and low frequency region. In the high frequency region, the intercept of the real axis indicated the bulk resistance (R_s), which was the total resistance of pore-electrolyte resistance, bulk resistance, and a contact resistance causing by the electrode and current collector surface (X. He *et al.*, 2017). By fitting the semicircles of the measured data, the R_s values of CNF and P-CNF were estimated to be 300.53 m Ω , and 456.00 m Ω , respectively. At the middle frequency, the diameter of semicircle corresponded to the charge transfer resistance (R_{ct}) which was caused by Faradaic reaction (Xiao *et al.*, 2017). As seen in Figure 4.7(b), some big-diameter semicircles were observed at this region, which interpreted that all electrodes exhibited little characteristics of Faradaic reaction. Last, in the low frequency region, almost straight lines with an angle about 20° along the vertical axis were observed for CNF and wider angle was observed for P-CNF. The slopes of the curves corresponded the Warburg impedances which represented the electrolyte diffusion in the electrode material (Sun *et al.*, 2017). It was noticed that the CNF electrode showed the smaller vertical slope compared with the vertical axis, which indicated that this electrode materials had lower Warburg impedance. The value of R_{ct} , R_s , and N values of all samples were displayed in Table 4.2.

Table 4.2 The textural parameter of CNFs and PCNFs obtained by BET, BJH, and MP methods.

Sample	R_s [m Ω]	R_{ct} [m Ω]	N value
CNFs	300.53	298.29	0.99431
PCNFs	456.00	137.90	0.99663

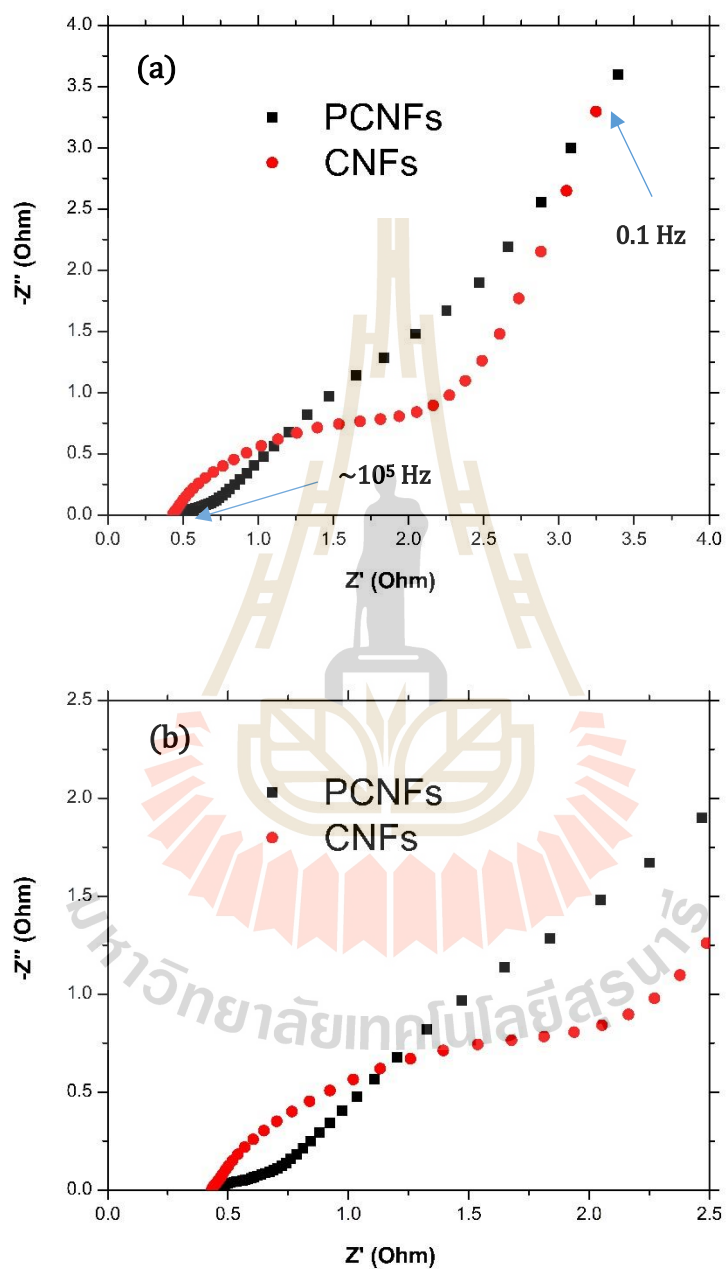


Figure 4.7 The Nyquist impedance plots at a frequency range of 0.1 Hz-100 kHz in 6 M KOH electrolyte solution of CNF and P-CNF electrodes.

4.2 Interconnected carbon nanofibers IC-CNF

4.2.1 Structure and morphology characterization

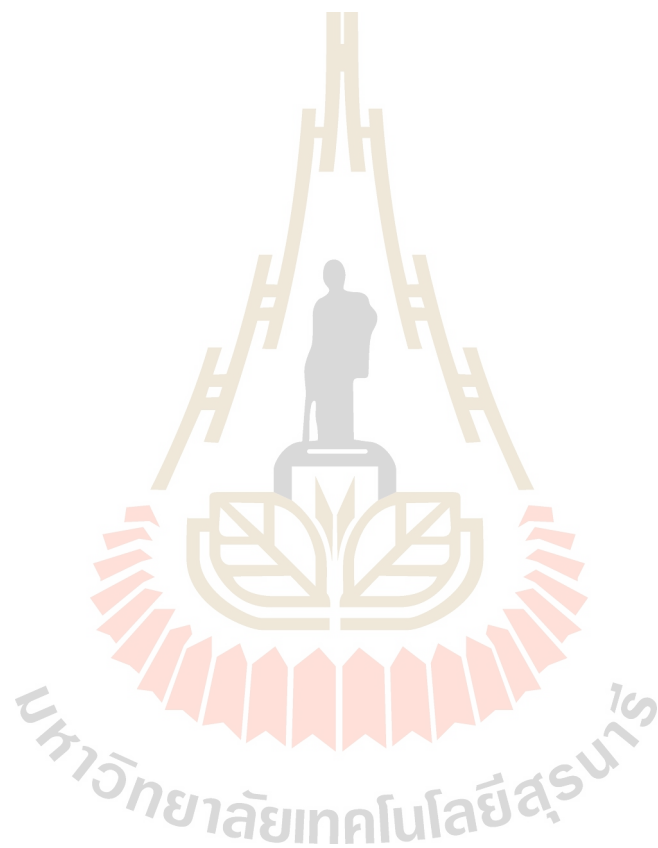
4.2.1.1 Thermogravimetric analysis (TGA) of PAN_3-7, PAN_2-8, PAN_1-9, CS-PVP, and CS-PAN nanofibers

Figure 4.8(a) displayed the DSC curves of the samples, which the experiments were measured under the nitrogen atmosphere with the flow rate of 100 ml min⁻¹, the heating rate of 10 °C min⁻¹, and the temperature range from 25 °C to 1000 °C. The as-spun PAN_3-7, PAN_2-8, and PAN_1-9 curves appeared with its main exothermic peak at about 293 °C while the as-spun CS-PAN and CS-PVP appeared at about 295°C.

The weight losses of all samples were determined by the study of TGA analysis. In general, for as-spun PAN and composite PAN nanofibers, the degradation occurred through three main steps. The first step in region I was related to the removal of humidity at below 100°C. Second in region II, at the temperature about 200-300°C, the weight loss was related to the infusible ladder polymer forming before carbonization. For this step, the as-spun CS-PVP and CS-PAN had higher stabilization temperature, which implied that these samples were more stable than the others (Youe *et al.*, 2016). The last step in region III was related to the pyrolysis of the polymer structure of the fibers at the temperature about 400–600°C (Yoo *et al.*, 2017). As shown in Figure 4.8(b), the weight loss of the as-spun samples started above 290°C and maximized at about 500°C, which the weight loss in this temperature were in the range between 73% and 65%, and occurred continuously until the temperature of 1000°C. The total weight loss was measured about 88, 80, 85, 88, and 88% at 1000°C for

PAN_3-7, PAN_2-8, PAN_1-9, CS-PVP, and CS-PAN as-spun nanofibers, respectively.

The cause of shift temperature of weight loss from the lower to the higher temperature comparing to pure PAN sample was caused by the PVP content embedding in the sample.



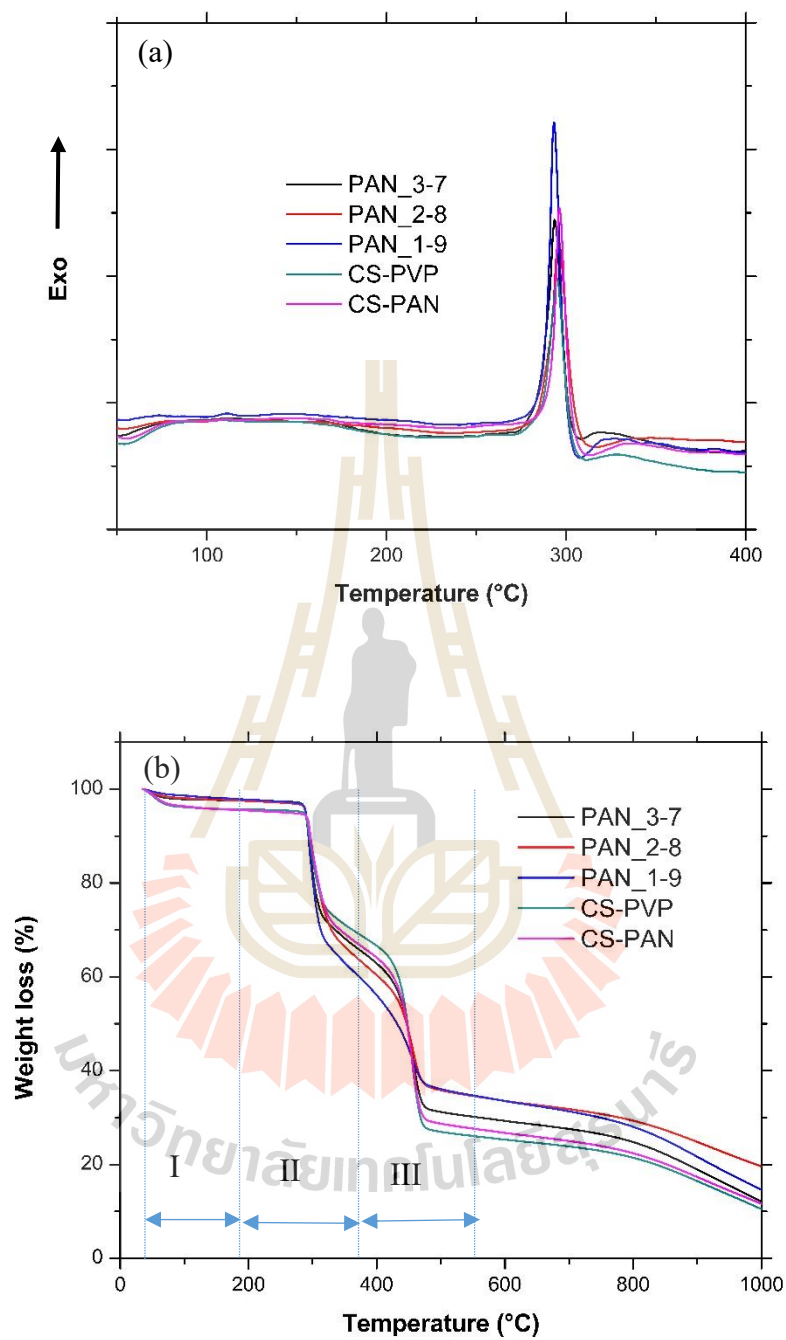
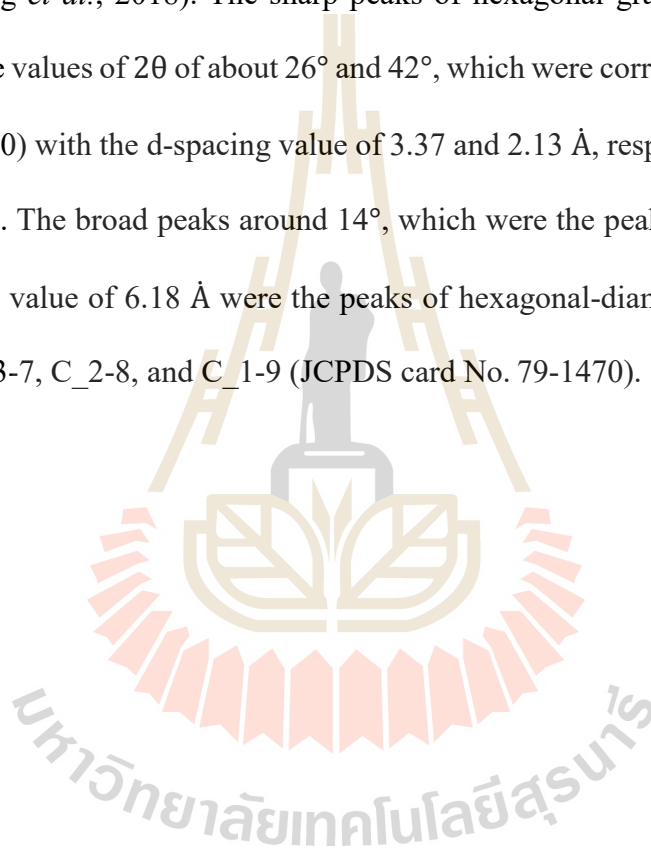


Figure 4.8 The TGA (a) and DSC (b) curves of PAN_3-7, PAN_2-8, PAN_1-9, CS-PVP, and CS-PAN nanofibers.

4.2.1.2 X-ray Diffraction (XRD) analysis of C_3-7, C_2-8, C_1-9, CS-PVP, and CS-PAN

Figure 4.9 displayed the XRD patterns of all samples measured by Cu K_{α} with wavelength of 1.54 Å, 2θ from 10 to 80°, step size 0.02 and step time 0.2. The broad-peak pattern showed the characteristic of amorphous carbon in the sample (Jingjing Ding *et al.*, 2018). The sharp peaks of hexagonal graphite appeared in the samples at the values of 2θ of about 26° and 42°, which were corresponding to the plane (002) and (100) with the d-spacing value of 3.37 and 2.13 Å, respectively (JCPDS card No. 12-0212). The broad peaks around 14°, which were the peaks of plane (002) with the d-spacing value of 6.18 Å were the peaks of hexagonal-diamond carbon observed clearly in C_3-7, C_2-8, and C_1-9 (JCPDS card No. 79-1470).



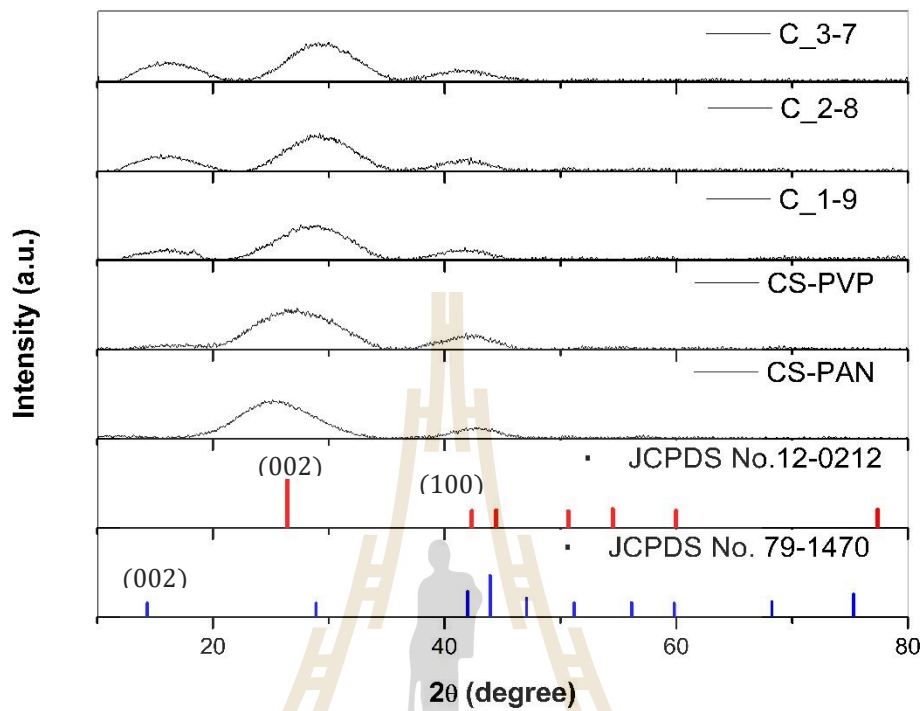


Figure 4.9 The XRD patterns of C_3-7, C_2-8, C_1-9, CS-PVP, and CS-PAN and the references patterns.

4.2.1.3 Raman analysis of C_3-7, C_2-8, C_1-9, CS-PVP, and CS-PAN

The Raman analysis was used to determine the carbon quality of all samples with the wave number in the range between 500 and 3500 cm^{-1} . By using a Lorentzian multi-peaks fitting, the band positions were observed (Carotenuto *et al.*, 2016). As presented in Figure 4.10, there were two main peaks $\sim 1330\text{-}1346 \text{ cm}^{-1}$ (D-Band) and $\sim 1582\text{-}1596 \text{ cm}^{-1}$ (G-Band) occurred in the curves of all samples, which related to the scattering on disordered amorphous carbon cluster (sp^3 bonded carbon atoms) and the stretching of C-C bonds in the hexagonal ring of graphite structure (sp^2 bonded carbon atom) (H. Chen *et al.*, 2014). Another peak was observed around 2704 cm^{-1} (G'-band, which was a two-phonon band taken to be $2 \times 1352 \text{ cm}^{-1}$) (Yan *et al.*, 2014). The biggest I_D/I_G ratio of 0.99 for CS-PVP was obtained from the fitting, which implied that this sample had the phase of amorphous structures. On the other hand, the smallest I_D/I_G ratio of 0.97 for C_3-7, C_2-8, and C_1-9 showed the high graphite structure in the fibers.

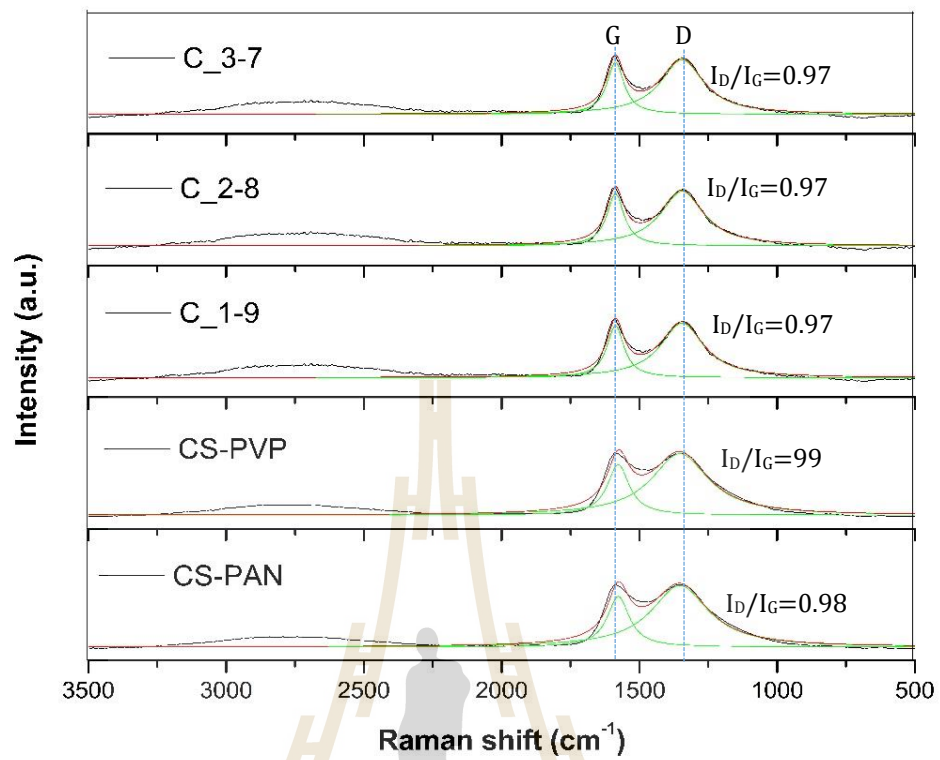


Figure 4.10 The Raman spectra of C_3-7, C_2-8, C_1-9, CS-PVP, CS-PAN, and the references patterns.

4.2.1.4 Scanning electron spectroscopy (SEM) analysis of C_3-7, C_2-8, C_1-9, CS-PVP, and CS-PAN

Figure 4.11(a), (b), (c), and (d) exposed the FE-SEM images of CNF, C_1-9, C_2-8, and C_3-7, respectively, at the magnification of 5 kX, which exhibited a few rough surfaces of long uniform and randomly arranged nanofibers. None of the interconnected fibers were observed in these cases. On the other hand, the interconnected-fiber patterns were observed in the sample CS-PAN and CS-PVP as presented in Figure 4.11(e) and (f) at magnification of 5 kX. These patterns were caused by the melting of PVP content during the calcination as stated in the previous section (Niu, 2012). By using the software ImageJ and Microsoft Excel, the diameters and the average diameters of nanofibers could be measured and calculated, respectively. CNF exhibited the biggest average diameters of about 412 nm and most of the fibers were in the ranges of 400 nm to 500 nm (inset in Figure 4.11(a)). The average diameters of the PAN-PVP blends changed with the difference of PVP-PAN ratios. At the ratio 1:9 of PVP compared with PAN, the fibers had the biggest average diameter of about 254 nm while the smallest average diameter was obtained from the sample with the ratio 2:8. Most of the fibers were in the ranges of 200 nm to 280 nm (inset in Figure 4.11(b)-(d)). The same as above case, there were also no interconnection patterns in these cases. However, the images of CS-PAN and CS-PVP exhibited the fiber-fiber interconnection patterns and the fiber diameters were calculated about 236 nm and 268 nm for CS-PAN and CS-PVP, respectively, and most of the fibers were in the ranges of 200 nm to 300 nm (inset in Figure 4.11(e) and (f)).

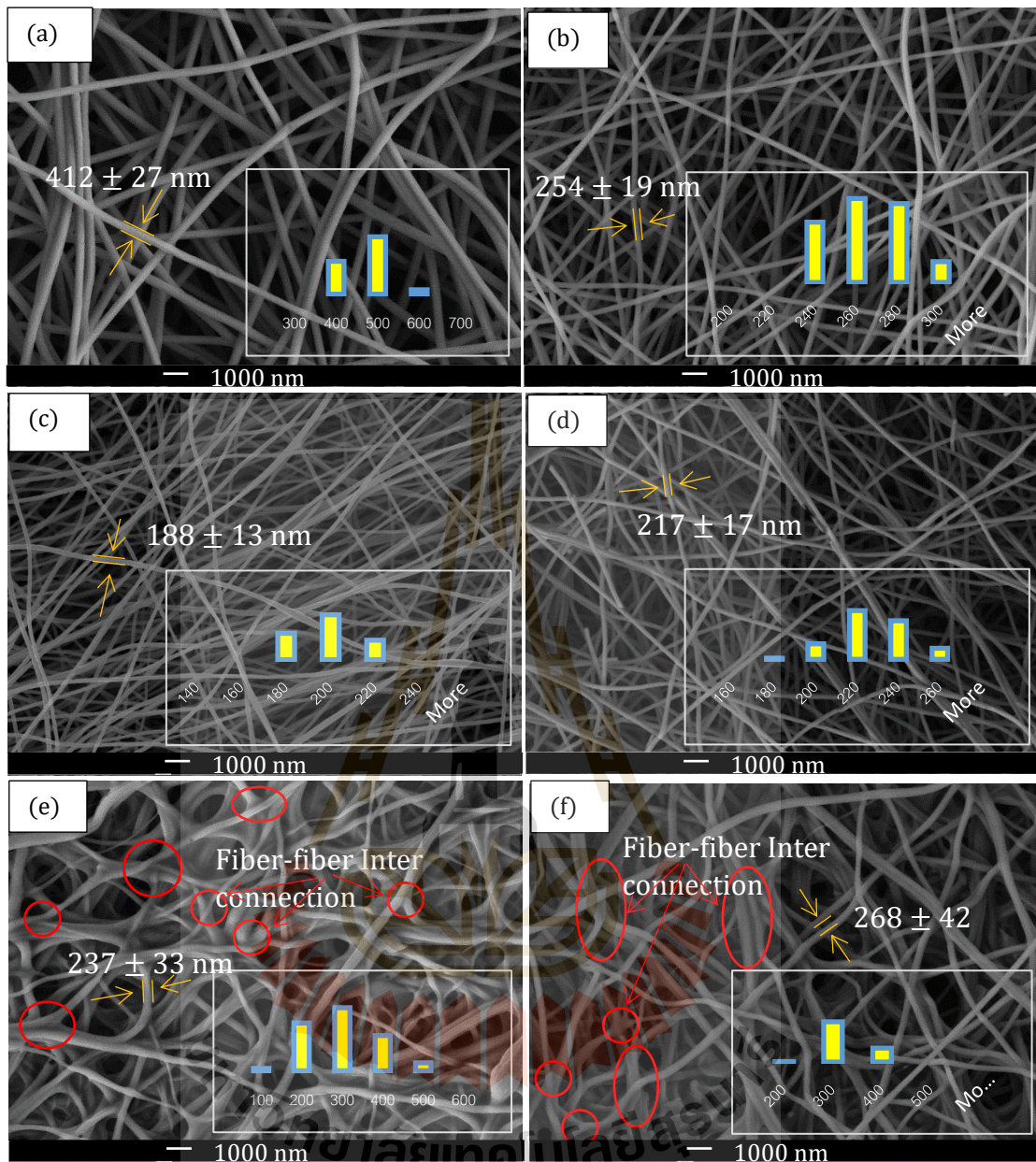


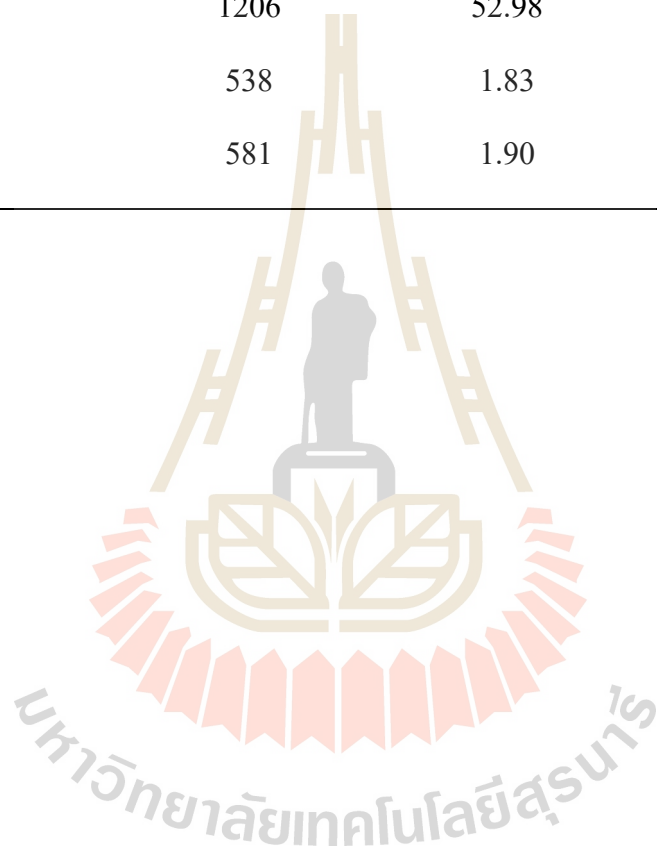
Figure 4.11 The SEM images of (a) CNF, (b) C_3-7, (c) C_2-8, (d) C_1-9, CS-PVP, and (e) CS-PAN.

4.2.1.5 N₂ adsorption/desorption analysis of C_1-9, CS-PVP, and CS-PAN

The pore characters and specific areas of all calcined samples were determined by measuring N₂ adsorption/desorption. Generally, the pore can be classified into three groups depending on the size of the pore, which are micropores, mesopores, and macropores in the range of less than 2 nm, from 2 to 50 nm, and bigger than 50 nm, respectively (P. B. Balbuena, and Gubbins, K. E. , 1993). Figure 4.12(a) revealed the isotherm curves of the samples, which generally displayed small hysteresis loops of type IV isotherm, which is mesopore and parts of type II isotherm, which is macropore. For type II and type IV isotherms, the interaction between sample surface and adsorbate are relatively strong. The pore size distributions of the samples were obtained by using MP and BJH method for micropores and mesoporous, respectively, which were displayed in Figure 4.12(b). C_1-9, CS-PAN, and CS-PVP had micropores with average sizes of about 1.7-1.9 nm. From BET analysis, C_3-7 had the greatest specific area of 1206 m² g⁻¹. The large specific surface areas were very useful for providing many electrochemical reaction sites for electrolyte ions to obtain high electrochemical performance, which were consistent with the electrochemical property results, which we will discuss. The values of specific area and other parameters of all samples were summarized in table 4.3.

Table 4.3 Average diameters of all nanofibers and textural parameters of the samples obtained by BET, BJH, and MP methods.

Sample	S_{BET} ($\text{m}^2 \text{g}^{-1}$)	D_m (nm)	V_m ($\text{cm}^3 \text{g}^{-1}$)
C_1-9	677	1.91	156
C_2-8	773	2.02	1775
C_3-7	1206	52.98	277
CS-PAN	538	1.83	124
CS-PVP	581	1.90	134



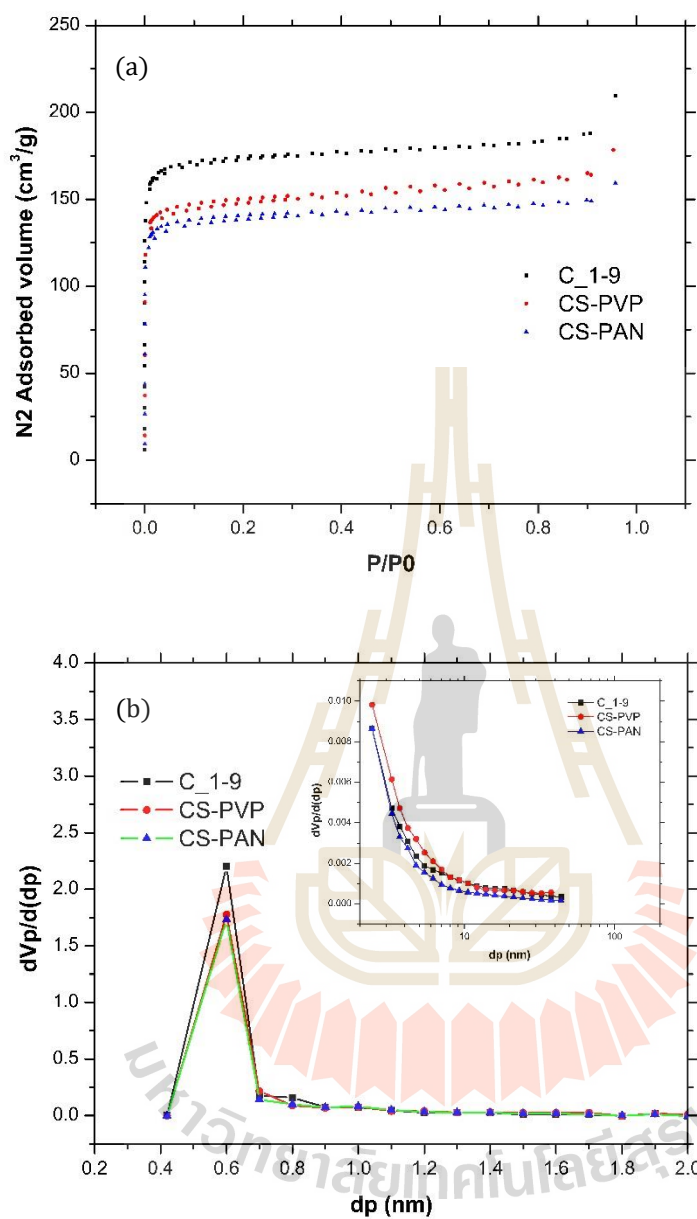


Figure 4.12 (a) N_2 adsorption and desorption isotherm; (b) micropore distribution and (insert) mesopore and macropore distribution of C_1-9, CS-PVP, and CS-PAN.

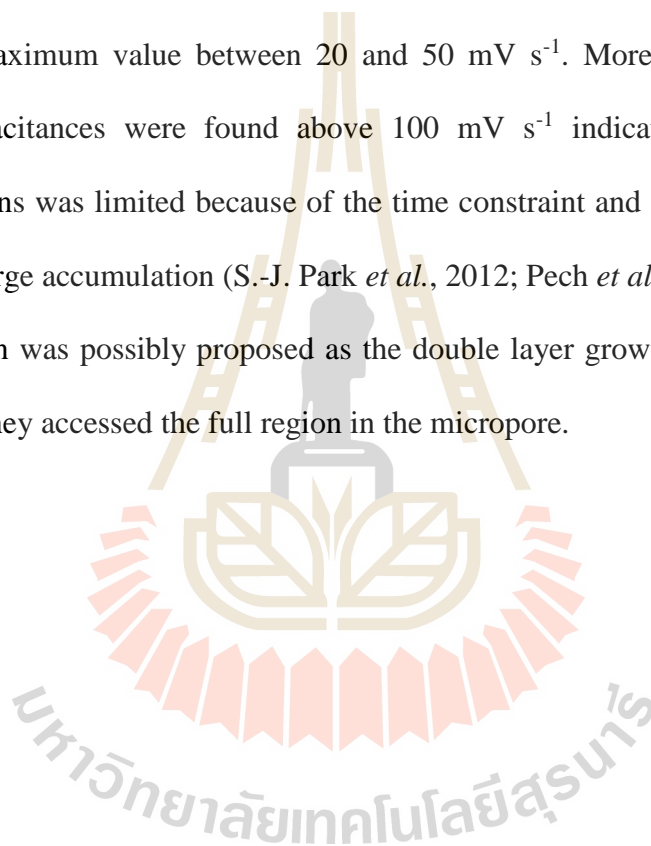
4.2.3 Electrochemical properties of C_3-7, C_2-8, C_1-9, CS-PVP, and CS-PAN

The electrochemical properties of CNF and P-CNF were studied by the cyclic voltammetry (CV), galvanostatic charge/discharge (GCD), and electrochemical impedance spectroscopy (EIS). The experiments were conducted in the three-electrode configuration system in 6 M KOH aqueous electrolyte. The working electrodes were prepared by sandwiching the samples between the nickel foams and pressing at very low pressure for 1 min, subsequently they were soaked in the electrolyte overnight before doing measurements. In CV measurement, the potential windows were chosen from -1 to 0 V and the scan rates in the range of 2, 5, 10, 20, 50, 100, 200, 500 mV s⁻¹. The CD testing was measured with the same voltage window as CV measurement at the current densities in the range of 0.5, 1, 2, 5, and 10 A g⁻¹. The impedance behavior of electrode was tested in a frequency range between 0.1 and 10⁵ Hz.

4.2.3.1 Cyclic voltammetry (CV) measurement

The capacitive behaviors of the electrodes were determined by plotting the CV curve at 500 mV s⁻¹ and 2 mV s⁻¹. As presented in Figure 4.13(a), at high scan rate the curves of all samples behaved nearly as a rectangular curve of an ideal capacitor without any redox peaks, which indicated that the double layer capacitive processes mainly stored the charges of the electrode. At this scan rate, the CV-curve loop of C_3-7 had the biggest loop, which implied that this sample had the greatest specific capacitance at this scan rate. Figure 4.13(b) revealed the CV curves of the samples at the scan rate of 5 mV s⁻¹, which also behaved nearly as a rectangular curve. It is noteworthy that the samples started to display resistive behaviors at the operating potential -0.1 V, which is the cathodic current from the decomposition of the aqueous

electrolyte (L. Chen *et al.*, 2013). This phenomena indicated over potential region that implies the limitation of CNF. In this case, the CV-curve loop of C_1-9 had the biggest loop comparing to other samples, which suggested that this sample had the greatest specific capacitance at this scan rate. Figure 4.13(c) exhibited the plots of specific capacitances of the samples versus scan rates. As the scan rate increased, the specific capacitances of the samples also increased with the scan rate from 2 to 20 mV s^{-1} , then reached a maximum value between 20 and 50 mV s^{-1} . Moreover, the decrease of specific capacitances were found above 100 mV s^{-1} indicating the diffusion of electrolyte ions was limited because of the time constraint and only the outer surface provided charge accumulation (S.-J. Park *et al.*, 2012; Pech *et al.*, 2010). Furthermore, this limitation was possibly proposed as the double layer growth, which blocked the ions before they accessed the full region in the micropore.



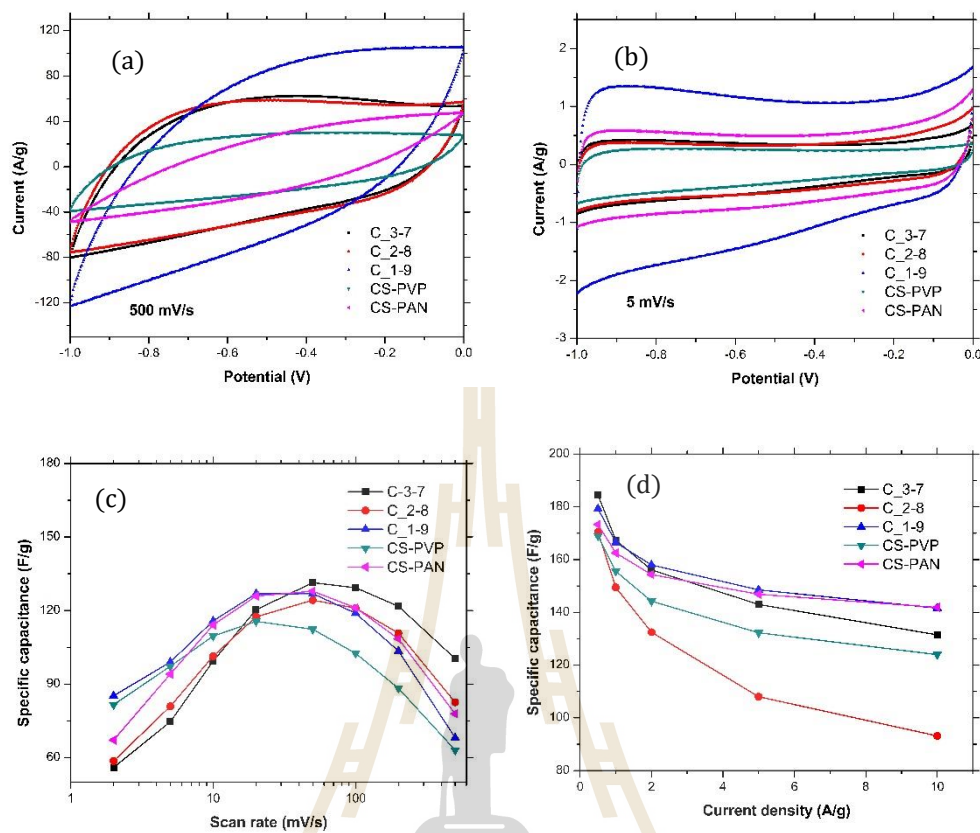


Figure 4.13 The CV curves at the scan rate of (a) 500 mV/s and (b) scan rate 5 mV/s; the plots of specific capacitances vs (c) scan rate and (d) current density of C_3-7, C_2-8, C_1-9, CS-PVP, and CS-PAN.

4.2.3.2 Galvanostatic charge/discharge (GCD) measurement

The linear voltage-time profile of GCD measurement of both samples at the current density of 10 A g^{-1} and 0.5 A g^{-1} were displayed in Figure 4.14(a) and (b), respectively. At the current density of 10 A g^{-1} , C_1-9 and CS-PAN had the long discharge curves whereas at the current density of 0.5 A g^{-1} , C_3-7 had the longest discharge duration. Generally, the longest discharge time represents the greatest specific capacitance. Figure 4.13(d) indicated that the specific capacitances of all samples decreased with an increase of current density. A comparison of power and energy densities of all electrodes was represented by the well-known Ragone plot as in Figure 4.14(c). Concerning about the energy density, the C_3-7 electrode was considered as the greatest electrode, which can store maximum energy of $\sim 26 \text{ mW h g}^{-1}$ at a high power density of $\sim 250 \text{ mW g}^{-1}$. Concerning about power density, CS-PAN had the maximum power density of 4810 mW g^{-1} at the energy density of $\sim 18 \text{ mW h g}^{-1}$, which demonstrated faster charging/discharging. However, Figure 4.4(d) presented that C_2-8 electrode had a greater cycling stability of $\sim 99\%$ remaining after 1000 cycles, where CS-PVP and CS-PAN electrode had only $\sim 96\%$, C_1-9 electrode had only $\sim 97\%$, and C_3-7 had $\sim 92\%$ remaining after 1000 cycles.

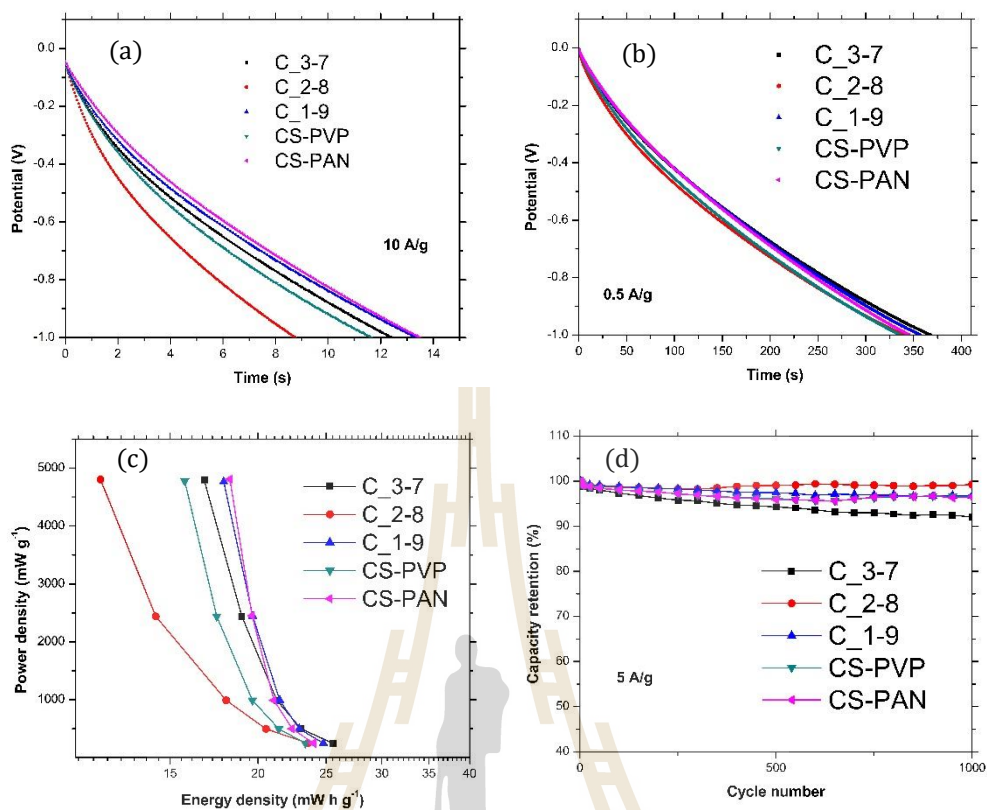


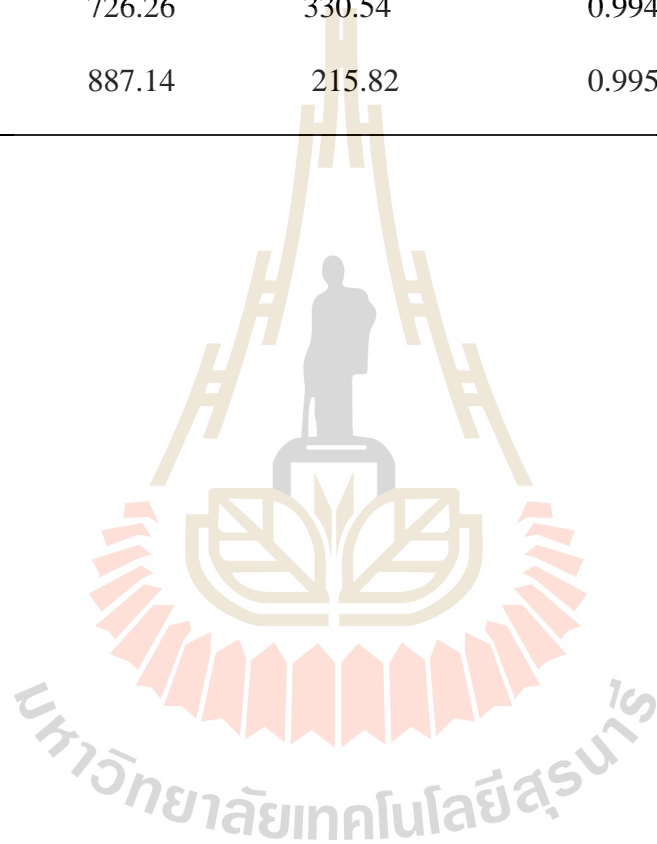
Figure 4.14 The discharge curves at the current density of (a) 10 A g^{-1} and (b) 0.5 A g^{-1} . The Ragone plots (c) and (d) capacity retentions of C_3-7, C_2-8, C_1-9, CS-PVP, and CS-PAN.

4.2.3.3 Electrochemical impedance spectroscopy (EIS) measurement

EIS experiment was performed in the frequency range of 0.1 Hz to 100 kHz at amplitude of 0.1 V to understand more about electrochemical performance of all samples. EIS data are generally presented as a Nyquist plot which is the plot of imaginary part ($-Z''$) versus the real part (Z'). As exposed in Figure 4.15(a), there were three regions to be considered in Nyquist plot including high frequency region, mid-frequency region, and low frequency region. In the high frequency region, the intercept of the real axis indicated the bulk resistance (R_s), which was the total resistance of pore-electrolyte resistance, bulk resistance, and a contact resistance causing by the electrode and current collector surface (X. He *et al.*, 2017). By fitting the semicircles of the measured data, the R_s values of C_3-7, C_2-8, C_1-9, CS-PVP, and CS-PAN were estimated to be 553.39 m Ω , 556.45 m Ω , 791.04 m Ω , 726.26 m Ω , and 887.14 m Ω , respectively. At the middle frequency, the diameter of semicircle corresponded to the charge transfer resistance (R_{ct}), which was caused by Faradaic reaction (Xiao *et al.*, 2017). As seen in Figure 4.15(b), some big-diameter semicircles were observed at this region, which interpreted that all electrodes exhibited little characteristics of Faradaic reaction. Last, in the low frequency region, almost straight lines with an angle about 20° along the vertical axis were observed for C_2-8 and wider angle was observed for other samples. The slopes of the curves corresponded the Warburg impedances, which represented the electrolyte diffusion in the electrode material (Sun *et al.*, 2017). It was noticed that the C_2-8 electrode showed the smaller vertical slope compared with the vertical axis, which indicated that this electrode materials had lower Warburg impedance than the other electrodes. The value of R_{ct} , R_s , and n values of all samples were displayed in Table 4.4.

Table 4.4 The values of R_s and R_{ct} of C_3-7, C_2-8, C_1-9, CS-PVP, and CS-PAN.

Sample	R_s [m Ω]	R_{ct} [m Ω]	n value
C_3-7	553.39	66.37	0.99451
C_2-8	556.45	196.82	0.99673
C_1-9	791.04	183.25	0.99665
CS-PVP	726.26	330.54	0.99439
CS-PAN	887.14	215.82	0.99529



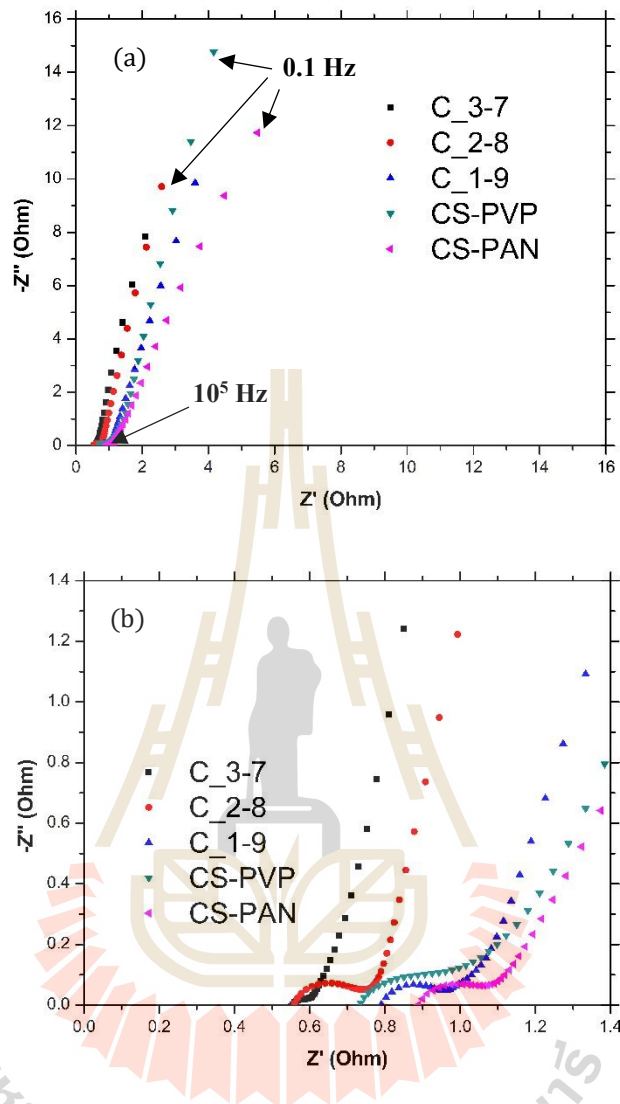


Figure 4.15 The Nyquist plot (a) and (b) enlargement of Nyquist plot of C_3-7, C_2-8, C_1-9, CS-PVP, and CS-PAN.

4.3 Carbon-manganese oxide composite nanofibers (C-MnO_x)

4.3.1 Structure and morphology characterization

4.3.1.1 Thermogravimetric analysis (TGA) of PAN-Mn₁₀₋₈, PAN-Mn₁₀₋₉, and PAN-Mn₁₀₋₁₀

Figure 4.15(b) displayed the DSC curves of all samples, which the experiments were measured under the nitrogen atmosphere with the flow rate of 100 ml min⁻¹, the heating rate of 10°C min⁻¹, and the temperature range from 35°C to 1000°C. The as-spun C-Mn₁₀₋₈, C-Mn₁₀₋₉, C-Mn₁₀₋₁₀ appeared at about 268°C, 269°C, and 242°C, respectively. The peak shift observing in the as-spun C-Mn₁₀₋₈ implied that the embedding of Mn(NO₃)₂ enhanced the cyclization reaction of nitrile groups resulting in a lower decomposition temperature.

The weight losses of all samples were determined by the study of TGA analysis. In general, for as-spun composite PAN nanofibers, the degradation occurred through three main steps. The first step in region (I) was related to the removal of humidity at below 100°C. Second in region (II), at the temperature about 200-300°C, the weight loss was related to the infusible ladder polymer forming before carbonization. The last step in region (III) was related to the pyrolysis of the polymer structure of the fibers at the temperature about 400–600°C (Yoo *et al.*, 2017). As displayed in Figure 4.16(b), the weight losses of the as-spun samples started above 268 °C, maximized at about 400°C and occurred continuously until the temperature of 1000°C. The total weight loss was measured about 81%, 87%, and 78% for the as spun C-Mn₁₀₋₈, C-Mn₁₀₋₉, and C-Mn₁₀₋₁₀, respectively, at 1000°C.

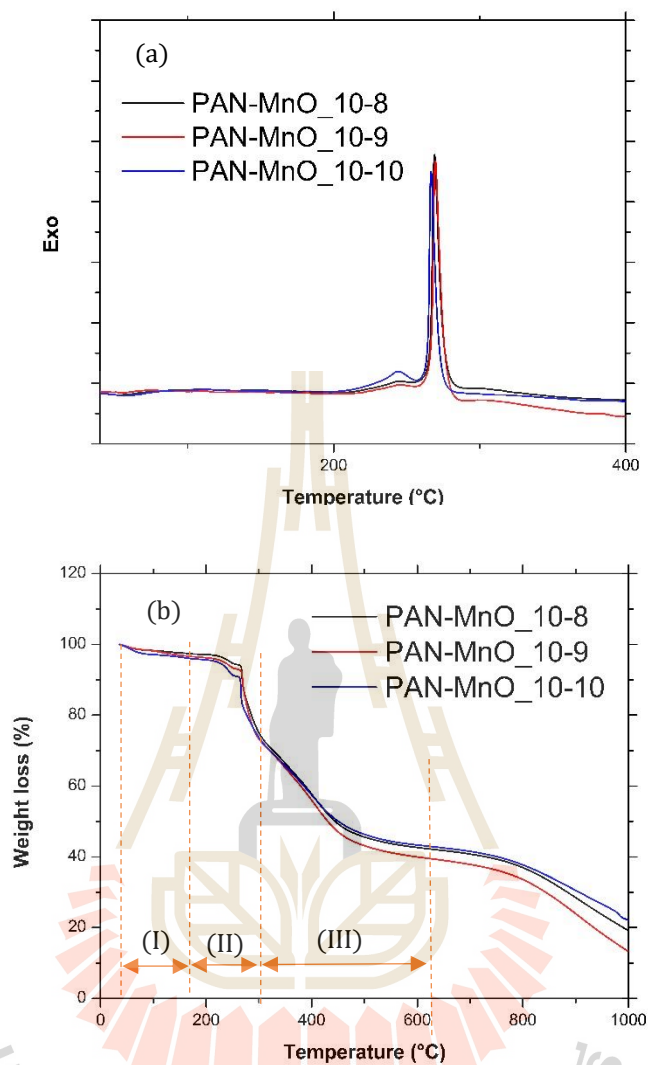


Figure 4.16 The DSC (a) and TGA (b) of PAN-MnO₁₀₋₈, PAN-MnO₁₀₋₉, and PAN-MnO₁₀₋₁₀.

4.3.1.2 X-ray diffraction (XRD) measurement of C-Mn₁₀₋₈, C-Mn₁₀₋₉, and C-Mn₁₀₋₁₀

Figure 4.17 displayed the XRD patterns of all samples measured by Cu K α with wavelength of 1.54 Å between 2 θ from 10° to 80°, step size 0.02 and step time 0.2. In general, the broad-peak patterns show the characteristic of amorphous carbon in the sample, which occur at around 10–12°, 27–29°, and 43–44° (Jingjing Ding *et al.*, 2018). The sharp peaks of hexagonal graphite appeared in the samples at the values of 2 θ of about 26° and 42°, which were corresponding to the plane (002) and (100) with the d-spacing value of 3.37 and 2.13 Å, respectively (JCPDS card No. 12-0212). The broad peaks around 14°, which were the peaks of plane (002) with the d-spacing value of 6.18 Å were the peak of hexagonal-diamond carbon observed clearly in C-Mn₁₀₋₈ and C-Mn₁₀₋₉ (JCPDS card No. 79-1470). The sharp peaks of manganese oxide (MnO) were observed clearly in the sample C-Mn₁₀₋₁₀ at the two-theta of 35, 40, 58, 69, and 73°, which correspond to the plane (111), (200), (220), (311), and (222) with the d-spacing values of 2.58, 2.23, 1.58, 1.34, 1.29, and 1.11 Å, respectively (JCPDS card No. 72-1533). The results showed the multi-phase composition of carbon phase and manganese oxide phase, which were consistent with the SEM result. Each phase had different advantage for electrochemical properties i.e. the carbon phase was excellent for EDLCs behavior and manganese oxide phase was excellent for pseudocapacitive behavior, which will be discussed in details in the following section.

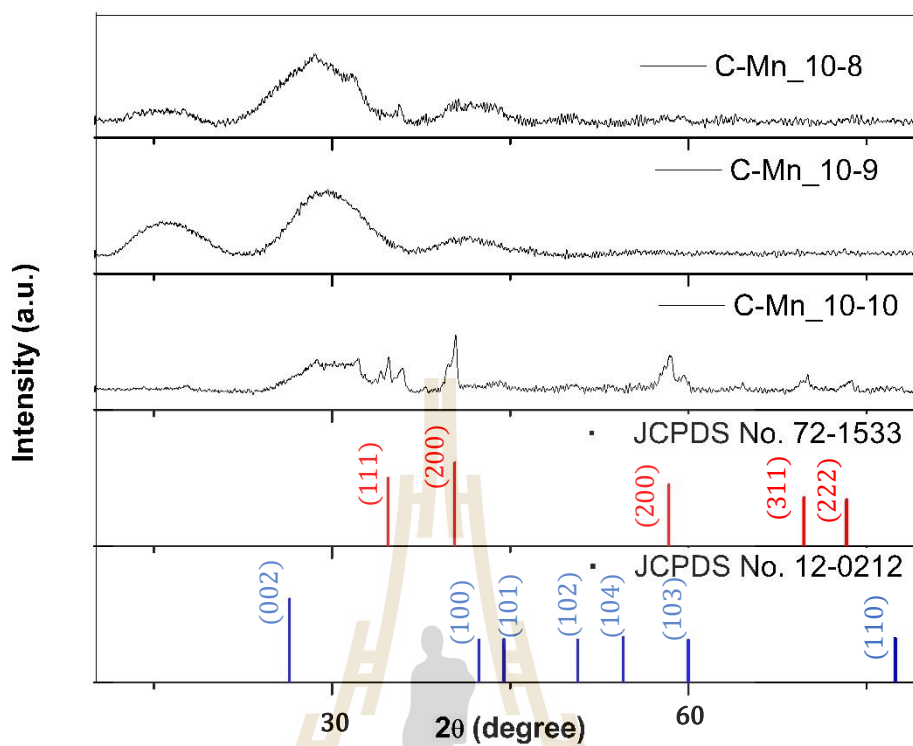


Figure 4.17 The XRD spectra of C-Mn_10-8, C-Mn_10-9, and C-Mn_10-10.

4.3.1.3 Raman spectroscopy analysis of C-Mn₁₀₋₈, C-Mn₁₀₋₉, and C-Mn₁₀₋₁₀

The Raman analysis was used to determine the carbon quality of all samples with the wave number in the range between 500 and 3500 cm^{-1} . By using a Lorentzian multi-peaks fitting the band positions were observed (Carotenuto *et al.*, 2016). As presented in Figure 4.18, there were two main peaks $\sim 1330\text{-}1346 \text{ cm}^{-1}$ (D-Band) and $\sim 1582\text{-}1596 \text{ cm}^{-1}$ (G-Band) occurred in the curves of all samples, which related to the scattering on disordered amorphous carbon cluster (sp^3 bonded carbon atoms) and the stretching of C-C bonds in the hexagonal ring of graphite structure (sp^2 bonded carbon atom) (H. Chen *et al.*, 2014). Another peak was observed around 2704 cm^{-1} (G'-band, which was a two-phonon band taken to be $2 \times 1352 \text{ cm}^{-1}$) (Yan *et al.*, 2014). The biggest I_D/I_G ratio of 1.00 for C-Mn₁₀₋₈ was obtained from the fitting, which implied that this sample had the phase of amorphous structures. On the other hand, the smaller I_D/I_G ratio of 0.98 for C-Mn₁₀₋₉ and C-Mn₁₀₋₁₀ showed the high graphite structure in the fibers.

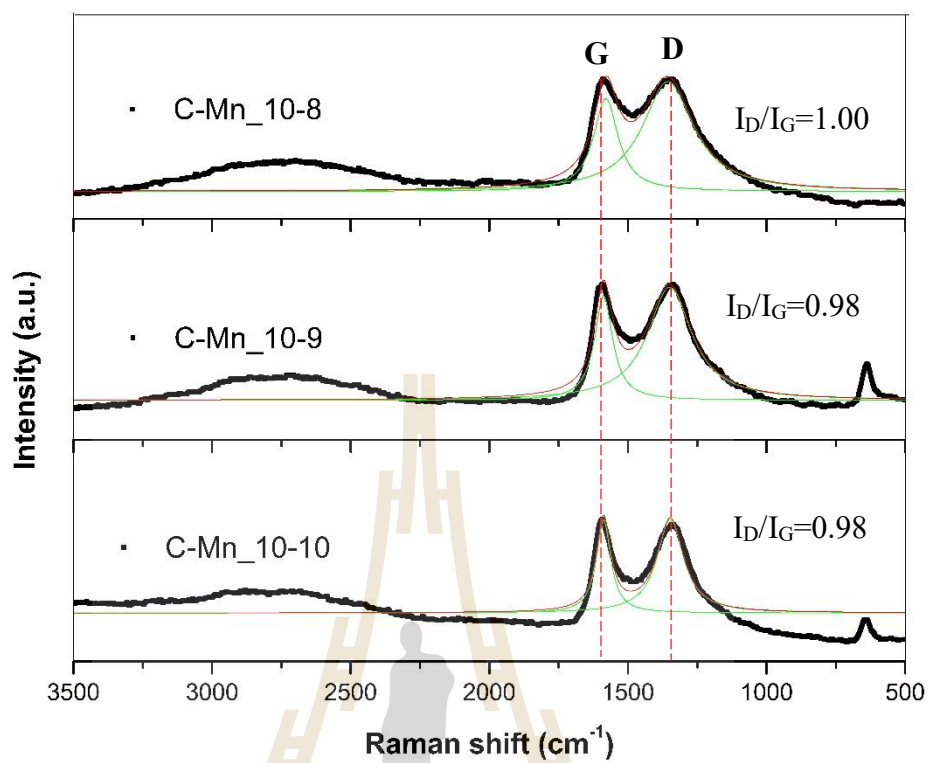


Figure 4.18 The Raman spectra of C-Mn_10-8, C-Mn_10-9, and C-Mn_10-10.

4.3.1.4 Scanning electron microscopy (SEM) analysis of C-Mn₁₀₋₈, C-Mn₁₀₋₉, and C-Mn₁₀₋₁₀

Figure 4.19(a), (b), and (c) exposed the FE-SEM of C-Mn₁₀₋₈, C-Mn₁₀₋₉, and C-Mn₁₀₋₁₀, respectively, at the magnifications of 50 kX, which exhibited a few rough surfaces of long uniform and randomly arranged nanofibers. None of the interconnected fibers were observed in these cases. The average fiber diameter of these samples decreases in the range of about 228 nm and 308 nm where C-Mn₁₀₋₁₀ had the smallest average diameter. The changes of diameter sizes in composite nanofibers were caused by different net charged density and the repulsive force created by the metallic precursor embedding in the fibers (Tavanai *et al.*, 2009). In addition to these, the manganese oxide nanoparticles had the average sizes in the range of about 28-54 nm with the shape of sphere. The average sizes of particles and average diameters of all samples were summarized in table 1.

To ensure the core-shell structures of carbon nanofibers and manganese oxides nanoparticle the fibers-cross-sectional images were performed by FE-SEM. As revealed in Figure 4.20(a), the cross-sectional image of C-Mn₁₀₋₈ revealed the core-shell structure of the fibers, which the manganese oxide nanoparticles stayed on the outside surface of the carbon nanofibers. Plus, the enlargement of this image was performed as shown in Figure 4.20(b) to exhibit that there was no particle staying on the inside of the fibers. Another image was taken for C-Mn₁₀₋₈ as exposed in Figure 4.20(c) to provide more evidence that there was absolutely no particle inside the fibers. Figure 4.20(d) displayed the image of C-Mn₁₀₋₉, which exhibited that the manganese oxide nanoparticles were outside on the surface of the fiber. Similar to the two samples above, Figure 4.20(f) indicated the image of cross-sectional fibers, which illustrated

manganese oxide nanoparticles sit outside on the surface of fibers, and Figure 4.20(f), which is the enlargement of image of C-Mn_10-10, conformed absence of manganese oxide nanoparticle on the cross section of the fibers.

Table 4.5 Average diameters of all nanofibers and particle size of MnO_x embedded in nanofibers.

Sample	Fiber size (nm)	Particle size (nm)
C-Mn_10-8	308 ±30	54±07
C-Mn_10-9	293±22	46±06
C-Mn_10-10	228±30	28±03

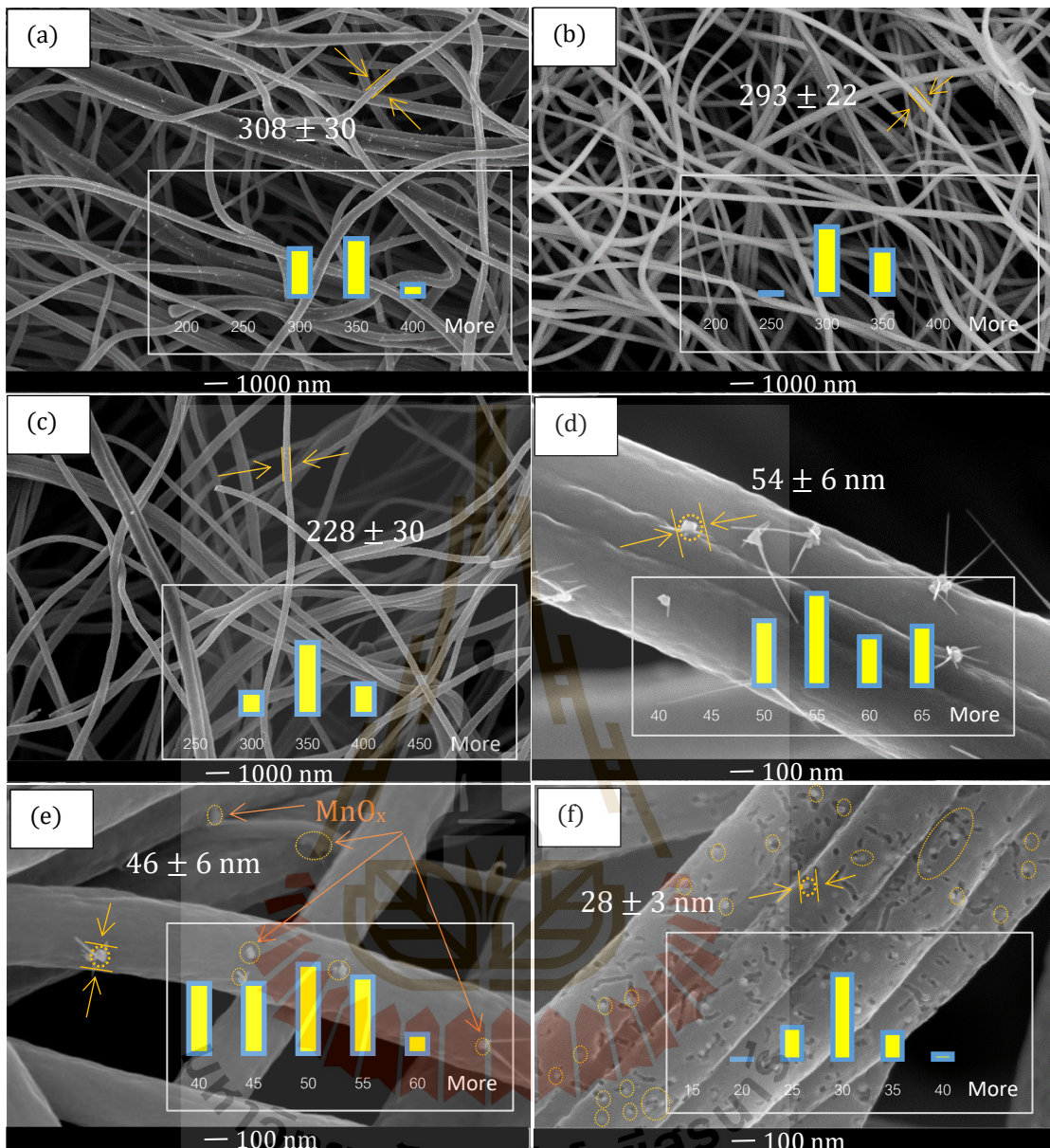


Figure 4.19 The FE-SEM of (a) C-Mn_10-8, (b) C-Mn_10-9, and (c) C-Mn_10-10 at the magnification of 5 kX and (d) C-Mn_10-8, (e) C-Mn_10-9, and C-Mn_10-10 at the magnification of 50 kX.

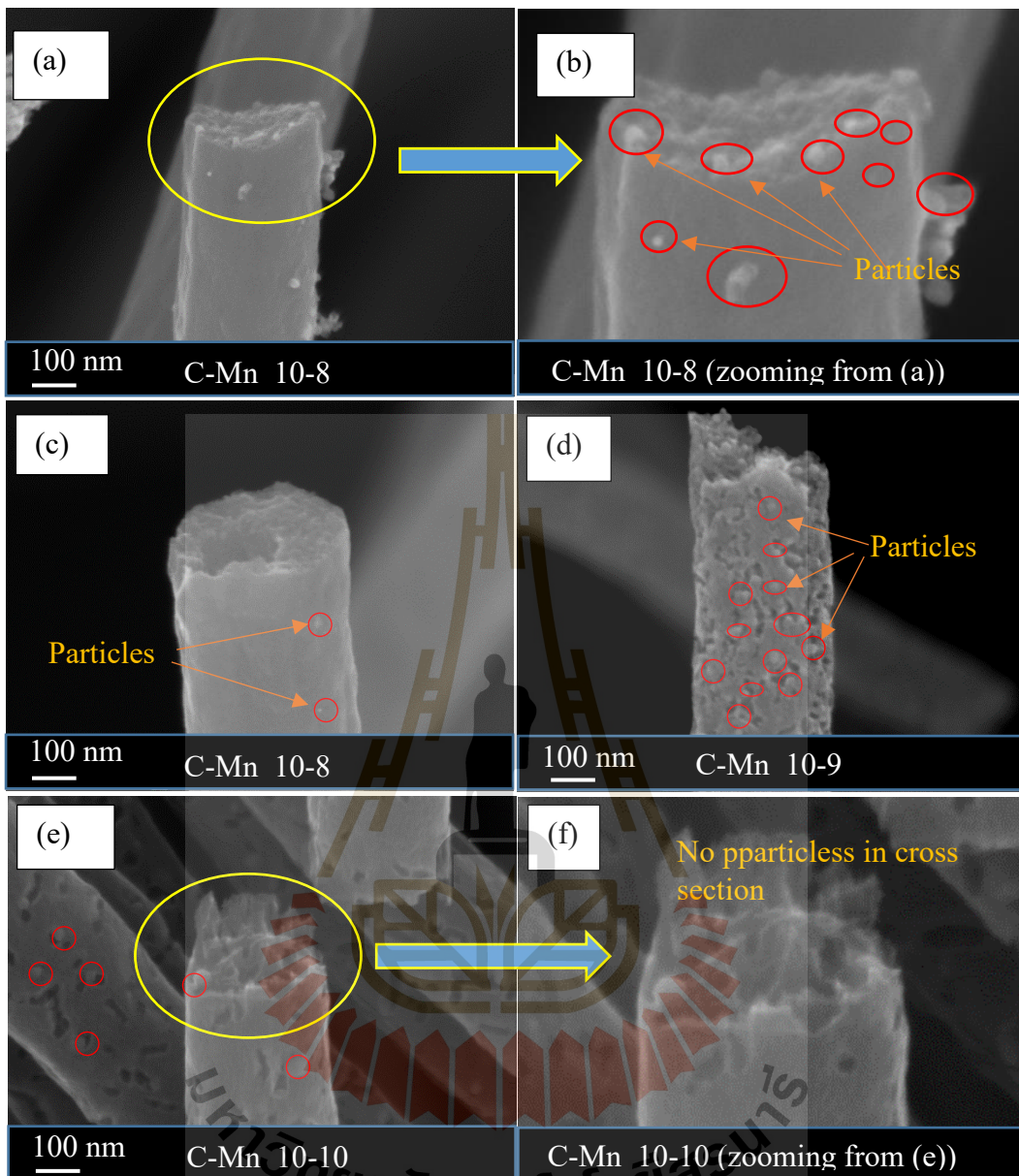


Figure 4.20 The FE-SEM images of cross-sectional fibers of (a) and (c) C-Mn₁₀₋₈, (b) the enlargement of C-Mn₁₀₋₈, (d) C-Mn₁₀₋₉, (e) C-Mn₁₀₋₁₀, and (f) the enlargement of C-Mn₁₀₋₁₀.

4.3.1.5 N₂-adsorption/desorption analysis of C-Mn₁₀₋₈

The pore character and specific area of all calcined samples were determined by measuring N₂ adsorption/desorption. Generally, the pore can be classified into three groups depending on the size of the pore which are micropores, mesopores, and macropores in the range of less than 2 nm, from 2 to 50 nm, and bigger than 50 nm, respectively (P. B. Balbuena, and Gubbins, K. E. , 1993). Figure 4.21(a) displayed the isotherm curves of the C-Mn₁₀₋₈, which displayed small hysteresis loops, which typically are type-IV isotherm and parts of type-II isotherm which are mesopores and macropores, respectively. For type-II and type-IV isotherm, the interaction between sample surface and adsorbate are relatively strong. The pore size distributions of the samples were obtained by using MP and BJH for micropores and mesoporous, respectively, which were shown in Figure 4.21(b). C-Mn₁₀₋₈ had mesopores and macropores with average sizes of about 3 nm, the specific area about 701 m² g⁻¹, and the average volume of about 161 cm³ g⁻¹, which the results were consistent with the above FE-SEM results. The large specific surface areas were very useful for providing many electrochemical reaction sites for electrolyte ions to obtain high electrochemical performance, which were consistent with the electrochemical property results, which we will discuss.

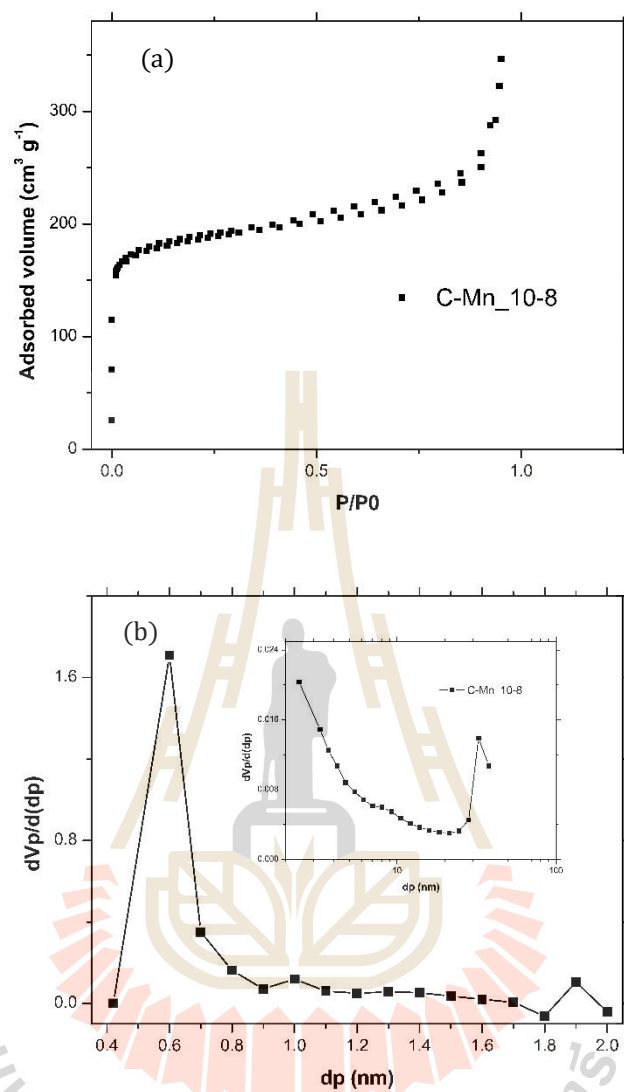
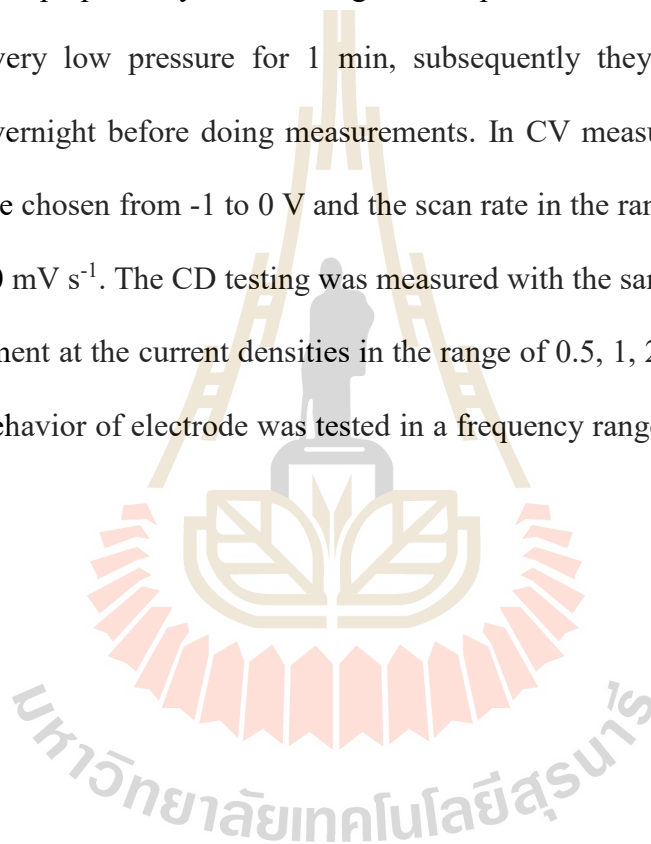


Figure 4.21 The isotherm curve (a), MP plot (b), and BJH (inset (b)) of C-Mn₁₀₋₈.

4.3.2 Electrochemical properties of C-Mn_10-8, C-Mn-10-9, C-Mn_10-10

The electrochemical properties of C-Mn_10-8, C-Mn-10-9, C-Mn_10-10 were studied by the cyclic voltammetry (CV), galvanostatic charge/discharge (GCD), and electrochemical impedance spectroscopy (EIS). The experiments were conducted in the three-electrode configuration system in 6 M KOH aqueous electrolyte. The working electrodes were prepared by sandwiching the samples between the nickel foams and pressing at very low pressure for 1 min, subsequently they were soaked in the electrolyte overnight before doing measurements. In CV measurement, the potential windows were chosen from -1 to 0 V and the scan rate in the range of 2, 5, 10, 20, 50, 100, 200, 500 mV s⁻¹. The CD testing was measured with the same voltage window as CV measurement at the current densities in the range of 0.5, 1, 2, 5, and 10 A g⁻¹. The impedance behavior of electrode was tested in a frequency range between 0.1 and 10⁵ Hz.



4.3.2.1 Cyclic voltammetry (CV) analysis

The capacitive behaviors of the electrodes were determined by plotting the CV curve at 500 mV s⁻¹ and 2 mV s⁻¹. As presented in Figure 4.22(a), at high scan rate of 500 mV s⁻¹, the curves of all samples behaved nearly as a rectangular curve of an ideal capacitor without any redox peaks, which indicated that the double layer capacitive processes mainly stored the charges of the electrode. At this scan rate, the CV-curve loop of C-Mn_10-10 had the biggest loop, which implied that this sample had the greatest specific capacitance at this scan rate. Figure 4.22(b) displayed the CV curves of the samples at the scan rate of 5 mV s⁻¹, which also behaved nearly as a rectangular curve. Moreover, the redox peaks of manganese oxide nanoparticles were observed for all samples. The oxidation-reaction peaks occurred around the potentials of -0.5 V and -0.6 V for manganese oxide changing its oxidation state from Mn²⁺ to Mn³⁺ and from Mn³⁺ to Mn⁴⁺, respectively, while the reduction-reaction peaks occurred around the potential of -0.5 V represented the changing of oxidation states for Mn⁴⁺ to Mn³⁺ or/and Mn²⁺ (Sinprachim *et al.*, 2016). It is noteworthy that the samples started to display resistive behaviors at the operating potential -0.1 V, which is the cathodic current from the decomposition of the aqueous electrolyte (L. Chen *et al.*, 2013). This phenomena indicated over potential region that implies the limitation of CNF. For this scan rate, the CV-curve loop of C-Mn_10-8 had the biggest loop comparing to other samples, which suggested that this sample had the greatest specific capacitance at this scan rate. Figure 4.22(c) exhibited the plots of specific capacitances of the samples versus scan rates. As the scan rate increased, the specific capacitances of the samples also increased with the scan rate from 2 to 20 mV s⁻¹, then reached a maximum value between 20 and 50 mV s⁻¹ and the decrease of specific capacitances were found above

100 mV s⁻¹ indicating the diffusion of electrolyte ions was limited due to the time constraint and only the outer surface provided charge accumulation (S.-J. Park *et al.*, 2012; Pech *et al.*, 2010). Moreover, this limitation was possibly proposed as the double layer growth and blocked the ions before they accessed the full region in the micropore.



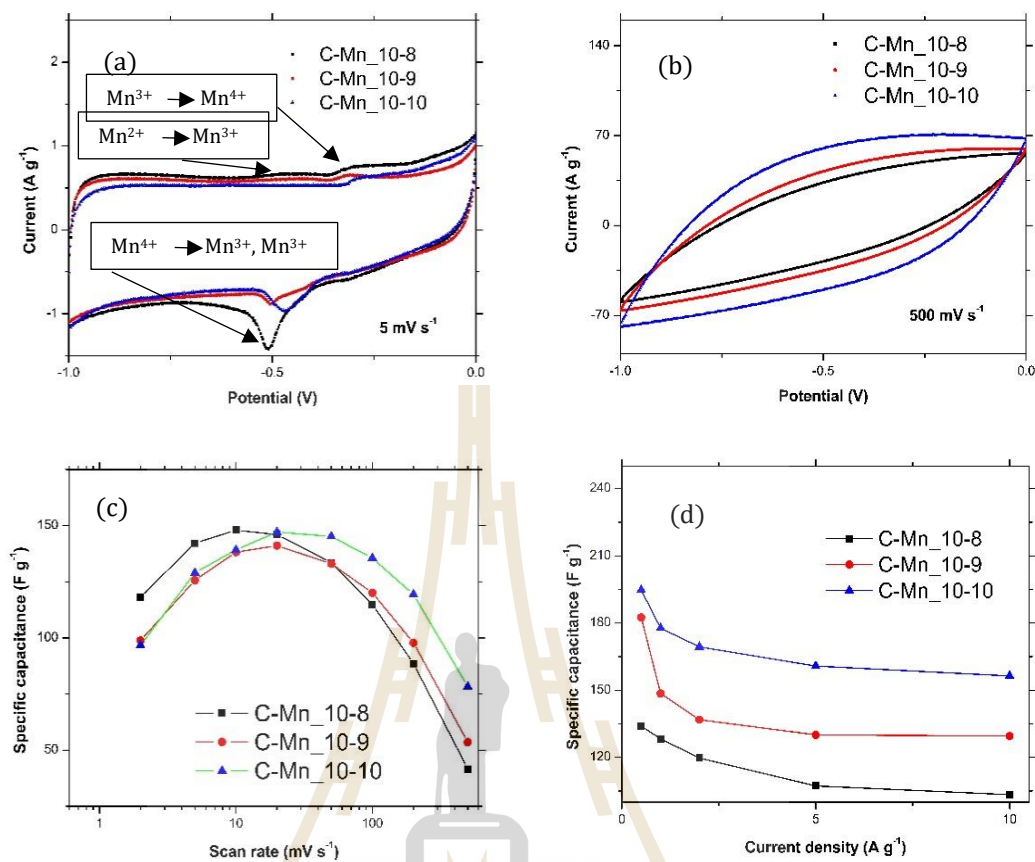


Figure 4.22 The CV curves at the scan rate of (a) 5 mV s^{-1} and (b) 500 mV s^{-1} ; (c) the plots of specific capacitances versus scan rate, and (d) the plots of specific capacitances versus current density of the samples.

4.3.2.2 Galvanostatic charge/discharge (GDC) analysis

The linear voltage-time profile of GCD measurement of both samples at the current density of 10 A g^{-1} and 0.5 A g^{-1} were revealed by Figure 4.23(a) and (b), respectively. At both current densities, C-Mn₁₀₋₁₀ had the long discharge curves, which, generally, the longest discharge time represents the greatest specific capacitance. Figure 4.22(d) displayed that the specific capacitances of all samples decreased with an increasing of current density. It is worth noted that C-Mn₁₀₋₁₀ had the great specific capacitances for all current densities. A comparison of power and energy densities of all electrodes is represented by the well-known Ragone plot as in Figure 4.23(c). Concerning the energy density, the C-Mn₁₀₋₁₀ electrode was considered as the greatest electrode which can store maximum energy of $\sim 27 \text{ mW h g}^{-1}$ at a high power density of $\sim 249 \text{ mW g}^{-1}$. In addition, the C-Mn₁₀₋₁₀ had the maximum power density of 4846 mW g^{-1} at the energy density of $\sim 17 \text{ mW h g}^{-1}$, which demonstrated faster charging/discharging. As shown in Figure 4.23(d), the capacitance retention of all samples was great, which remained $\sim 95\%$ except C-Mn₁₀₋₁₀, which remained $\sim 97\%$ after 1000 cycles.

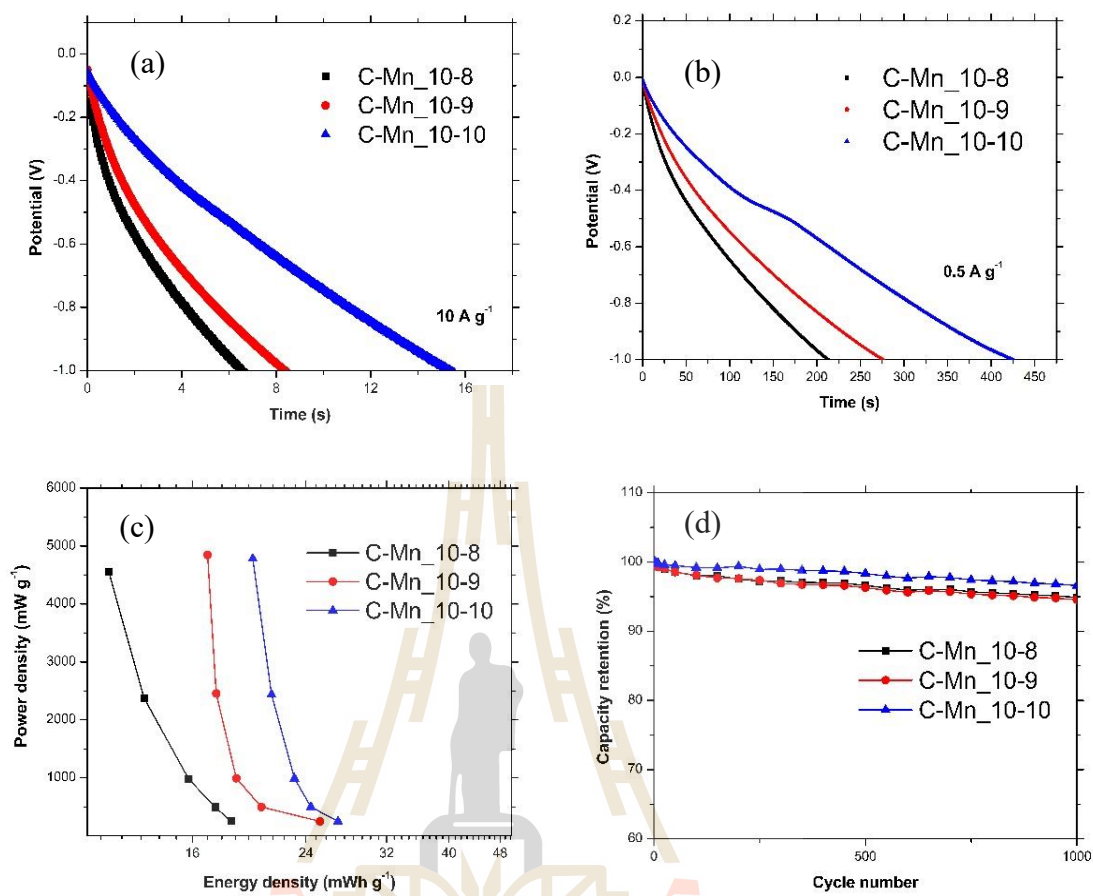


Figure 4.23 The CD curves at the current density of (a) 10 A g^{-1} and (b) 0.5 A g^{-1} ; (c) the Ragone plots and (d) capacity retention.

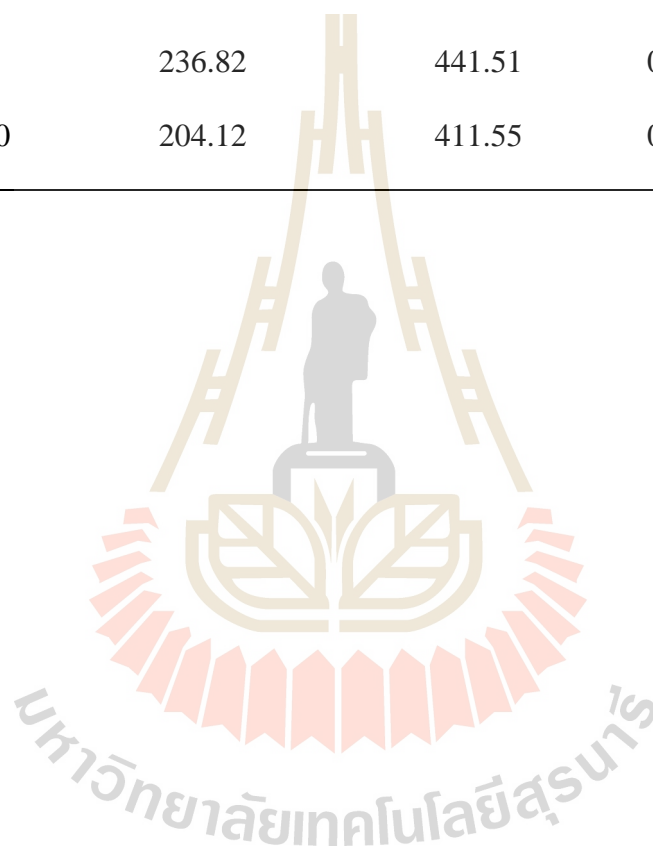
4.2.2.3 Electrochemical impedance spectroscopy (EIS) measurement

EIS experiment was performed in the frequency range of 0.1 Hz to 100 kHz at amplitude of 0.1 V to understand more about electrochemical performance of all samples. EIS data are generally presented as a Nyquist plot which is a plot of imaginary part ($-Z''$) versus the real part (Z'). As displayed in Figure 4.24(a), there were three regions to be considered in Nyquist plot including high frequency region, mid-frequency region, and low frequency region. In the high frequency region, the intercept of the real axis indicated the bulk resistance (R_s), which was the total resistance of pore-electrolyte resistance, bulk resistance, and a contact resistance causing by the electrode and current collector surface (X. He *et al.*, 2017). By fitting the semicircles of the measured data, the series resistances (R_s) and charge transfer resistances of C-Mn_10-8, C-Mn_10-9, and C-Mn_10-10 were estimated. In comparison, C-Mn_10-8 showed the smallest value R_s of 282.14 m Ω . At the middle frequency, the diameter of semicircle corresponded to the charge transfer resistance (R_{ct}) which was caused by Faradaic reaction (Xiao *et al.*, 2017). As seen in Figure 4.24(b), some big-diameter semicircles were observed at this region, which interpreted that all electrodes exhibited little characteristics of Faradaic reaction. By fitting the measured data, the R_{ct} of C-Mn_10-10 showed the smallest value of 204.12 m Ω . Last, in the low frequency region, almost straight lines with an angle about 20° along the vertical axis were observed for C-Mn_10-10 and wider angle was observed for other samples. The slopes of the curves corresponded the Warburg impedances which represented the electrolyte diffusion in the electrode material (Sun *et al.*, 2017). It was noticed that the C-Mn_10-10 electrode showed the smaller vertical slope compared with the vertical axis, which indicated that

this electrode materials had lower Warburg impedance than the other electrodes. The value of R_{ct} , R_s , and N values of all samples were displayed in Table 4.6.

Table 4.6 The values of charge transfer resistances, equivalent series resistances, and N values of the samples.

Sample	R_{ct} (m Ω)	R_s (m Ω)	N value
C-Mn_10-8	316.4	282.14	0.99283
C-Mn_10-9	236.82	441.51	0.99558
C-Mn_10-10	204.12	411.55	0.99568



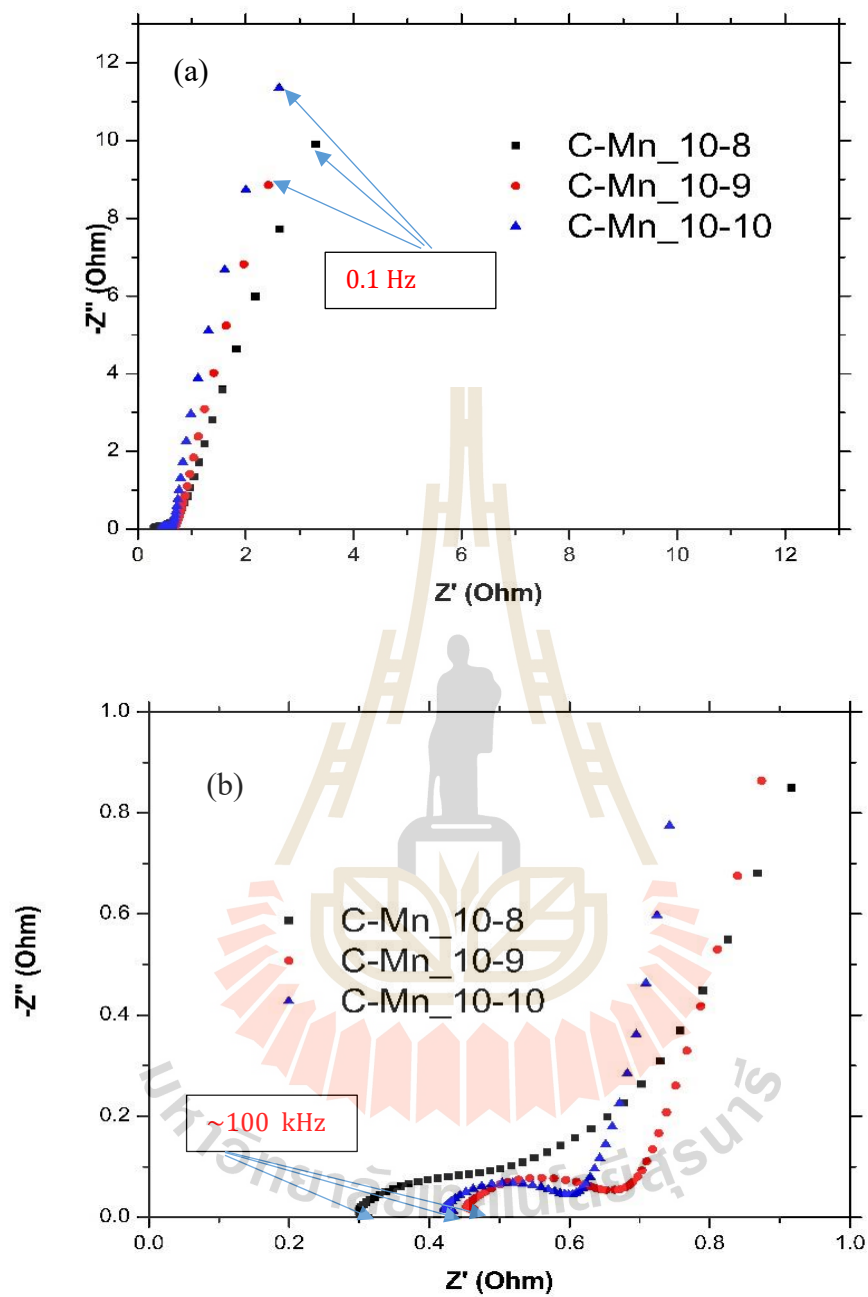


Figure 4.24 The Nyquist plot (a) and enlargement of Nyquist plot (b) of all samples.

CHAPTER V

CONCLUSIONS AND SUGGESTIONS

In this study, carbon nanofibers (CNF), porous carbon nanofibers (P-CNF), interconnected carbon nanofibers (IC-CNF), and carbon-manganese oxide core-shell composite nanofibers were successfully fabricated by a single-nozzle and core-shell electrospinning technique followed by carbonization and CO₂-activation process. The thermal properties of the as spun samples were studied by Thermogravimetric analyzer (TGA). The structures and morphologies of all the samples were characterized by XRD, SEM, Raman, and Gas absorption techniques. The electrochemical properties were studied by CV, GCD and EIS techniques. The conclusion were made on the samples, which could be classified into three sections related to the types of the samples including (i) carbon nanofibers (CNF) and porous carbon nanofibers (P-CNF), (ii) interconnected carbon nanofibers (IC-CNF), and (iii) carbon/manganese oxide core-shell composite nanofibers (C/MnO_x). The conclusions based on the experimental results for each group and all samples were summarized as follows:

5.1 The structure and morphology characterization

The XRD patterns of all samples showed the phases of amorphous carbon and hexagonal graphite (JCPDS card No. 12-0212). In addition to these phases, C/MnO_x displayed the patterns of manganese oxide (Mn²⁺ and Mn³⁺) (JCPDS card No. 72-1533).

For sample in IC-CNF group, the sample C_3-7, C_2-8, and C_1-9 revealed the highest graphite structures based on the Raman analysis with I_D/I_G -value of 0.97. One of core-shell blends, CS-PAN had higher graphite structure based on the Raman analysis with the I_D/I_G -value of 0.98. Among all samples in C/MnO_x group, C-Mn_10-9 and C-Mn_10-10 illustrated the higher graphite structure based on the Raman analysis with the I_D/I_G -value of 0.98 where C-Mn_10-8 had I_D/I_G -value of 1.00. Therefore, the carbon nanofibers getting from the PVP-PAN blend showed the highest graphite structure.

Concerning the morphology, CNF based on gas adsorption/desorption technique possessed the characteristic of non-porous structure where P-CNF had the characteristic of microporous and mesoporous structure with the higher specific area of $677 \text{ m}^2 \text{ g}^{-1}$ and smaller pore diameter of 1.86 nm. Among the samples made from PVP-PAN blends, C_3-7 illustrated the highest specific area of $1206 \text{ m}^2 \text{ g}^{-1}$ with the characteristic of macropores with the average diameter of 52.98 nm. However, in the samples made from core-shell solution, CS-PVP contained the higher specific area of $581 \text{ m}^2 \text{ g}^{-1}$ with average diameter of 1.9 nm. In the last group, C-Mn_10-8 showed the characteristic of mesopore and macropore with the specific surface area of $701 \text{ m}^2 \text{ g}^{-1}$ with the average diameter of 3 nm. The CNF had the biggest average diameter of $412 \pm 27 \text{ nm}$ while the mixture of PVP in the precursor solution could decrease the average diameter of the fibers. For instance, C_2-8 had the smallest average diameter of $188 \pm 13 \text{ nm}$ among CNF derived from PVP-PAN blend. Moreover, the decreases of average diameters were also observed in the CS-PVP and CS-PAN. For example, CS-PVP exhibited the smaller average diameter of $237 \pm 33 \text{ nm}$. It is worth noted that only CNF fabricated by core-shell electrospinning technique followed by carbonization process displayed the structure of fiber-fiber interconnection. In summary, the presence of PVP

in the precursor solution could decrease the average diameter of the fibers, and the fibers obtained from the PVP-PAN blend did not show the fiber-fibers structure. In the C-MnO_x composite group, the decreases of average diameters were also observed. Thus, the smallest average diameter of 228 ± 30 nm was observed in C-Mn_10-10. In additions, this sample also presented the smallest average particle size of 28 ± 03 nm. The core-shell structures of CNF and manganese oxide nanoparticles were exposed by the cross-sectional image of the fibers. In conclusion, the change of PAN concentration of the shell solution could vary the average diameter and particle sizes, i.e. the higher concentration, the bigger average diameter or particle size.

5.2 The electrochemical properties

The summary of the effects of charge storage mechanism, specific capacitance, and energy density on electrochemical properties of CNF, P-CNF, IC-CNF, and C-MnO_x composite nanofiber were presented in this section. There are two main types of charge storage mechanism: (i) the electric double layer capacitors (EDLCs) and (ii) the pseudocapacitive behavior. It was observed that the carbon-based nanofibers stored energy via the accumulation of charge at the electrode-electrolyte interface while the manganese oxide nanoparticle stored energy via redox reaction. The redox reaction of manganese oxide nanoparticles was studied by the CV technique in the 6 M KOH aqueous electrolyte with the potential window between -1 V and 0 V at the scan rates from 2 to 500 mV s⁻¹. The study revealed that all MnO_x-based samples displayed the pseudocapacitive behaviors. The redox peaks observed in the CV curves were caused by the redox transition of the nanoparticle between different valence states. The rapid and faradic reactions on the electrode-electrolyte electrode were the main causes of the

specific capacitances of the pseudoelectrodes. There were no redox peaks in the CV curves of CNF, C_3-7, C_2-8, C_1-9, CS-PVP, and CS-PAN. Hence, these samples exhibited the EDLCs behaviors. However, the C-Mn_10-8, C-Mn_10-9, and C-Mn_10-10 displayed the oxidation-reaction peaks occurred around the potentials of -0.5 V and -0.6 V for manganese oxide changing its oxidation states from Mn^{+2} to Mn^{3+} and from Mn^{3+} to Mn^{4+} , respectively. Alternatively, the reduction-reaction peaks occurred around the potential of -0.5 V represented the change of oxidation states for Mn^{4+} to Mn^{3+} or/and Mn^{2+} .

For the specific capacitances of all samples were calculated from the discharging curves. Among carbon-based samples, excluding MnO_x , C_1-9 exhibited the highest specific capacitance of 180 F g^{-1} at the current density of 0.5 A g^{-1} . Besides, all MnO_x -composite nanofibers exhibited the higher specific capacitances than the pure carbon-based samples. For instance, C-Mn_10-10 presented the highest specific capacitance of 214 F g^{-1} at the current density of 0.5 A g^{-1} . This suggested that the composite both carbon materials and pseudo materials provided better electrochemical performance. This improvement was the cause of the combination of EDLCs and pseudo behaviors of CNF and MnO_x nanoparticles. Particularly, EDLCs materials could provide high power density due to the good conductivity and high surface area while pseudomaterials could provide higher energy densities. Therefore, the synergistic effect between Carbon and pseudomaterials could maximize the use of individual benefit to reach the excellent electrochemical properties. All samples revealed the great cycle stability of more than 90 % after 1000 cycles. For example, the specific capacitance of C-Mn_10-10 remained ~97% after 1000 cycles, and P-CNF remained ~99% after 1000 cycles. This excellent cycle stability was caused by the charge storage mechanism of

carbon materials which stored the energy by the accumulation of ions at the electrolyte-electrode interface. This mechanism could prevent the electrode from the changing of pore volume during charging/discharging process.

Finally, the energy density of all samples were calculated at the current density of 0.5 A g^{-1} and compared with the CNF. As a result, all samples had lower energy densities than CNF except C-Mn₁₀₋₁₀. For instance, the extremely decrease was observed in P-CNF and C-Mn₁₀₋₈ about 27% and 29%, respectively. In addition, the tiny decreases were observed in C₃₋₇, C₂₋₈, C₁₋₉, CS-PVP, CS-PAN, and C-Mn₁₀₋₉ about 2, 9, 5, 10, 8, 3, and 4%, respectively. In contrast, the increase was observed in C-Mn₁₀₋₁₀ about 4%. These results suggested that the micropores in P-CNF could not enhance the energy density. Moreover, the presence of PVP content in the precursor solutions did not improve the energy density. However, the presence of manganese oxide nanoparticles in the CNF could increase the energy density based on the synergistic effect of EDLCs and pseudocapacitive behaviors.

5.3 Suggestions

Further works should be done to improve and clarify the structure and mechanism of electrochemical reaction by the following:

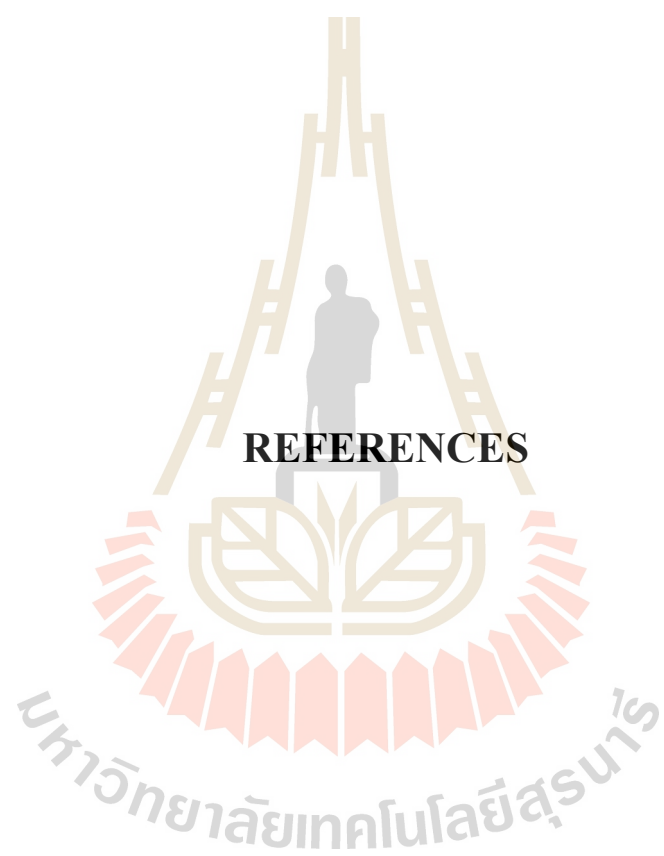
(1) The TEM technique should be used to explore the manganese oxide nanoparticles in the carbon nanofibers.

(2) The oxidation state of the manganese oxide should be studied by XANE technique.

(3) Investigation of atomic/electronic structure, such as the change of redox valence of the C-MnO_x electrodes using *in situ* X-ray absorption spectroscopy (XAS) during the charging/discharging process is important to understand in more details.

(4) The fitting between the Nyquist plot and the equivalent circuit could provide more information about the electrode including the Warburg impedance.





REFERENCES

REFERENCES

- Abdal-hay, A., Abbasi, N., Gwiazda, M., Hamlet, S., and Ivanovski, S. (2018). Novel polycaprolactone/hydroxyapatite nanocomposite fibrous scaffolds by direct melt-electrospinning writing. **European Polymer Journal**. 105: 257-264.
- Abdelkareem, M. A., Allagui, A., Sayed, E. T., El Haj Assad, M., Said, Z., and Elsaid, K. (2019). Comparative analysis of liquid versus vapor-feed passive direct methanol fuel cells. **Renewable Energy**. 131: 563-584.
- Agyemang, F. O., Tomboc, G. M., Kwofie, S., and Kim, H. (2018). Electrospun carbon nanofiber-carbon nanotubes coated polyaniline composites with improved electrochemical properties for supercapacitors. **Electrochimica Acta**. 259: 1110-1119.
- Ahn, M. S., Ahmad, R., Yoo, J. Y., and Hahn, Y. B. (2018). Synthesis of manganese oxide nanorods and its application for potassium ion sensing in water. **Journal of Colloid Interface Science**. 516: 364-370.
- Ahuja, P., Ujjain, S. K., and Kanojia, R. (2018). Electrochemical behaviour of manganese and ruthenium mixed oxide@ reduced graphene oxide nanoribbon composite in symmetric and asymmetric supercapacitor. **Applied Surface Science**. 427: 102-111.
- Akinwolemiwa, B., Wei, C., and Chen, G. Z. (2017). Mechanisms and Designs of Asymmetrical Electrochemical Capacitors. **Electrochimica Acta**. 247: 344-357.

- Al-Enizi, A. M., Brooks, R. M., El-Halwany, M. M., Yousef, A., Nafady, A., and Hameed, R. M. A. (2018). CoCr 7 C 3 -like nanorods embedded on carbon nanofibers as effective electrocatalyst for methanol electro-oxidation. **International Journal of Hydrogen Energy**. 43(21): 9943-9953.
- Al Garawi, M. S., Al Salman, S. A., Mansoor, A. S., Kayani, A., Al-Ghamdi, S. S., and Baig, M. R. (2017). X-ray diffraction (XRD), thermogravimetric analysis (TGA) and impedance spectroscopy studies of PM-355 as a function of proton fluence. **Radiation Measurements**. 99: 41-43.
- Alazab, M., Mitchell, G. R., Davis, F. J., and Mohan, S. D. (2017). Sustainable Electrospinning of Nanoscale Fibres. **Procedia Manufacturing**. 12: 66-78.
- Alegre, C., Modica, E., Di Blasi, A., Di Blasi, O., Busacca, C., Ferraro, M., Aricò, A. S., Antonucci, V., and Baglio, V. (2018). NiCo-loaded carbon nanofibers obtained by electrospinning: Bifunctional behavior as air electrodes. **Renewable Energy**. 125: 250-259.
- Alharbi, H. F., Luqman, M., Khalil, K. A., Elnakady, Y. A., Abd-Elkader, O. H., Rady, A. M., Alharthi, N. H., and Karim, M. R. (2018). Fabrication of core-shell structured nanofibers of poly (lactic acid) and poly (vinyl alcohol) by coaxial electrospinning for tissue engineering. **European Polymer Journal**. 98: 483-491.
- Alim, S., Kafi, A. K. M., Jose, R., Yusoff, M. M., and Vejayan, J. (2018). Enhanced direct electron transfer of redox protein based on multiporous SnO₂ nanofiber-carbon nanotube nanocomposite and its application in biosensing. **International Journal of Biol Macromol**. 114: 1071-1076.

- Alvi, M. A., and Akhtar, M. S. (2016). An effective and low cost Pd Ce bimetallic decorated carbon nanofibers as electro-catalyst for direct methanol fuel cells applications. **Journal of Alloys and Compounds**. 684: 524-529.
- Amini, M., Arash Haddadi, S., Ghaderi, S., Ramazani SA, A., and Hassan Ansarizadeh, M. (2018). Preparation and characterization of PVDF/Starch nanocomposite nanofibers using electrospinning method. **Materials Today: Proceedings**. 5(7): 15613-15619.
- Amir, F. Z., Pham, V. H., Schultheis, E. M., and Dickerson, J. H. (2018). Flexible, all-solid-state, high-cell potential supercapacitors based on holey reduced graphene oxide/manganese dioxide nanosheets. **Electrochimica Acta**. 260: 944-951.
- An, G.-H., Lee, E.-H., and Ahn, H.-J. (2016). Well-dispersed iron nanoparticles exposed within nitrogen-doped mesoporous carbon nanofibers by hydrogen-activation for oxygen-reduction reaction. **Journal of Alloys and Compounds**. 682: 746-752.
- Aneke, M., and Wang, M. (2016). Energy storage technologies and real life applications – A state of the art review. **Applied Energy**. 179: 350-377.
- Arbab, S., Teimoury, A., Mirbaha, H., Adolphe, D. C., Noroozi, B., and Nourpanah, P. (2017). Optimum stabilization processing parameters for polyacrylonitrile-based carbon nanofibers and their difference with carbon (micro) fibers. **Polymer Degradation and Stability**. 142: 198-208.
- Aswathy, R., Ulaganathan, M., and Ragupathy, P. (2018). Mn₃O₄ nanoparticles grown on surface activated graphite paper for aqueous asymmetric supercapacitors. **Journal of Alloys and Compounds**. 767: 141-150.

- Babapoor, A., Karimi, G., Golestaneh, S. I., and Mezjin, M. A. (2017). Coaxial electrospun PEG/PA6 composite fibers: Fabrication and characterization. **Applied Thermal Engineering**. 118: 398-407.
- Bae, J., Kim, H., Kim, K. S., and Choi, H. (2018). Effect of asymmetric wettability in nanofiber membrane by electrospinning technique on separation of oil/water emulsion. **Chemosphere**. 204: 235-242.
- Bai, J., Liu, Y., Hou, Y., and Wang, S. (2018). Electrospinning preparation and luminescence properties of $\text{Eu}_2(\text{PBT})_3(\text{NO}_3)_3/\text{PMMA}$ composite nanofibers. **Materials Chemistry and Physics**. 217: 486-492.
- Bai, X., Tong, X., Gao, Y., Zhu, W., Fu, C., Ma, J., Tan, T., Wang, C., Luo, Y., and Sun, H. (2018). Hierarchical multidimensional MnO_2 via hydrothermal synthesis for high performance supercapacitors. **Electrochimica Acta**. 281: 525-533.
- Bai, Y., Huang, Z.-H., and Kang, F. (2014). Surface oxidation of activated electrospun carbon nanofibers and their adsorption performance for benzene, butanone and ethanol. **Colloids and Surfaces A: Physicochemical and Engineering Aspects**. 443: 66-71.
- Bai, Y., Huang, Z.-H., Yu, X., Kaneko, K., and Kang, F. (2018). Micro-mesoporous graphitic carbon nanofiber membranes. **Carbon**. 132: 746-748.
- Bajaj, B., Joh, H.-I., Jo, S. M., Park, J. H., Yi, K. B., and Lee, S. (2018). Enhanced reactive H_2S adsorption using carbon nanofibers supported with $\text{Cu}/\text{Cu}_2\text{O}$ nanoparticles. **Applied Surface Science**. 429: 253-257.
- Balbuena, P. B., and Gubbins, K. E. (1993). Theoretical interpretation of adsorption behavior of simple fluids in slit pores. **Langmuir**. 9(7): 1801-1814.

- Balbuena, P. B., and Gubbins, K. E. (1993). Theoretical interpretation of adsorption behavior of simple fluids in slit pores. **Langmuir**. 9(7): 1801-1814.
- Bao, Y., Huang, Y., Song, X., Long, J., Wang, S., Ding, L.-X., and Wang, H. (2018). Heteroatom doping and activation of carbon nanofibers enabling ultrafast and stable sodium storage. **Electrochimica Acta**. 276: 304-310.
- Barai, H. R., Banerjee, A. N., and Joo, S. W. (2017). Improved electrochemical properties of highly porous amorphous manganese oxide nanoparticles with crystalline edges for superior supercapacitors. **Journal of Industrial and Engineering Chemistry**. 56: 212-224.
- Barrett, E. P., Joyner, L. G., and Halenda, P. P. (1951). The determination of pore volume and area distributions in porous substances. I. Computations from nitrogen isotherms. **Journal of the American chemical society**. 73(1): 373-380.
- Bhojate, S., Kahol, P. K., Sapkota, B., Mishra, S. R., Perez, F., and Gupta, R. K. (2018). Polystyrene activated linear tube carbon nanofiber for durable and high-performance supercapacitors. **Surface and Coatings Technology**. 345: 113-122.
- Bi, Y., Nautiyal, A., Zhang, H., Luo, J., and Zhang, X. (2018). One-pot microwave synthesis of NiO/MnO₂ composite as a high-performance electrode material for supercapacitors. **Electrochimica Acta**. 260: 952-958.
- Blecua, M., Fatas, E., Ocon, P., Gonzalo, B., Merino, C., de la Fuente, F., Valenciano, J., and Trinidad, F. (2017). Graphitized Carbon Nanofibers: new additive for the Negative Active Material of Lead Acid Batteries. **Electrochimica Acta**. 257: 109-117.

- Bokobza, L., Bruneel, J.-L., and Couzi, M. (2014). Raman spectroscopy as a tool for the analysis of carbon-based materials (highly oriented pyrolytic graphite, multilayer graphene and multiwall carbon nanotubes) and of some of their elastomeric composites. **Vibrational Spectroscopy**. 74: 57-63.
- Bose, S., and Sanyal, D. (2018). Synthesis and Characterization of ZnO Microfiber By Electrospinning Technique. **Materials Today: Proceedings**. 5(3): 9860-9865.
- Brolly, C., Parnell, J., and Bowden, S. (2016). Raman spectroscopy: Caution when interpreting organic carbon from oxidising environments. **Planetary and Space Science**. 121: 53-59.
- Brownson, D. A., and Banks, C. E. (2014). *The handbook of graphene electrochemistry*: Springer.
- Brunauer, S., Emmett, P. H., and Teller, E. (1938). Adsorption of gases in multimolecular layers. **Journal of the American chemical society**. 60(2): 309-319.
- Budhiraju, V. S., Kumar, R., Sharma, A., and Sivakumar, S. (2017). Structurally stable hollow mesoporous graphitized carbon nanofibers embedded with NiMoO₄ nanoparticles for high performance asymmetric supercapacitors. **Electrochimica Acta**. 238: 337-348.
- Busacca, C., Di Blasi, O., Briguglio, N., Ferraro, M., Antonucci, V., and Di Blasi, A. (2017). Electrochemical performance investigation of electrospun urchin-like V₂O₅-CNF composite nanostructure for vanadium redox flow battery. **Electrochimica Acta**. 230: 174-180.

- Byamba-Ochir, N., Shim, W. G., Balathanigaimani, M. S., and Moon, H. (2016). Highly porous activated carbons prepared from carbon rich Mongolian anthracite by direct NaOH activation. **Applied Surface Science**. 379: 331-337.
- Byles, B. W., Cullen, D. A., More, K. L., and Pomerantseva, E. (2018). Tunnel structured manganese oxide nanowires as redox active electrodes for hybrid capacitive deionization. **Nano Energy**. 44: 476-488.
- Cai, J., Niu, H., Wang, H., Shao, H., Fang, J., He, J., Xiong, H., Ma, C., and Lin, T. (2016). High-performance supercapacitor electrode from cellulose-derived, inter-bonded carbon nanofibers. **Journal of Power Sources**. 324: 302-308.
- Cai, N., Fu, J., Zeng, H., Luo, X., Han, C., and Yu, F. (2018). Reduced graphene oxide-silver nanoparticles/nitrogen-doped carbon nanofiber composites with meso-microporous structure for high-performance symmetric supercapacitor application. **Journal of Alloys and Compounds**. 742: 769-779.
- Callahan, P. G., Stinville, J. C., Yao, E. R., Echlin, M. P., Titus, M. S., De Graef, M., Gianola, D. S., and Pollock, T. M. (2018). Transmission scanning electron microscopy: Defect observations and image simulations. **Ultramicroscopy**. 186: 49-61.
- Cao, Z., Wang, C., and Chen, J. (2018). Novel mesoporous carbon nanofibers prepared via electrospinning method as host materials for Li-S battery. **Materials Letters**. 225: 157-160.
- Carotenuto, G., Longo, A., Camerlingo, C., De Nicola, S., and Pepe, G. P. (2016). Microstructures of carbon nanoscrolls characterized by polarized micro-Raman spectroscopy. **New Carbon Materials**. 31(6): 621-627.

- Castkova, K., Maca, K., Sekaninova, J., Nemcovsky, J., and Cihlar, J. (2017). Electrospinning and thermal treatment of yttria doped zirconia fibres. **Ceramics International**. 43(10): 7581-7587.
- Chai, C., Liu, A., Wang, Y., Lu, Y., and Che, H. (2018). A MoS₂-templated oxidation-etching strategy to synthesize hollow δ -MnO₂ nanospheres as a high-performance electrode for supercapacitor. **Ceramics International**. 44(14): 16923-16930.
- Chang, W.-M., Wang, C.-C., and Chen, C.-Y. (2016). Plasma-Induced Polyaniline Grafted on Carbon Nanotube-embedded Carbon Nanofibers for High-Performance Supercapacitors. **Electrochimica Acta**. 212: 130-140.
- Chang, W.-M., Wang, C.-C., and Chen, C.-Y. (2018). Fabrication of ultra-thin carbon nanofibers by centrifuged-electrospinning for application in high-rate supercapacitors. **Electrochimica Acta**.
- Chang, Y.-C., Chen, J.-Y., Kabtamu, D. M., Lin, G.-Y., Hsu, N.-Y., Chou, Y.-S., Wei, H.-J., and Wang, C.-H. (2017). High efficiency of CO₂-activated graphite felt as electrode for vanadium redox flow battery application. **Journal of Power Sources**. 364: 1-8.
- Che Othman, F. E., Yusof, N., Hasbullah, H., Jaafar, J., Ismail, A. F., Abdullah, N., Md Nordin, N. A. H., Aziz, F., and Wan Salleh, W. N. (2017). Polyacrylonitrile/magnesium oxide-based activated carbon nanofibers with well-developed microporous structure and their adsorption performance for methane. **Journal of Industrial and Engineering Chemistry**. 51: 281-287.
- Chee, W. K., Lim, H. N., Andou, Y., Zainal, Z., Hamra, A. A. B., Harrison, I., Altarawneh, M., Jiang, Z. T., and Huang, N. M. (2017). Functionalized graphene

oxide-reinforced electrospun carbon nanofibers as ultrathin supercapacitor electrode. **Journal of Energy Chemistry**. 26(4): 790-798.

Chen, G., Yao, X., Cao, Q., Ding, S., He, J., and Wang, S. (2018). Flexible free-standing SnS₂/carbon nanofibers anode for high performance sodium-ion batteries. **Materials Letters**.

Chen, H., Golder, M. R., Wang, F., Jasti, R., and Swan, A. K. (2014). Raman spectroscopy of carbon nanohoops. **Carbon**. 67: 203-213.

Chen, L., Chen, L., Ai, Q., Li, D., Si, P., Feng, J., Zhang, L., Li, Y., Lou, J., and Ci, L. (2018). Flexible all-solid-state supercapacitors based on freestanding, binder-free carbon nanofibers@polypyrrole@graphene film. **Chemical Engineering Journal**. 334: 184-190.

Chen, L., Guo, Z., Xia, Y., and Wang, Y. (2013). High-voltage aqueous battery approaching 3 V using an acidic-alkaline double electrolyte. **Chemical Communications**. 49(22): 2204-2206.

Chen, M., Jiang, S., Cai, S., Wang, X., Xiang, K., Ma, Z., Song, P., and Fisher, A. C. (2017). Hierarchical porous carbon modified with ionic surfactants as efficient sulfur hosts for the high-performance lithium-sulfur batteries. **Chemical Engineering Journal**. 313: 404-414.

Chen, Q., Heng, B., Wang, H., Sun, D., Wang, B., Sun, M., Guan, S., Fu, R., and Tang, Y. (2015). Controlled facile synthesis of hierarchical CuO@MnO₂ core-shell nanosheet arrays for high-performance lithium-ion battery. **Journal of Alloys and Compounds**. 641: 80-86.

- Chen, S., Li, R., Li, X., and Xie, J. (2018). Electrospinning: An enabling nanotechnology platform for drug delivery and regenerative medicine. **Advanced drug delivery reviews**. 132: 188-213.
- Chen, T.-L., and Elabd, Y. A. (2017). Hybrid-capacitors with polyaniline/carbon electrodes fabricated via simultaneous electrospinning/electrospraying. **Electrochimica Acta**. 229: 65-72.
- Chen, Y., Wang, J.-W., Shi, X.-C., and Chen, B.-Z. (2013). Pseudocapacitive characteristics of manganese oxide anodized from manganese coating electrodeposited from aqueous solution. **Electrochimica Acta**. 109: 678-683.
- Cheng, G., Ma, X., Li, J., Cheng, Y., Cao, Y., Wang, Z., Shi, X., Du, Y., Deng, H., and Li, Z. (2018). Incorporating platelet-rich plasma into coaxial electrospun nanofibers for bone tissue engineering. **International Journal of Pharmacy**. 547(1-2): 656-666.
- Cheng, Y., Wei, Z., Du, Q., Liu, F., Duan, X., Wang, Y., Jia, D., Zhou, Y., and Li, B. (2018). The shape effect of manganese(II,III) oxide nanoparticles on the performance of electrochemical capacitors. **Electrochimica Acta**. 284: 408-417.
- Cheng, Z., Cao, J., Kang, L., Luo, Y., Li, T., and Liu, W. (2018). Novel transparent nano-pattern window screen for effective air filtration by electrospinning. **Materials Letters**. 221: 157-160.
- Chesnokov, V. V., Podyacheva, O. Y., Shmakov, A. N., Kibis, L. S., Boronin, A. I., and Ismagilov, Z. R. (2016). Comparison of growth mechanisms of undoped and nitrogen-doped carbon nanofibers on nickel-containing catalysts. **Chinese Journal of Catalysis**. 37(1): 169-176.

- Chi, H. Z., Wu, Y. Q., Shen, Y. K., Zhang, C., Xiong, Q., and Qin, H. (2018). Electrodepositing manganese oxide into a graphene hydrogel to fabricate an asymmetric supercapacitor. **Electrochimica Acta**. 289: 158-167.
- Choi, J.-Y., Hyun, Y., Park, H.-K., and Lee, C.-S. (2018). Synthesis and electrochemical performance of transition metal-coated carbon nanofibers as anode materials for lithium secondary batteries. **Journal of Industrial and Engineering Chemistry**.
- Choi, Y., Park, M., Kyoung Shin, H., Liu, Y., Choi, J.-W., Nirmala, R., Park, S.-J., and Kim, H.-Y. (2014). Facile stabilization process of polyacrylonitrile-based electrospun nanofibers by spraying 1% hydrogen peroxide and electron beam irradiation. **Materials Letters**. 123: 59-61.
- Chung, K.-H., Jeong, S., Kim, B.-J., An, K.-H., Park, Y.-K., and Jung, S.-C. (2018). Enhancement of photocatalytic hydrogen production by liquid phase plasma irradiation on metal-loaded TiO₂/carbon nanofiber photocatalysts. **International Journal of Hydrogen Energy**. 43(24): 11422-11429.
- Coimbra, P., Freitas, J. P., Gonçalves, T., Gil, M. H., and Figueiredo, M. (2019). Preparation of gentamicin sulfate eluting fiber mats by emulsion and by suspension electrospinning. **Materials Science and Engineering: C**. 94: 86-93.
- Cougnon, C., Lebègue, E., and Pognon, G. (2015). Impedance spectroscopy study of a catechol-modified activated carbon electrode as active material in electrochemical capacitor. **Journal of Power Sources**. 274: 551-559.

- Davoglio, R. A., Cabello, G., Marco, J. F., and Biaggio, S. R. (2018). Synthesis and characterization of α -MnO₂ nanoneedles for electrochemical supercapacitors. **Electrochimica Acta**. 261: 428-435.
- de Souza, W., and Attias, M. (2018). New advances in scanning microscopy and its application to study parasitic protozoa. **Experimental Parasitology**. 190: 10-33.
- Dejoie, C., Autran, P.-O., Bordet, P., Fitch, A. N., Martinetto, P., Sciau, P., Tamura, N., and Wright, J. (2018). X-ray diffraction and heterogeneous materials: An adaptive crystallography approach. **Comptes Rendus Physique**.
- Delgado-Mellado, N., Larriba, M., Navarro, P., Rigual, V., Ayuso, M., García, J., and Rodríguez, F. (2018). Thermal stability of choline chloride deep eutectic solvents by TGA/FTIR-ATR analysis. **Journal of Molecular Liquids**. 260: 37-43.
- Deng, N., Kang, W., Ju, J., Fan, L., Zhuang, X., Ma, X., He, H., Zhao, Y., and Cheng, B. (2017). Polyvinyl Alcohol-derived carbon nanofibers/carbon nanotubes/sulfur electrode with honeycomb-like hierarchical porous structure for the stable-capacity lithium/sulfur batteries. **Journal of Power Sources**. 346: 1-12.
- Dincer, K., Waisi, B., Önal, G., Tuğluoğlu, N., McCutcheon, J., and Yüksel, Ö. F. (2018). Investigation of optical and dispersion parameters of electrospinning grown activated carbon nanofiber (ACNF) layer. **Synthetic Metals**. 237: 16-22.
- Ding, J., Lu, Z., Wu, M., Liu, C., Yang, Y., Ji, H., and Yang, G. (2018). Carbon coated SnO₂ particles stabilized in the elastic network of carbon nanofibers and its

- improved electrochemical properties. **Materials Chemistry and Physics**. 215: 285-292.
- Ding, J., Zhang, H.-p., Li, X., Tang, Y., and Yang, G. (2018). Crosslinked carbon nanofiber films with hierarchical pores as flexible electrodes for high performance supercapacitors. **Materials and Design**. 141: 17-25.
- Dobrovolskaya, I. P., Yudin, V. E., Popryadukhin, P. V., Ivan'kova, E. M., Shabunin, A. S., Kasatkin, I. A., and Morgantie, P. (2018). Effect of chitin nanofibrils on electrospinning of chitosan-based composite nanofibers. **Carbohydrate Polymer**. 194: 260-266.
- Dong, Q., Wang, G., Hu, H., Yang, J., Qian, B., Ling, Z., and Qiu, J. (2013). Ultrasound-assisted preparation of electrospun carbon nanofiber/graphene composite electrode for supercapacitors. **Journal of Power Sources**. 243: 350-353.
- Dong, Y., Lin, H., Zhou, D., Niu, H., Jin, Q., and Qu, F. (2015). Synthesis of mesoporous graphitic carbon fibers with high performance for supercapacitor. **Electrochimica Acta**. 159: 116-123.
- Dupont, M. F., and Donne, S. W. (2016). Charge storage mechanisms in electrochemical capacitors: Effects of electrode properties on performance. **Journal of Power Sources**. 326: 613-623.
- Ensafi, A. A., Ahmadi, N., Rezaei, B., Abdolmaleki, A., and Mahmoudian, M. (2018). A new quaternary nanohybrid composite electrode for a high-performance supercapacitor. **Energy**. 164: 707-721.
- Fan, L., Yang, L., Ni, X., Han, J., Guo, R., and Zhang, C. (2016). Nitrogen-enriched meso-macroporous carbon fiber network as a binder-free flexible electrode for supercapacitors. **Carbon**. 107: 629-637.

- Fang, F., Jing, W. Q., and Yang, W. (2018). High performance electrospinning fibrous membranes for infrared stealth camouflage. **Infrared Physics and Technology**. 93: 130-135.
- Gadkari, S. B. (2014). Scaling analysis for electrospinning. **Springer Plus**. 3(705).
- Gao, P., Tong, Q., Lv, J., Wang, Y., and Ma, Y. (2017). X-ray diffraction data-assisted structure searches. **Computer Physics Communications**. 213: 40-45.
- Gao, Q., Wang, J., Ke, B., Wang, J., and Li, Y. (2018). Fe doped δ -MnO₂ nanoneedles as advanced supercapacitor electrodes. **Ceramics International**. 44(15): 18770-18775.
- Gao, X., Li, F., Wang, R., and Zhang, T. (2018). A formaldehyde sensor: Significant role of p - n heterojunction in gas-sensitive core-shell nanofibers. **Sensors and Actuators B: Chemical**. 258: 1230-1241.
- Gee, S., Johnson, B., and Smith, A. L. (2018). Optimizing electrospinning parameters for piezoelectric PVDF nanofiber membranes. **Journal of Membrane Science**. 563: 804-812.
- Geelen, D., Thete, A., Schaff, O., Kaiser, A., van der Molen, S. J., and Tromp, R. (2015). eV-TEM: Transmission electron microscopy in a low energy cathode lens instrument. **Ultramicroscopy**. 159 Pt 3: 482-487.
- Ghasemi, S., Hosseini, S. R., and Boore-Talari, O. (2018). Sonochemical assisted synthesis MnO₂/RGO nanohybrid as effective electrode material for supercapacitor. **Ultrason Sonochem**. 40(Pt A): 675-685.
- Gnana Sundara Raj, B., Kim, H.-Y., and Kim, B.-S. (2018). Ultrasound assisted formation of Mn₂SnO₄ nanocube as electrodes for high performance symmetrical hybrid supercapacitors. **Electrochimica Acta**. 278: 93-105.

- González, A., Goikolea, E., Barrena, J. A., and Mysyk, R. (2016). Review on supercapacitors: Technologies and materials. **Renewable and Sustainable Energy Reviews**. 58: 1189-1206.
- Goodenough, J. B., Abruna, H., and Buchanan, M. (2007). Basic research needs for electrical energy storage. Paper presented at the Report of **the basic energy sciences workshop for electrical energy storage**.
- Hasanzadeh, S., Schaublin, R., Decamps, B., Rousson, V., Autissier, E., Barthe, M. F., and Hebert, C. (2018). Three-dimensional scanning transmission electron microscopy of dislocation loops in tungsten. **Micron**. 113: 24-33.
- Hayakawa, E. H., and Matsuoka, H. (2016). Detailed methodology for high resolution scanning electron microscopy (SEM) of murine malaria parasitized-erythrocytes. **Parasitol Int**. 65(5 Pt B): 539-544.
- He, R.-X., and Zha, D.-W. (2017). Cyclic voltammetry and voltabsorptometry studies of redox mechanism of lumazine. **Journal of Electroanalytical Chemistry**. 791: 103-108.
- He, X., Hu, Y., Shen, Z., Chen, R., Wu, K., Cheng, Z., Zhang, X. W., and Pan, P. (2017). Channelized carbon nanofiber with uniform-dispersed GeO₂ as anode for long-lifespan lithium-ion batteries. **Journal of Alloys and Compounds**. 729: 313-322.
- Hsieh, W.-h., Cheng, W.-t., Chen, L.-c., and Lin, S.-y. (2018). Non-isothermal dehydration kinetic study of aspartame hemihydrate using DSC, TGA and DSC-FTIR microspectroscopy. **Asian Journal of Pharmaceutical Sciences**. 13(3): 212-219.

- Huang, J., Liu, X., Chen, G., Zhang, N., Ma, R., and Qiu, G. (2018). Selective fabrication of porous iron oxides hollow spheres and nanofibers by electrospinning for photocatalytic water purification. **Solid State Sciences**. 82: 24-28.
- Huang, W., Zou, T., Li, S., Jing, J., Xia, X., and Liu, X. (2013). Drug-loaded zein nanofibers prepared using a modified coaxial electrospinning process. **AAPS PharmSciTech**. 14(2): 675-681.
- Huang, Y., Cui, F., Zhao, Y., Lian, J., Bao, J., and Li, H. (2018). Controlled growth of ultrathin NiMoO₄ nanosheets on carbon nanofiber membrane as advanced electrodes for asymmetric supercapacitors. **Journal of Alloys and Compounds**. 753: 176-185.
- Huang, Y., Zhao, Y., Bao, J., Lian, J., Cheng, M., and Li, H. (2018). Lawn-like FeCo₂S₄ hollow nanoneedle arrays on flexible carbon nanofiber film as binder-free electrodes for high-performance asymmetric pseudocapacitors. **Journal of Alloys and Compounds**.
- Huang, Z.-X., Liu, X., Wu, J., Wong, S.-C., and Qu, J.-P. (2018). Electrospinning water harvesters inspired by spider silk and beetle. **Materials Letters**. 211: 28-31.
- Inagaki, M., Yang, Y., and Kang, F. (2012). Carbon nanofibers prepared via electrospinning. **Advance Materials**. 24(19): 2547-2566.
- Isik, B. S., Altay, F., and Capanoglu, E. (2018). The uniaxial and coaxial encapsulations of sour cherry (*Prunus cerasus* L.) concentrate by electrospinning and their in vitro bioaccessibility. **Food Chemistry**. 265: 260-273.
- Jeong, J. H., and Kim, B.-H. (2018). Electrospun porous carbon nanofibers with controllable pore sizes by boron trioxide for electrochemical capacitor

- electrodes. **Journal of the Taiwan Institute of Chemical Engineers.** 84: 179-187.
- Jia, L., Shi, Y., Zhang, Q., and Xu, X. (2018). Green synthesis of ultrafine Methyl-cellulose-derived porous carbon/MnO₂ nanowires for asymmetric supercapacitors and flexible pattern stamping. **Applied Surface Science.** 462: 923-931.
- Jiandong Liu , J. L., Caiyun Wang , Jianmin Ma. (2018). Electrospun CoSe@N-doped carbon nanofibers with highly capacitive Li storage. **Journal of Energy Chemistry.**
- Kadam, S. L., Mane, S. M., Tirmali, P. M., and Kulkarni, S. B. (2018). Electrochemical synthesis of flower like Mn-Co mixed metal oxides as electrode material for supercapacitor application. **Current Applied Physics.** 18(4): 397-404.
- Kang, D. H., and Kang, H. W. (2018). Advanced electrospinning using circle electrodes for freestanding PVDF nanofiber film fabrication. **Applied Surface Science.** 455: 251-257.
- Kogularasu, S., Akilarasan, M., Chen, S.-M., Elaiyappillai, E., Johnson, P. M., Chen, T.-W., Al-Hemaid, F. M. A., Ali, M. A., and Elshikh, M. S. (2018). A comparative study on conventionally prepared MnFe₂O₄ nanospheres and template-synthesized novel MnFe₂O₄ nano-agglomerates as the electrodes for biosensing of mercury contaminations and supercapacitor applications. **Electrochimica Acta.** 290: 533-543.
- Korhammer, K., Neumann, K., Opel, O., and Ruck, W. K. L. (2018). Thermodynamic and kinetic study of CaCl₂-CH₃OH adducts for solid sorption refrigeration by TGA/DSC. **Applied Energy.** 230: 1255-1278.

- Kwak, H. W., Shin, M., Lee, J. Y., Yun, H., Song, D. W., Yang, Y., Shin, B. S., Park, Y. H., and Lee, K. H. (2017). Fabrication of an ultrafine fish gelatin nanofibrous web from an aqueous solution by electrospinning. **Internatinal Journal of Biol Macromol.** 102: 1092-1103.
- Lan, S., Gaeini, M., Zondag, H., van Steenhoven, A., and Rindt, C. (2018). Direct numerical simulation of the thermal dehydration reaction in a TGA experiment. **Applied Thermal Engineering.** 128: 1175-1185.
- Lapham, D. P., and Lapham, J. L. (2017). Gas adsorption on commercial magnesium stearate: Effects of degassing conditions on nitrogen BET surface area and isotherm characteristics. **Internationla Journal of Pharmcy.** 530(1-2): 364-376.
- Lasprilla-Botero, J., Álvarez-Láinez, M., and Lagaron, J. M. (2018). The influence of electrospinning parameters and solvent selection on the morphology and diameter of polyimide nanofibers. **Materials Today Communications.** 14: 1-9.
- Le Corre-Bordes, D., Hofman, K., and Hall, B. (2018). Guide to electrospinning denatured whole chain collagen from hoki fish using benign solvents. **International Journal of Biology Macromol.** 112: 1289-1299.
- Lee, H.-M., Kwac, L.-K., An, K.-H., Park, S.-J., and Kim, B.-J. (2016). Electrochemical behavior of pitch-based activated carbon fibers for electrochemical capacitors. **Energy Conversion and Management.** 125: 347-352.
- Lei, J., Zhou, J., Li, J., Wen, J., Su, L., Duan, T., and Zhu, W. (2018). Novel collagen waste derived Mn-doped nitrogen-containing carbon for supercapacitors. **Electrochimica Acta.** 285: 292-300.

- Li, L., Hou, L., Cheng, J., Simmons, T., Zhang, F., Zhang, L. T., Linhardt, R. J., and Koratkar, N. (2018). A flexible carbon/sulfur-cellulose core-shell structure for advanced lithium–sulfur batteries. **Energy Storage Materials**.
- Li, L., Zhang, X., Wang, D., Zhang, W., Li, X., Zhao, X., Zhang, Q., Gu, L., Yu, Z., and Wu, M. (2018). Electrospinning synthesis of high performance carbon nanofiber coated flower-like MoS₂ nanosheets for dye-sensitized solar cells counter electrode. **Electrochimica Acta**. 280: 94-100.
- Li, R.-B., Yu, L.-L., Li, S., Fan, J., Luo, R., and Zhao, J.-T. (2018). Facile synthesis of hierarchical mesoporous beta-manganese dioxide nanoflowers with extremely high specific surface areas for high-performance electrochemical capacitors. **Electrochimica Acta**. 284: 52-59.
- Li, Y., Ou-Yang, W., Xu, X., Wang, M., Hou, S., Lu, T., Yao, Y., and Pan, L. (2018). Micro-/mesoporous carbon nanofibers embedded with ordered carbon for flexible supercapacitors. **Electrochimica Acta**. 271: 591-598.
- LichaoFeng, E. Y., NingXie, E. Y., and Zhong, J. (2014). Carbon nanofibers and their composites: a review of synthesizing, properties and applications. **Materials**. 7(5): 3919-3945.
- Lin, Z., Taberna, P.-L., and Simon, P. (2018). Advanced analytical techniques to characterize materials for electrochemical capacitors. **Current Opinion in Electrochemistry**.
- Liu, D., Yuan, W., Yuan, P., Yu, W., Tan, D., Liu, H., and He, H. (2013). Physical activation of diatomite-templated carbons and its effect on the adsorption of methylene blue (MB). **Applied Surface Science**. 282: 838-843.

- Liu, K., Ostadhassan, M., and Kong, L. (2018). Multifractal characteristics of Longmaxi Shale pore structures by N₂ adsorption: A model comparison. **Journal of Petroleum Science and Engineering**. 168: 330-341.
- Liu, Y., Zhu, X., Wei, X., Zhang, S., Chen, J., and Ren, Z. J. (2018). CO₂ activation promotes available carbonate and phosphorus of antibiotic mycelial fermentation residue-derived biochar support for increased lead immobilization. **Chemical Engineering Journal**. 334: 1101-1107.
- Liv, N., Lazic, I., Kruit, P., and Hoogenboom, J. P. (2014). Scanning electron microscopy of individual nanoparticle bio-markers in liquid. **Ultramicroscopy**. 143: 93-99.
- López-Lapeña, O., and Pallas-Areny, R. (2018). Solar energy radiation measurement with a low-power solar energy harvester. **Computers and Electronics in Agriculture**. 151: 150-155.
- Mahle, J. J. (2002). An adsorption equilibrium model for Type 5 isotherms. **Carbon**. 40(15): 2753-2759.
- Mendes, A. C., Stephansen, K., and Chronakis, I. S. (2017). Electrospinning of food proteins and polysaccharides. **Food Hydrocolloids**. 68: 53-68.
- Miller, J. R. (2017). Perspective on electrochemical capacitor energy storage. **Applied Surface Science**.
- Morikawa, K., Green, M., and Naraghi, M. (2018). A Novel Approach for Melt Electrospinning of Polymer Fibers. . **Procedia Manufacturing**. 26: 205-208.
- Nilmoung, S., Sinprachim, T., Kotutha, I., Kidkhunthod, P., Yimnirun, R., Rujirawat, S., and Maensiri, S. (2016). Electrospun carbon/CuFe₂O₄ composite

nanofibers with improved electrochemical energy storage performance.

Journal of Alloys and Compounds. 688: 1131-1140.

Nithya, V., Selvan, R. K., Kalpana, D., Vasylechko, L., and Sanjeeviraja, C. (2013).

Synthesis of Bi₂WO₆ nanoparticles and its electrochemical properties in different electrolytes for pseudocapacitor electrodes. **Electrochimica Acta**.

109: 720-731.

Niu, H., Wang, X., and Lin, T. (2012). Carbon Nanofibers with Inter-bonded Fibrous

Structure for Supercapacitor Application. **Proceedings of the World Congress**

on Advances in Civil, Environmental, and Materials Research: 550-557.

Pajarre, R., and Koukkari, P. (2018). CALPHAD aqueous solution model based on the

BET approach: General theory. **Calphad**. 63: 1-5.

Park, J. E., Kim, M.-J., Lim, M. S., Kang, S. Y., Kim, J. K., Oh, S.-H., Her, M., Cho,

Y.-H., and Sung, Y.-E. (2018). Graphitic carbon nitride-carbon nanofiber as

oxygen catalyst in anion-exchange membrane water electrolyzer and rechargeable metal-air cells. **Applied Catalysis B: Environmental**. 237: 140-

148.

Park, S.-J., Park, S., and Kim, S. (2012). Preparation and capacitance behaviors of

cobalt oxide/graphene composites. **Carbon letters**. 13(2): 130-132.

Pech, D., Brunet, M., Durou, H., Huang, P., Mochalin, V., Gogotsi, Y., Taberna, P.-L.,

and Simon, P. (2010). Ultrahigh-power micrometre-sized supercapacitors based

on onion-like carbon. **Nat Nano**. 5(9): 651-654.

Pongprayoon, T., Ayutthaya, M. S.-N., and Pochai, C. (2017). Electrochemical

capacitor improvement fabricated by carbon microfiber composite with

admicellar-modified carbon nanotube. **Applied Surface Science**. 396: 723-731.

- Randviir, E. P. (2018). A cross examination of electron transfer rate constants for carbon screen-printed electrodes using Electrochemical Impedance Spectroscopy and cyclic voltammetry. **Electrochimica Acta**. 286: 179-186.
- Ranganatha, S., and Munichandraiah, N. (2018). γ -MnS nanoparticles anchored reduced graphene oxide: Electrode materials for high performance supercapacitors. **Journal of Science: Advanced Materials and Devices**.
- Sangwichien, C., Aranovich, G. L., and Donohue, M. D. (2002). Density functional theory predictions of adsorption isotherms with hysteresis loops. **Colloids and Surfaces A: Physicochemical and Engineering Aspects**,. 206(1-3): 313-320.
- Sankar, S., Inamdar, A. I., Im, H., Lee, S., and Kim, D. Y. (2018). Template-free rapid sonochemical synthesis of spherical α -MnO₂ nanoparticles for high-energy supercapacitor electrode. **Ceramics International**. 44(14): 17514-17521.
- Sarwar, W., Marinescu, M., Green, N., Taylor, N., and Offer, G. (2016). Electrochemical double layer capacitor electro-thermal modelling. **Journal of Energy Storage**. 5: 10-24.
- Sinprachim, T., Phumying, S., and Maensiri, S. (2016). Electrochemical energy storage performance of electrospun AgO_x-MnO_x/CNF composites. **Journal of Alloys and Compounds**. 677: 1-11.
- Soares, R. M. D., Siqueira, N. M., Prabhakaram, M. P., and Ramakrishna, S. (2018). Electrospinning and electrospray of bio-based and natural polymers for biomaterials development. **Materials Science Engineering C Mater Biol Appl**. 92: 969-982.

- Someshwararao, M. V., Dubey, R. S., Subbarao, P. S. V., and Singh, S. (2018). Electrospinning Process Parameters Dependent Investigation of TiO₂ Nanofibers. **Results in Physics**.
- Song, M. J., and Shin, M. W. (2014). Fabrication and characterization of carbon nanofiber@mesoporous carbon core-shell composite for the Li-air battery. **Applied Surface Science**. 320: 435-440.
- Streckova, M., Sopcak, T., Stulajterova, R., Giretova, M., Medvecký, L., Kovalčíková, A., and Balazsi, K. (2018). Needle-less electrospinning employed for calcium and magnesium phosphate coatings on titanium substrates. **Surface and Coatings Technology**. 340: 177-189.
- Sun, X., Zhang, X., Liu, W., Wang, K., Li, C., Li, Z., and Ma, Y. (2017). Electrochemical performances and capacity fading behaviors of activated carbon/hard carbon lithium ion capacitor. **Electrochimica Acta**. 235: 158-166.
- Tang, Y., Zheng, S., Xu, Y., Xiao, X., Xue, H., and Pang, H. (2018). Advanced batteries based on manganese dioxide and its composites. **Energy Storage Materials**. 12: 284-309.
- Tavakoli Ferooshani, F., Tavanai, H., Ranjbar, M., and Bahrami, H. (2018). Fabrication of tungsten oxide nanofibers via electrospinning for gasochromic hydrogen detection. **Sensors and Actuators B: Chemical**. 268: 319-327.
- Tavanai, H., Jalili, R., and Morshed, M. (2009). Effects of fiber diameter and CO₂ activation temperature on the pore characteristics of polyacrylonitrile based activated carbon nanofibers. **Surface and Interface Analysis**. 41(10): 814-819.
- Tian, K., Wei, L., Zhang, X., Jin, Y., and Guo, X. (2017). Membranes of carbon nanofibers with embedded MoO₃ nanoparticles showing superior cycling

- performance for all-solid-state flexible supercapacitors. **Materials Today Energy**. 6: 27-35.
- Wang, H., Jiang, Y., and Manthiram, A. (2019). N-doped Fe₃C@C as an efficient polyselenide reservoir for high-performance sodium-selenium batteries. **Energy Storage Materials**. 16: 374-382.
- Wang, H., Liu, B., Huang, W., Lin, Z., Luo, J., Li, Y., Zhuang, L., Wang, W., and Jiang, L. (2018). Continuous needleless electrospinning of magnetic nanofibers from magnetization-induced self-assembling PVA/ferrofluid cone array. **Journal of Magnetism and Magnetic Materials**. 452: 1-4.
- Wei, Y., Zhang, L., Gong, C., Liu, S., Zhang, M., Shi, Y., and Zhang, J. (2018). Fabrication of TiN/Carbon nanofibers by electrospinning and their electromagnetic wave absorption properties. **Journal of Alloys and Compounds**. 735: 1488-1493.
- Willis, D. J., Niezrecki, C., Kuchma, D., Hines, E., Arwade, S. R., Barthelmie, R. J., DiPaola, M., Drane, P. J., Hansen, C. J., Inalpolat, M., Mack, J. H., Myers, A. T., and Rotea, M. (2018). Wind energy research: State-of-the-art and future research directions. **Renewable Energy**. 125: 133-154.
- Wu, W., Qi, W., Zhao, Y., Tang, X., Qiu, Y., Su, D., Fan, H., and Wang, G. (2019). Hollow CeO₂ spheres conformally coated with graphitic carbon for high-performance supercapacitor electrodes. **Applied Surface Science**. 463: 244-252.
- Wu, Y., Liu, Z., and Ran, F. (2019). New comprehensions on structure superiority of asymmetric carbon membrane and controlled construction of advanced

hierarchical inner-structure for high performance supercapacitors. **Microporous and Mesoporous Materials**. 275: 14-25.

Xia, G., Zhang, L., Chen, X., Huang, Y., Sun, D., Fang, F., Guo, Z., and Yu, X. (2018).

Carbon hollow nanobubbles on porous carbon nanofibers: An ideal host for high-performance sodium-sulfur batteries and hydrogen storage. **Energy Storage Materials**. 14: 314-323.

Xiao, X., Wang, Y., Chen, G., Wang, L., and Wang, Y. (2017). Mn₃O₄/activated carbon

composites with enhanced electrochemical performances for electrochemical capacitors. **Journal of Alloys and Compounds**. 703: 163-173.

Xie, W., Jiang, X., Qin, T., Yang, H., Liu, D., and He, D. (2017). Inner porous carbon

nanofibers as binder-free electrodes for high-rate supercapacitors. **Electrochimica Acta**. 258: 1064-1071.

Xu, C., Yang, X., Li, X., Liu, T., and Zhang, H. (2017). Ultrathin free-standing

electrospun carbon nanofibers web as the electrode of the vanadium flow batteries. **Journal of Energy Chemistry**. 26(4): 730-737.

Xu, H., Bronner, T., Yamamoto, M., and Yamane, H. (2018). Regeneration of cellulose

dissolved in ionic liquid using laser-heated melt-electrospinning. **Carbohydrate polymers**. 201: 182-188.

Xu, J., Zhang, L., Xu, G., Sun, Z., Zhang, C., Ma, X., Qi, C., Zhang, L., and Jia, D.

(2018). Facile synthesis of NiS anchored carbon nanofibers for high-performance supercapacitors. **Applied Surface Science**. 434: 112-119.

Yadav, P., Pandey, K., Bhatt, P., Tripathi, B., Pandey, M. K., and Kumar, M. (2016).

Probing the electrochemical properties of TiO₂/graphene composite by cyclic

- voltammetry and impedance spectroscopy. **Materials Science and Engineering: B**. 206: 22-29.
- Yan, H., Mahanta, N. K., Wang, B., Wang, S., Abramson, A. R., and Cakmak, M. (2014). Structural evolution in graphitization of nanofibers and mats from electrospun polyimide–mesophase pitch blends. **Carbon**. 71: 303-318.
- Yang, K. S., Kim, C. H., and Kim, B.-H. (2015). Preparation and electrochemical properties of RuO₂-containing activated carbon nanofiber composites with hollow cores. **Electrochimica Acta**. 174: 290-296.
- Yang, S., Guo, Z., Sheng, G., and Wang, X. (2012). Application of a novel plasma-induced CD/MWCNT/iron oxide composite in zinc decontamination. **Carbohydrate polymers**. 90(2): 1100-1105.
- Yang, Y., Zeng, D., Yang, S., Gu, L., Liu, B., and Hao, S. (2019). Nickel cobaltite nanosheets coated on metal-organic framework-derived mesoporous carbon nanofibers for high-performance pseudocapacitors. **Journal of colloid and interface science**. 534: 312-321.
- Yao, Y., Wu, H., Huang, L., Li, X., Yu, L., Zeng, S., Zeng, X., Yang, J., and Zou, J. (2017). Nitrogen-enriched hierarchically porous carbon nanofiber network as a binder-free electrode for high-performance supercapacitors. **Electrochimica Acta**. 246: 606-614.
- Yao, Y., Wu, H., and Ping, J. (2019). Simultaneous determination of Cd(II) and Pb(II) ions in honey and milk samples using a single-walled carbon nanohorns modified screen-printed electrochemical sensor. **Food Chemistry**. 274: 8-15.

- Yoo, S. H., Joh, H.-I., and Lee, S. (2017). Synthesis of porous carbon nanofiber with bamboo-like carbon nanofiber branches by one-step carbonization process. **Applied Surface Science**. 402: 456-462.
- You, X., Ye, C., and Guo, P. (2017). Electric field manipulation for deposition control in near-field electrospinning. **Journal of Manufacturing Processes**. 30: 431-438.
- Youe, W. J., Lee, S. M., Lee, S. S., Lee, S. H., and Kim, Y. S. (2016). Characterization of carbon nanofiber mats produced from electrospun lignin-g-polyacrylonitrile copolymer. **International Journal of Biology Macromol**. 82: 497-504.
- Yu, D.-G., Xu, Y., Li, Z., Du, L.-P., Zhao, B.-G., and Wang, X. (2014). Coaxial Electrospinning with Mixed Solvents: From Flat to Round Eudragit L100 Nanofibers for Better Colon-Targeted Sustained Drug Release Profiles. **Journal of Nanomaterials**. 2014: 1-8.
- Yuan, C., Wu, H. B., Xie, Y., and Lou, X. W. (2014). Mixed transition-metal oxides: design, synthesis, and energy-related applications. **Angew Chem Int Ed Engl**. 53(6): 1488-1504.
- Yuan, T., Qi, X., Liu, Z., Yang, J., Guan, C., Long, Q., Cao, J., Luo, M., Yang, X., and Yuan, L. (2018). Humidity sensor based on micro optical fiber array fabricated by electrospinning. **Optics Communications**. 427: 517-521.
- Zarrin, N., Tavanai, H., Abdolmaleki, A., Bazarganipour, M., and Alihosseini, F. (2018). An investigation on the fabrication of conductive polyethylene dioxythiophene (PEDOT) nanofibers through electrospinning. **Synthetic Metals**. 244: 143-149.

- Zeng, Y., Li, X., Jiang, S., He, S., Fang, H., and Hou, H. (2015). Free-standing mesoporous electrospun carbon nanofiber webs without activation and their electrochemical performance. **Materials Letters**. 161: 587-590.
- Zhai, Y., Dou, Y., Zhao, D., Fulvio, P. F., Mayes, R. T., and Dai, S. (2011). Carbon materials for chemical capacitive energy storage. **Advace Materials**. 23(42): 4828-4850.
- Zhang, B., Kang, F., Tarascon, J.-M., and Kim, J.-K. (2016). Recent advances in electrospun carbon nanofibers and their application in electrochemical energy storage. **Progress in Materials Science**. 76: 319-380.
- Zhang, C., Feng, F., and Zhang, H. (2018). Emulsion electrospinning: Fundamentals, food applications and prospects. **Trends in Food Science and Technology**. 80: 175-186.
- Zhang, K., Li, Z., Kang, W., Deng, N., Yan, J., Ju, J., Liu, Y., and Cheng, B. (2018). Preparation and characterization of tree-like cellulose nanofiber membranes via the electrospinning method. **Carbohydr Polymer**. 183: 62-69.
- Zhang, L., Jiang, Y., Wang, L., Zhang, C., and Liu, S. (2016). Hierarchical porous carbon nanofibers as binder-free electrode for high-performance supercapacitor. **Electrochimica Acta**. 196: 189-196.
- Zhang, L., Xia, G., Guo, Z., Sun, D., Li, X., and Yu, X. (2016). In situ fabrication of three-dimensional nitrogen and boron co-doped porous carbon nanofibers for high performance lithium-ion batteries. **Journal of Power Sources**. 324: 294-301.
- Zhang, X., Hao, Y., Shang, C., Chen, X., Li, W., Hu, S., and Cui, G. (2018). Coaxial titanium vanadium nitride core-sheath nanofibers with enhanced

electrocatalytic activity for triiodide reduction in dye-sensitized solar cells.

Electrochimica Acta. 271: 388-396.

Zhang, Y., Wang, F., Zhu, H., Zhou, L., Zheng, X., Li, X., Chen, Z., Wang, Y., Zhang, D., and Pan, D. (2017). Preparation of nitrogen-doped biomass-derived carbon nanofibers/graphene aerogel as a binder-free electrode for high performance supercapacitors. **Applied Surface Science.** 426: 99-106.

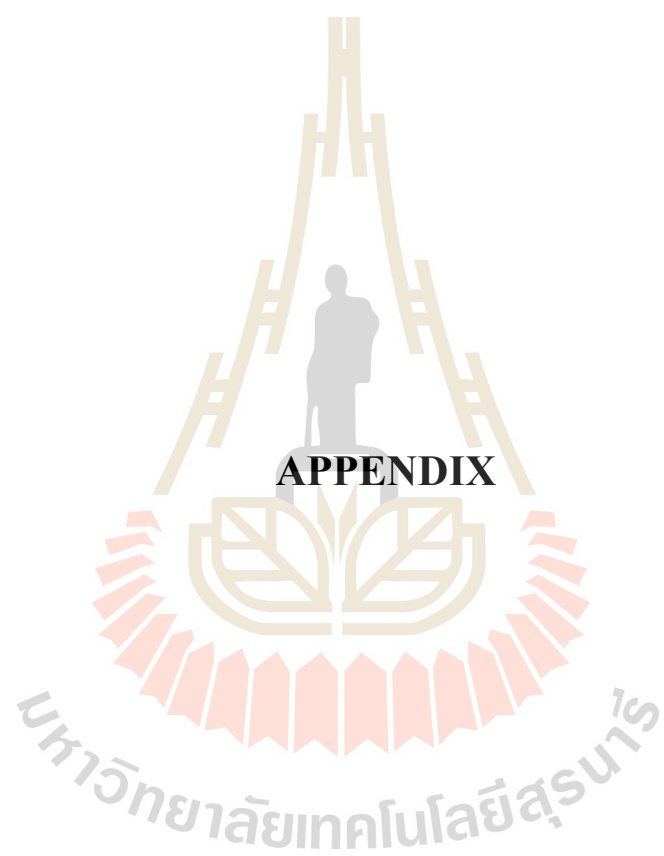
Zhao, F., Zhao, X., Peng, B., Gan, F., Yao, M., Tan, W., Dong, J., and Zhang, Q. (2017). Polyimide-derived carbon nanofiber membranes as anodes for high-performance flexible lithium ion batteries. **Chinese Chemical Letters.**

Zhao, Z., Shi, S., Cao, H., and Li, Y. (2017). Electrochemical impedance spectroscopy and surface properties characterization of anion exchange membrane fouled by sodium dodecyl sulfate. **Journal of Membrane Science.** 530: 220-231.

Zhu, Q., Wang, M., Nan, B., Shi, H., Zhang, X., Deng, Y., Wang, L., Chen, Q., and Lu, Z. (2017). Core/shell nanostructured $\text{Na}_3\text{V}_2(\text{PO}_4)_3/\text{TiO}_2$ composite nanofibers as a stable anode for sodium-ion batteries. **Journal of Power Sources.** 362: 147-159.

Zhu, X., Niu, Q., Xu, Y., Wu, G., Li, G., Nie, J., and Ma, G. (2018). From small molecules to polymer fibers: Photopolymerization with electrospinning on the fly. **Journal of Photochemistry and Photobiology A: Chemistry.** 353: 101-107.

Zuniga, L., Agubra, V., Flores, D., Campos, H., Villareal, J., and Alcoutlabi, M. (2016). Multichannel hollow structure for improved electrochemical performance of $\text{TiO}_2/\text{Carbon}$ composite nanofibers as anodes for lithium ion batteries. **Journal of Alloys and Compounds.** 686: 733-743.



APPENDIX

APPENDIX

PUBLICATIONS AND PRESENTATIONS

A.1 List of publications

Pech, O., Nettonglang, C., and Maensiri, S., (2017), Fabrication and electrochemical properties of electrospun porous carbon nanofibers. E-proceeding: **The First Material Research Society of Thailand International Conference**. Symposium 3: Graphene and Carbon Materials. pp. 67-76.

Pech, O. and Maensiri, S., Electrochemical performances of electrospun carbon nanofibers, interconnected carbon nanofibers, and carbon-manganese oxide composite nanofibers, **Journal of Alloys and compounds** **781** (2019) 541-552, DOI: <https://doi.org/10.1016/j.jallcom.2018.12.088>

A.2 List of Oral presentations

Pech., O. and Maensiri, S., (Sept. 2016), Fabrication and Characterization of Electro-spun Carbon Nanofibers (CNFs), **IAS-CERN Joint Workshop on Collaboration with ASEAN Countries**, NTU, Singapore.

A.3 List of poster presentations

Pech., O. and Maensiri, S., (Nov. 2017), Fabrication and electrochemical properties of electro-spun porous carbon nanofibers”, **The First Materials Research**

Society of Thailand International Conference.The Empress Hotel, Chiang Mai, Thailand.

Pech., O. and Maensiri, S. , (Jun. 2018), Fabrication and electrochemical properties of carbon nanofibers by core-shell electrospinning technique, **2018 ISAF-FMA-AMF-AMEC-PFM Joint Conference (IFAAP 2018)**, International Convention Center, Hiroshima, Japan.



CURRICULUM VITAE

Name: Ouksaphea Pech

Date of Birth: May 31, 1984

Place of Birth: Phnom Penh, Cambodia

Education

2015-2018: Suranaree University of Technology (SUT), Nakhon Ratchasima, Thailand, Ph.D. in Physics.

2010-2013: Royal University of Phnom Penh (RUPP), Phnom Penh, Cambodia
M.Sc. In Physics.

2005-2006: National Institute of Education (NIE), Phnom Penh, Cambodia
B.Sc. +1

2001-2005: Royal University of Phnom Penh (RUPP), Phnom Penh, Cambodia
B.Sc. In Physics.

Position and Workplace Lecturer and Researcher, Graduate School of Science, Royal University of Phnom Penh (RUPP), Phnom Penh, Cambodia.